Astronomy & Astrophysics manuscript no. 43020corr
April 18, 2022

The *Planck* clusters in the LOFAR sky

I. LoTSS-DR2: New detections and sample overview

A. Botteon[1], T. W. Shimwell[2,1], R. Cassano[3], V. Cuciti[4], X. Zhang[1,5], L. Bruno[3,6], L. Camillini[7,8], R. Natale[7,8], A. Jones[4], F. Gastaldello[7], A. Simionescu[5,1,9], M. Rossetti[7], H. Akamatsu[5], R. J. van Weeren[1], G. Brunetti[3], M. Brüggen[4], C. Groeneveld[1], D. N. Hoang[4], M. J. Hardcastle[10], A. Ignesti[11], G. Di Gennaro[4], A. Bonafede[6,3], A. Drabent[12], H. J. A. Röttgering[1], M. Hoeft[12] and F. de Gasperin[4,3]

(Affiliations can be found after the references)

Received XXX; accepted YYY

ABSTRACT

Context. Relativistic electrons and magnetic fields permeate the intra-cluster medium (ICM) and manifest themselves as diffuse sources of synchrotron emission observable at radio wavelengths, namely radio halos and radio relics. Although there is broad consensus that the formation of these sources is connected to turbulence and shocks in the ICM, the details of the required particle acceleration, the strength and morphology of the magnetic field in the cluster volume, and the influence of other sources of high-energy particles are poorly known.

Aims. Sufficiently large samples of radio halos and relics, which would allow us to examine the variation among the source population and pinpoint their commonalities and differences, are still missing. At present, due to the physical properties of the sources and the capabilities of existing facilities, large numbers of these sources are easiest to detect at low radio frequencies, where they shine brightly.

Methods. We examined the low-frequency radio emission from all 309 clusters in the second catalog of *Planck* Sunyaev Zel'dovich detected sources that lie within the 5634 deg^2 covered by the Second Data Release of the LOFAR Two-meter Sky Survey (LoTSS-DR2). We produced LOFAR images at different resolutions, with and without discrete sources subtracted, and created overlays with optical and X-ray images before classifying the diffuse sources in the ICM, guided by a decision tree.

Results. Overall, we found 83 clusters that host a radio halo and 26 that host one or more radio relics (including candidates). About half of them are new discoveries. The detection rate of clusters that host a radio halo and one or more relics in our sample is 30 ± 11% and 10 ± 6%, respectively. Extrapolating these numbers, we anticipate that once LoTSS covers the entire northern sky it will provide the detection of 251 ± 92 clusters that host a halo and 83 ± 50 clusters that host at least one relic from *Planck* clusters alone. All images and results produced in this work are publicly available via the project website.

Key words. galaxies: clusters: general – galaxies: clusters: intracluster medium – radiation mechanisms: nonthermal – radiation mechanisms: thermal – catalogs

1. Introduction

Radio emission associated with galaxy clusters and their member galaxies is mainly related either to radio galaxies that are powered by a central active galactic nucleus (AGN) or to nonthermal components residing in the intra-cluster medium (ICM). While AGN are often bright sources that contribute the majority of the radio flux from a cluster at gigahertz frequencies, the diffuse sources generated by relativistic electrons (Lorentz factors of $\gamma_L > 1000$) that propagate in the ICM magnetic field ($\sim\mu$G level) have remained somewhat elusive, despite many extensive searches, due to their lower surface brightness and rapidly declining flux density with increasing frequency (e.g., Feretti et al. 2012; van Weeren et al. 2019, for reviews). The observed levels of diffuse radio emission from clusters suggest that a few percent of the energy of a cluster merger is dissipated by shocks and turbulence in the ICM and transferred to nonthermal components (the largest amount goes into ICM heating; see Markevitch & Vikhlinin 2007). However, the details of the particle acceleration and magnetic field amplification mechanisms on cluster scales are still poorly understood (e.g., Brunetti & Jones 2014, for a review). Thus, by studying the emission associated with the ICM we can probe the fundamental physics of particle acceleration in highly rarefied plasmas that are beyond the reach of those that can be studied in laboratories, and more generally we can provide insights into large-scale structure formation and evolution.

Diffuse cluster sources are typically classified as radio halos, mini-halos, relics, and revived fossil plasma sources (or phoenixes) according to their location in the cluster, morphology, size, and radio spectral properties. Observations with many facilities, such as the Very Large Array (VLA; Thompson et al. 1980), the Westerbork Synthesis Radio Telescope (WSRT; Hogbom & Brouw 1974), and the Giant Metrewave Radio Telescope (GMRT; Swarup et al. 1991), have played a crucial role in the discovery of new cluster radio sources and in constraining their main properties (e.g., Giovannini et al. 1999, 2006; Giovannini & Feretti 2000; Kempner & Sarazin 2001; Venturi et al. 2007, 2008; Rudnick & Lemmerman 2009; van Weeren et al. 2009, 2011). These instruments, in combination with X-ray observations, have provided conclusive evidence that diffuse (up to megaparsec-scale) radio sources in the ICM are connected to the dynamical motions of the ICM. Proton-proton collisions in the ICM represent an alternative process for producing (secondary) electrons in clusters (e.g., Dennison 1980; Blasi & Colafrancesco 1999); however, their contribution is likely not dominant enough to explain extended emission on megaparsec scales (e.g., Jeltema & Profumo 2011; Zandanel & Ando 2014; Brunetti et al. 2017; Adam et al. 2021). The search for corre-

lations between diffuse radio sources and host cluster properties (e.g., Liang et al. 2000; Cassano et al. 2007, 2008; Brunetti et al. 2009; de Gasperin et al. 2014; Yuan et al. 2015) as well as their connection with the cluster dynamical state (e.g., Buote 2001; Cassano et al. 2010b; Wen & Han 2013; Cuciti et al. 2015; Giacintucci et al. 2017) is fundamental to unveiling the origin of these objects. However, until recently, many of these studies were hampered by the sensitivity of the observations, which has limited the number of detections of diffuse emission to about a hundred and the statistical analysis to very massive systems. This has challenged the overall interpretation of the population of these sources through theoretical models (e.g., Cassano & Brunetti 2005; Cassano et al. 2006; Nuza et al. 2012, 2017; Brüggen & Vazza 2020).

Thanks to the increased sensitivity to these diffuse sources that has been made possible due to upgrades to facilities such as the Karl G. Jansky Very Large Array (Perley et al. 2011) and the upgraded Giant Metrewave Radio Telescope (uGMRT; Gupta et al. 2017), as well as the advent of new-generation interferometers, such as the LOw Frequency ARray (LOFAR; van Haarlem et al. 2013), the Murchison Widefield Array (MWA; Tingay et al. 2013), the Australian Square Kilometre Array Pathfinder (ASKAP; Hotan et al. 2021), and MeerKAT (Jonas 2009), it is now possible to search for diffuse radio sources in clusters with a number of complementary and sensitive instruments. In particular, the leap forward in the capabilities of low-frequency interferometers allows us to study diffuse cluster sources in a regime where they are brighter due to their steep synchrotron spectra ($\alpha > 1$, with $S_\nu \propto \nu^{-\alpha}$, where S_ν is the flux density at frequency ν and α is the spectral index). In this respect, LOFAR has recently enabled the first detailed observations of galaxy clusters at frequencies of <200 MHz thanks to the unprecedented high sensitivity and high resolution in its operational frequency range. This potential has already been demonstrated as LOFAR has proved to be very fruitful in investigating different aspects of nonthermal phenomena in the ICM, allowing us: to discover new instances of diffuse sources in clusters (e.g., Shimwell et al. 2016; Savini et al. 2018a, 2019; Wilber et al. 2019), including ultra-steep spectrum emission (e.g., Brüggen et al. 2018; Wilber et al. 2018; Mandal et al. 2020; Biava et al. 2021b) and very large-scale emission outside the central cluster region (e.g., Govoni et al. 2019; Botteon et al. 2019a, 2020b; Bonafede et al. 2021; Hoeft et al. 2021; Hoang et al. 2021b), as well as new faint halos and relics (e.g., Botteon et al. 2019a, 2021a; Locatelli et al. 2020; Hoang et al. 2021a) and high-z systems (e.g., Cassano et al. 2019; Di Gennaro et al. 2021a); to pinpoint the complex interplay between tailed cluster AGN and ICM motions (e.g., de Gasperin et al. 2017; Clarke et al. 2019; Hardcastle et al. 2019; Botteon et al. 2020a, 2021b; **?**); to study the central cluster AGN duty cycle, structure, and interaction with the hot ICM (e.g., Brienza et al. 2020; Bîrzan et al. 2020; Biava et al. 2021a; Timmerman et al. 2022); and to detect extended, extraplanar emission from star-forming galaxies infalling into clusters (e.g., Ignesti et al. 2020, 2022; Roberts et al. 2021a,b, 2022).

Sensitive wide-area searches for diffuse cluster sources require significant observational time and are arguably most efficient at low frequencies due to the higher survey speed resulting from the larger field-of-view (FoV) of the instruments. In addition, much of the undiscovered population is thought to have very steep spectra ($\alpha > 1.5$; e.g., Cassano & Brunetti 2005; Cassano et al. 2006). This implies that, of the planned wide-area surveys, those at low frequencies are anticipated to make the largest number of discoveries (e.g., Cassano et al. 2010a, 2012; Nuza et al. 2012). In this respect, LOFAR is carrying out wide and deep surveys, and it is currently observing the entire northern sky at 120−168 MHz and 42−66 MHz in the context of the LOFAR Two-meter Sky Survey (LoTSS; Shimwell et al. 2017) and the LOFAR LBA Sky Survey (LoLSS; de Gasperin et al. 2021), respectively. These surveys have enormous discovery potential in many fields of astrophysics, including galaxy cluster science, offering the opportunity to study large samples of objects in synergy with surveys performed at other wavelengths. As it is currently believed that the cluster mass is a key parameter for the formation of the most extended radio sources in the ICM (namely, halos and relics), catalogs of clusters detected via the Sunyaev-Zel'dovich (SZ) effect (Sunyaev & Zel'dovich 1972) are particularly interesting as they provide unbiased samples that are almost mass-selected and that are ideal to be cross-matched with the LOFAR surveys.

This is Paper I of a series dedicated to the study of diffuse radio emission in the ICM of galaxy clusters selected from the second *Planck* catalog of SZ sources (PSZ2; Planck Collaboration XXVII 2016) that have also been covered by the Second LoTSS Data Release (LoTSS-DR2; Shimwell et al. 2022). It represents an extension of our previous work (van Weeren et al. 2021), which was based on the galaxy clusters covered by the First LoTSS Data Release (LoTSS-DR1; Shimwell et al. 2019). Here, we present the new sample (Sect. 2), describe the methods and data used (Sect. 3), classify the cluster radio sources (Sect. 4), provide the quantities used for the analysis that will be performed in subsequent papers, and present the new detections and the results of our study (Sects. 5 and 6). In Cassano et al. (in preparation) and Cuciti et al. (in preparation), we discuss the occurrence and the scaling relations of radio halos in the sample, while in Jones et al. (in preparation) we focus on radio relics. Other papers dedicated to the study of the X-ray properties of the sample (Zhang et al., in preparation) and to the methods developed to derive upper limits to the diffuse cluster radio emission (Bruno et al., in preparation) are also forthcoming.

Hereafter, we adopt a Λ cold dark matter cosmology, with $\Omega_\Lambda = 0.7$, $\Omega_m = 0.3$, and $H_0 = 70$ km s^{-1} Mpc^{-1}.

2. Cluster sample

The PSZ2 catalog (Planck Collaboration XXVII 2016) contains 1653 SZ sources detected over the entire sky. Here, we focus on the 309 entries listed in Table A.1 that lie in the LoTSS-DR2 footprint. This comprises two regions covering 5634 deg^2 that are centered at approximately 12h45m00s +44°30′00″ and 01h00m00s +28°00′00″. In the PSZ2 catalog, 63 entries out of 309 are without redshift and mass estimates, meaning that they were not confirmed detections at the time of their publication. However, in follow-up optical studies by Buddendiek et al. (2015), Burenin (2017), Burenin et al. (2018), Barrena et al. (2018), Streblyanska et al. (2018), Streblyanska et al. (2019), Aguado-Barahona et al. (2019), Boada et al. (2019), and Zohren et al. (2019), redshifts have been obtained for 35 of these 63 *Planck* detections. From these redshifts we computed M_{500} by interpolating the M_{500} versus z curves provided in the PSZ2 individual algorithm catalogs for each detection (see Appendix D in Planck Collaboration XXVII 2016). There are 28 remaining PSZ2 detections without redshift confirmation in the LoTSS-DR2 area. For simplicity, in the paper we refer to all 309 entries in Table A.1 as "galaxy clusters", even if 28 of them should formally be referred to as "SZ detections". In the end, our sample consists of galaxy clusters that are known to span at least the redshift and mass ranges of $0.016 < z < 0.9$ (median of 0.280) and 1.1×10^{14} M$_\odot$ $< M_{500} < 11.7 \times 10^{14}$ M$_\odot$ (median of 4.9×10^{14}

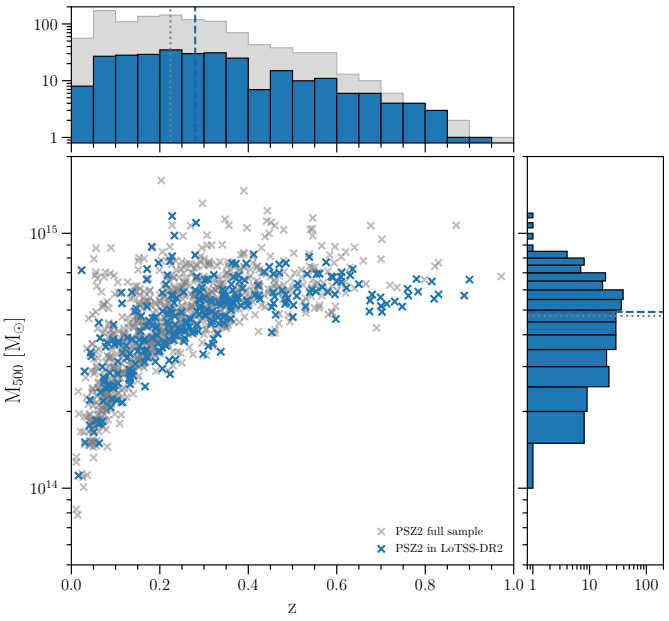

Fig. 1. Redshift-mass distribution of PSZ2 sources. Clusters that are located in the LoTSS-DR2 area are indicated in blue. The histograms show the number of clusters at various redshifts and masses; the dashed and dotted lines mark the median values of the LoTSS-DR2 sample and the full PSZ2 sample, respectively. Similarly to the full PSZ2 sample, our sample spans a wide range of redshifts and masses.

$M_\odot$). As shown in Fig. 1, the distribution of redshift and mass in the sample of clusters included in our study provides a qualitatively good representation of the full PSZ2 population. Nonetheless, we note that our sample was selected only based on right ascension and declination cuts. For a better assessment of the similarity between the two samples, we performed a two-sample Kolmogorov-Smirnov test on M_{500} and z, and found p-values of the null hypothesis (that the two samples are drawn from the same distribution) of 0.25974 and 0.00148, respectively. The absolute differences between the median values of the two samples are 0.17×10^{14} $M_\odot$ (for the mass) and 0.056 (for the redshift). These numbers indicate that the mass distributions of the two samples are in agreement. Concerning the redshift distributions, the low p-value and the slightly higher median value of the LoTSS-DR2 sample are related to the fact that our sample includes clusters that were confirmed with optical follow-ups after the publication of the *Planck* catalog. These clusters did not have a redshift in the original PSZ2 catalog and they are mostly clusters at high z (30 out of the 35 clusters confirmed by optical follow-ups have redshift higher than the median value of the full PSZ2 sample). The distribution of the clusters within the LoTSS-DR2 area is shown in Fig. 2.

3. Methods and data analysis

3.1. Data reduction

LoTSS is an ongoing radio survey that employs LOFAR High Band Antennas (HBA) to observe the entire northern sky in the frequency range 120−168 MHz. LoTSS observations are generally 8 hr long, the nominal central frequency of the survey is 144 MHz, and the typical root-mean-square (rms) noise σ is ∼0.1 mJy beam^{-1}. More details on LoTSS, such as its design and scientific goals, can be found in Shimwell et al. (2017, 2019). Here, we use the data from the LoTSS-DR2 (Shimwell et al. 2022), which covers an area that is a factor of ∼13 larger than LoTSS-DR1 and has additional improvements to image fidelity particularly for faint diffuse structures. LoTSS-DR2 pointings are processed with fully automated pipelines developed by the LOFAR Surveys Key Science Project team that aim to correct for direction-independent and direction-dependent effects that are present in the data. These pipelines are PREFACTOR[1] (van Weeren et al. 2016; Williams et al. 2016; de Gasperin et al. 2019) and `ddf-pipeline`[2] (Tasse et al. 2021). The latter employs KILLMS (Tasse 2014b,a; Smirnov & Tasse 2015) and DDFACET (Tasse et al. 2018) to perform direction-dependent self-calibration of the entire LOFAR FoV, and has been significantly improved compared to the version used to process LoTSS-DR1 (Shimwell et al. 2017). We refer the reader to Tasse et al. (2021) and Shimwell et al. (2022) for more details.

In order to further improve the image quality toward the targets in our sample while also allowing for more flexible imaging, we adopted the "extraction + recalibration" scheme described by van Weeren et al. (2021), which was also used for the analysis of the galaxy clusters in the LoTSS-DR1 region. This method consists of the subtraction of the sources outside a small square region of the sky (typically, ∼0.3−0.7 deg^2) containing the target from the *uv* data and using the direction-dependent calibration solutions and sky model derived from `ddf-pipeline`. The extracted data sets are then phase-shifted to the center of the region, averaged, and corrected for the LOFAR station beam in this direction. Finally, the calibration of the data is refined by performing a series of typically 4 phase and 6 phase and amplitude calibration loops. LoTSS pointings have a full width at half maximum of 3.96° at 144 MHz and are separated by ∼2.6°, so usually a specific target is covered by multiple pointings, which are combined and analyzed together. We typically extract the visibility data from pointings that are <2.2° from the center of the extracting region.

Among the 309 PSZ2 sources in the LoTSS-DR2 area, we were not able to apply this method to 5 targets. This included the Coma cluster (PSZ2 G057.80+88.00) whose radio emission is too large for us to approximate the ionospheric and beam errors with single solutions as is done in the extraction + recalibration scheme, requiring a special treatment (see Bonafede et al. 2021). Embedded within the Coma cluster radio halo, there are a further two clusters (PSZ2 G056.62+88.42 and PSZ2 G061.75+88.11) where we are unable to differentiate their emission from that of Coma. Finally, PSZ2 G060.10+15.59 and PSZ2 G075.08+19.83 are located in regions where the direction-dependent calibration with `ddf-pipeline` failed likely due to very poor ionospheric conditions. These 5 targets were excluded from the analysis. A collection of the LOFAR images of our PSZ2 sample is shown in Fig. B.1.

3.2. Alignment of the flux scale

Because of inaccuracies in the LOFAR beam model, transferring amplitude solutions from the calibrator field data to the target field data may introduce offsets in the flux density scale of the target field (e.g., Hardcastle et al. 2016). For this reason, as described by Hardcastle et al. (2021) and Shimwell et al. (2022), when constructing final LoTSS-DR2 catalogs and mosaics the images are scaled to align the flux density scale with the Roger et al. (1973) scale. This procedure involves cross-matching cata-

[1] `https://github.com/lofar-astron/prefactor`
[2] `https://github.com/mhardcastle/ddf-pipeline`

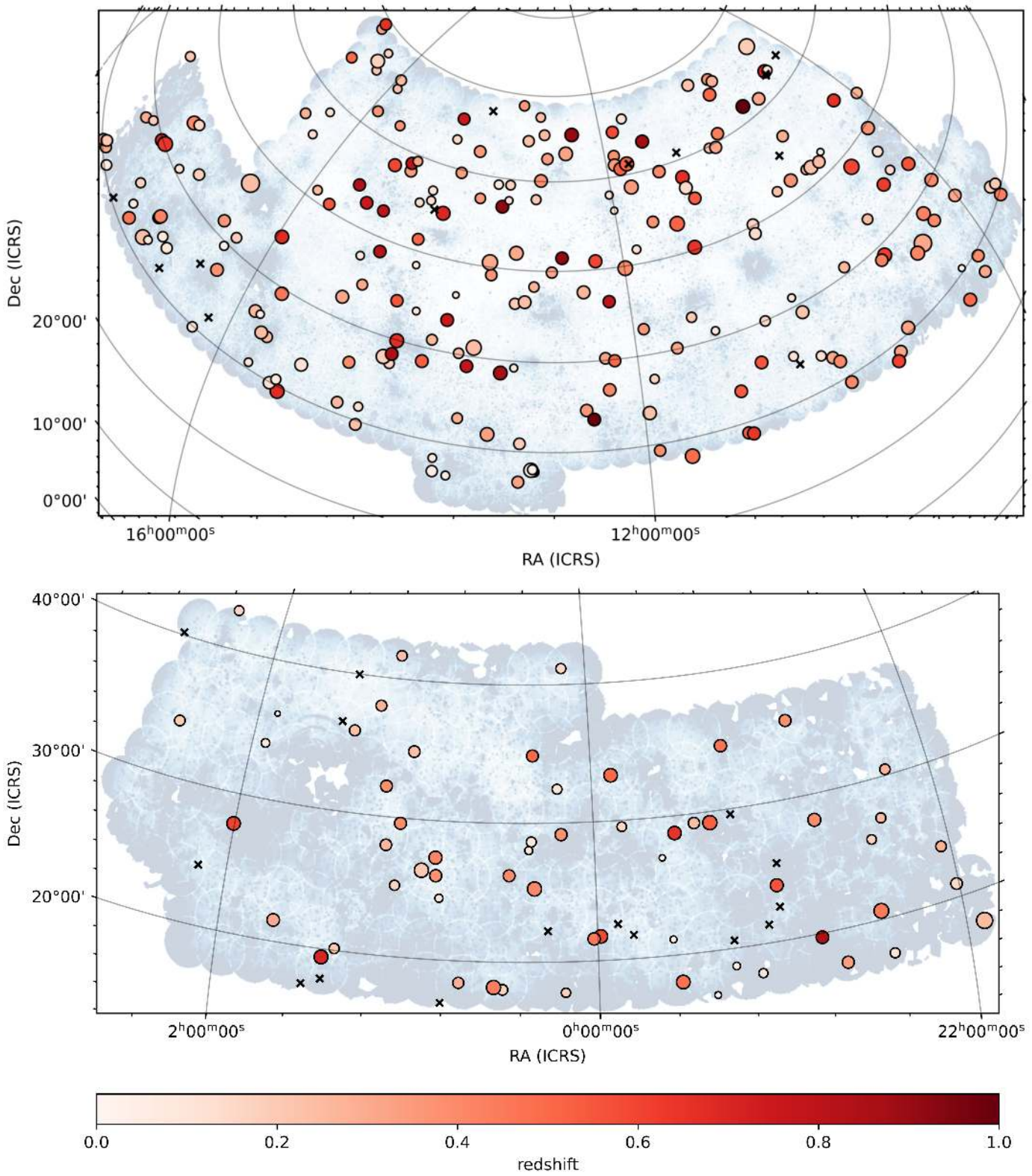

Fig. 2. Position of the PSZ2 clusters in the RA-13 (*top*) and RA-1 (*bottom*) regions covered by LoTSS-DR2. The color code indicates the redshift of the cluster. The radius of the circle is proportional to M_{500}. Clusters without redshift and mass are reported as black crosses. The background image represents the noise variations in LoTSS-DR2 (darker colors denote higher noise values) and is reproduced from Shimwell et al. (2022).

logs derived from each LoTSS-DR2 observation with the NRAO VLA Sky Survey (NVSS; Condon et al. 1998) catalog and assuming a global scaling relationship between NVSS and the 6C catalog (Hales et al. 1988, 1990), which is thought to be consistent with Roger et al. (1973) to 5%. In LoTSS-DR2 the derived scaling factors are applied to the images during the mosaicing and not to the visibilities directly (Shimwell et al. 2022). Hence, for our processing, which uses the archived *uv* data (Sect. 3.1),

we instead adopt a procedure where we align catalogs created from the images obtained from the extracted data sets with the final LoTSS-DR2 catalog in which the scaling factors have been applied. For this we perform a simple cross-match between the two catalogs (5 arcsec) and use the criteria given in Shimwell et al. (2022) to select only compact sources and remove those that are not (nearest neighbor within 30 arcsec) and those at low signal-to-noise (less than 7). As outliers can still exist in this cross-matched catalog, we used three different fitting methods (Sen 1968, Huber 1981, and regular linear regression). All three are available within the `scikit-learn` package[3] (Pedregosa et al. 2012), and all have different outlier rejection criteria, ranging from a more robust median calculation to a less robust simple linear regression. About 90% of the time the derived values from the different methods give results that are consistent within 10%. The remaining cases are those where outliers are more prominent and are rejected differently by the adopted fitting methods. Thus, for each fit we calculated the mean absolute error and selected the method with the lowest value, which we then used to scale our images for that particular object and align it with the LoTSS-DR2 scale.

3.3. Radio images

For each cluster, we produced images at different resolutions to search for diffuse radio emission in the ICM and perform the subsequent analysis. The imaging was done with WSClean v2.8 (Offringa et al. 2014) adopting the Briggs (1995) weighting scheme with `robust=-0.5`, and applying Gaussian *uv* tapers in arcsec equivalent approximately to 25, 50, and 100 kpc at the cluster redshift. For the PSZ2 entries without redshift, the Gaussian *uv* taper was set to 15, 30, and 60 arcsec to span a wide range of resolutions. The 60 arcsec tapered images were produced only with discrete sources subtracted (see below). For each cluster we also produced a higher-resolution image by using `robust=-1.25`, which leads to a resolution typically of 5.0 arcsec × 3.5 arcsec. The multi-scale multifrequency deconvolution option (Offringa & Smirnov 2017) was enabled in WSClean adopting fixed scales (`-multiscale-scales 0,4,8,16,32,64`) and subdividing the bandwidth into 6 channels for all imaging runs.

We used the images obtained with `robust=-0.5` and no *uv* taper as reference images to assess the quality of the data sets, which were visually inspected and graded according to: 1 for high quality images; 2 for images that are partially affected by calibration artifacts or higher rms levels; and 3 for low quality images where the scientific analysis is not possible due to strong calibration artifacts or very high rms noise levels (i.e., >0.3 mJy beam^{-1}). This image quality is reported in Table A.1. Radio contours from the reference images were overlaid on optical Panoramic Survey Telescope and Rapid Response System (Pan-STARRS; Chambers et al. 2016) mosaics using the *g,r,i* filters to verify the presence of optical counterparts.

To better study the diffuse emission, we removed the contribution of discrete sources by imaging the data sets with a *uv* cut corresponding to a physical scale of 250 kpc at the cluster redshift (for PSZ2 entries without redshift we arbitrarily adopted a *uv* cut of 2722λ, corresponding to 2.82 arcmin or 250 kpc at $z = 0.2$) and subtracting their clean components from the visibility data. The new visibility data were then imaged with the same values of *uv* taper adopted for the images obtained before discrete source subtraction. The low-resolution radio contours with discrete sources subtracted were overlaid onto the *Chandra* and/or *XMM-Newton* X-ray images (when available) smoothed to 30 kpc by a Gaussian function (for more details on the X-ray images, see Sect. 3.4).

An example of the set of images produced for each cluster is shown in Fig. 3. All images are available for download in PNG and FITS format on the project website[4].

3.4. X-ray images and morphological parameters

As we will describe in Sect. 4, for the purpose of classifying the detected cluster diffuse radio sources, it is crucial to compare the position of the extended radio emission with the other cluster components and especially the ICM, which can be traced by its X-ray emission and by the SZ effect. Since all clusters in our sample have been detected by *Planck*, two-dimensional maps of the SZ signal are available for all of them (Planck Collaboration XXII 2016) but their use is hampered by their 10 arcmin resolution, which does not allow us to spatially resolve most of the targets of the sample. We thus decided to map the ICM distribution with the X-ray images obtained by the current generation X-ray telescopes (*Chandra* and *XMM-Newton*), whose spatial resolution is higher or comparable to that of our radio images (Sect. 3.3). We searched the *Chandra* and *XMM-Newton* archives for observations of the targets in our sample and we retrieved the data for 115 and 100 clusters, respectively (72 targets have been observed both by *Chandra* and *XMM-Newton*). The procedures used to prepare the X-ray images for each instrument are described in Sects. 3.4.1 and 3.4.2.

The ICM distribution is very sensitive to the dynamical history of the clusters, and therefore quantitative measurements of the morphology of the X-ray emission of galaxy clusters have proved to be an effective way to characterize the dynamical state of large samples of galaxy clusters (e.g., Buote 2001; Santos et al. 2008; Cassano et al. 2010b; Rasia et al. 2013; Parekh et al. 2015; Rossetti et al. 2017; Lovisari et al. 2017, and references therein). The use of a set of morphological parameters of the X-ray emission of clusters is only an approximation to the daunting task of assessing the dynamical state of the cluster. However, the combination of two morphological parameters is effective to provide a relatively robust classification. In particular the optimal choice is to combine a parameter sensitive to the presence of substructure, the centroid shift, with a parameter more sensitive to the core properties, the concentration parameter (Lovisari et al. 2017). In fact this has been the usual choice made in previous studies of the classification of radio sources (for recent examples, see Cuciti et al. 2015, 2021). The physical scale over which the morphological parameters are measured is also an important factor: here, following previous studies (Cassano et al. 2010b; Cuciti et al. 2021), we analyze an aperture of $R_{\rm ap} = 500$ kpc centered on the peak of the X-ray emission.

The concentration parameter has been introduced by Santos et al. (2008) as the ratio of the flux within two circular apertures to effectively identify cool cores even at high redshift. Here we adopt the choice of apertures made by Cassano et al. (2010b)

$$c = \frac{F(r < 100\,\mathrm{kpc})}{F(r < R_{\rm ap})}\,, \tag{1}$$

where $F(r < 100\,\mathrm{kpc})$ is the flux within 100 kpc and $F(r < R_{\rm ap})$ is the flux within the aperture of 500 kpc. The error on this parameter is obtained by taking into account the Poisson noise

[3] `https://scikit-learn.org/stable/`

[4] `https://lofar-surveys.org/planck_dr2.html`

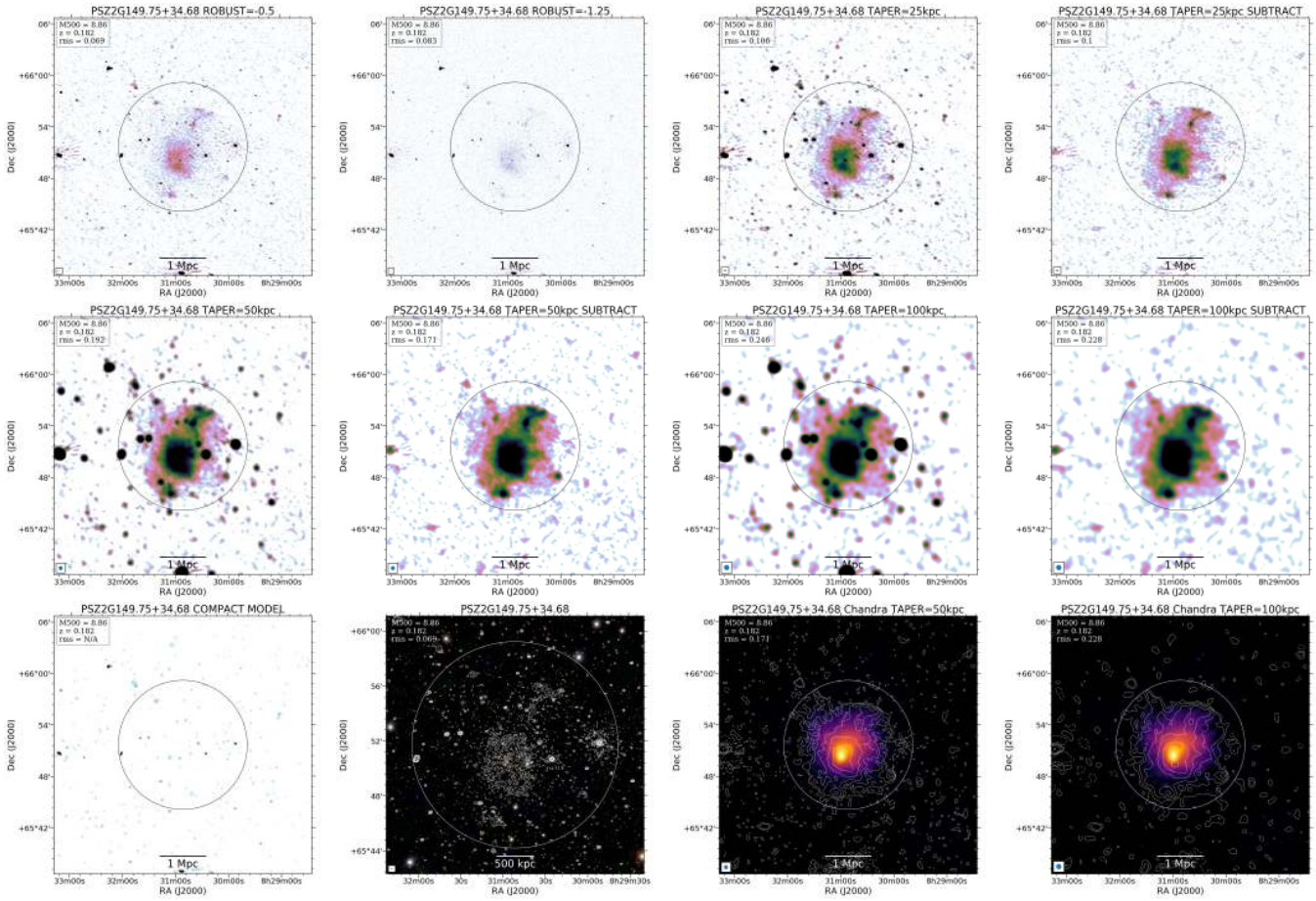

Fig. 3. Example of the set of images that we produced for each object in our sample. The displayed cluster is PSZ2 G149.75+34.68, and the reported panels show (from left to right and from top to bottom) the reference image (`robust=-0.5`), the high-resolution image (`robust=-1.25`), taper 25, 50, and 100 kpc images with and without discrete sources, the clean model components used for the source subtraction, contours from the reference radio image starting from 3σ overlaid on an optical image (Pan-STARRS *g,r,i*), and taper 50 and 100 kpc discrete-source-subtracted contours starting from 2σ overlaid on an X-ray image (*Chandra* or *XMM-Newton*). Contours are always spaced by a factor of 2. The beam is shown in the bottom-left corner, and the mass (M_{500}, in $\times 10^{14}$ $M_\odot$ units), redshift (z), and image noise (rms, in mJy beam^{-1} units) are reported in the top-left corner. The circle denotes r_{500} and is centered at the coordinates reported in the PSZ2 catalog. The images are available at full resolution as well as in FITS format on the project website, `https://lofar-surveys.org/planck_dr2.html`.

in both the source and background images.

The centroid shift (Mohr et al. 1993; Poole et al. 2006) is defined as the variance of the separation between the X-ray peak and the centroid of the emission obtained within a number N of apertures of increasing radius out to $R_{\rm ap}$,

$$w = \left[\frac{1}{N-1}\sum_i (\Delta_i - \overline{\Delta})^2\right]^{\frac{1}{2}} \frac{1}{R_{\rm ap}}\,, \qquad (2)$$

where Δ_i is the distance between the X-ray peak and the centroid of the i-th aperture. It traces the variation in the position of the centroid introduced by the presence of substructures in the X-ray emission. The number N of apertures is fixed at 20 in the *XMM-Newton* analysis and it is given by the number of annuli of fixed 5 arcsec width within 500 kpc for the *Chandra* analysis. The error on this parameter is obtained by using a Monte Carlo approach: for the *Chandra* analysis we simulated 100 realizations of the X-ray images obtained by resampling the counts per pixel according to their Poisson error, performed the measurement on the simulated image and estimated the standard deviation of the distribution of w thus obtained; for the *XMM-Newton* analysis we simulated 10000 realizations of the centroids of the 20 apertures, sampled within their statistical errors.

We measured the concentration parameter and the centroid shift for 105 PSZ2 objects with *Chandra* and for 98 PSZ2 objects with *XMM-Newton* as a result of the following four selections: (i) a low redshift cut to accommodate the aperture of 500 kpc within the FoV of each respective detector ($z > 0.065$ for ACIS-I, $z > 0.072$ for ACIS-S, and $z > 0.035$ for *XMM-Newton*); (ii) PSZ2 G165.95+41.01 does not have a measurement because of a possible incorrect redshift estimate: the X-ray and optical images suggest that this object is at a higher z compared to the value of $z = 0.062$ reported in the PSZ2 catalog (see the note in the catalog that discusses a superposition with a $z = 0.21$ object); (iii) PSZ2 G067.52+34.75 does not have a *Chandra* morphological measurement because the observation is performed in a sub-array mode that does not allow a 500 kpc aperture to be accommodated; and (iv) PSZ2 G126.27+51.61 does not have a measurement because the available *Chandra* observation is too shallow for the faint emission of this high redshift ($z = 0.815$) cluster.

There are 63 objects that have both *Chandra* and *XMM-Newton* measurements and the total number of PSZ2 clusters in our sample for which we have X-ray morphological parameters is 140. For objects for which different clumps of X-ray emission could be clearly distinguished we measured morphological pa-

rameters for each component, labeling them according to their position in the sky. This explains why Table A.2, where we list the c and w, has 150 entries. For the 63 objects (65 measurements including the objects with multiple clumps) with both *Chandra* and *XMM-Newton* measurements we provide combined morphological parameters according to the following equations:

$$\mathcal{P}_{\rm combined} = \frac{1}{2} \times (\mathcal{P}_{\rm xmm} + \mathcal{P}_{\rm chandra}) \ , \tag{3}$$

where $\mathcal{P}$ is either c or w and the error $\sigma_{\mathcal{P}}$ on this combined parameter is given by the sum of the statistical $\sigma_{\mathcal{P},\rm stat}$ and systematic $\sigma_{\mathcal{P},\rm sys}$ error,

$$\begin{aligned}\sigma^2_{\mathcal{P}} =& \sigma^2_{\mathcal{P},\rm stat} + \sigma^2_{\mathcal{P},\rm sys} \\ =& \frac{1}{4} \times \left(\sigma^2_{\mathcal{P},\rm xmm} + \sigma^2_{\mathcal{P},\rm chandra} + 2\sigma_{\mathcal{P},\rm xmm}\sigma_{\mathcal{P},\rm chandra}\right) \\ &+ \frac{1}{4} \times (\mathcal{P}_{\rm xmm} - \mathcal{P}_{\rm chandra})^2 \ ,\end{aligned} \tag{4}$$

where we also take into account the covariance with the term $2\sigma_{\mathcal{P},\rm xmm}\sigma_{\mathcal{P},\rm chandra}$. These values are used to discuss the occurrence of diffuse radio emission with the cluster dynamical state in Cassano et al. (in preparation). A thorough comparison between parameters derived from *XMM-Newton* and *Chandra* as well as the detailed analysis on the X-ray data will be presented in Zhang et al. (in preparation).

We describe the reduction and analysis steps used for the *Chandra* and *XMM-Newton* data in the following subsections.

3.4.1. *Chandra* data reduction and analysis

We analyzed *Chandra* data with the *Chandra* Interactive Analysis of Observations (CIAO) software v4.13 using CALDB v4.9.4 (Fruscione et al. 2006), reprocessing data from the level 1 event files and following the standard data reduction threads[5]. We reprocessed event files using the `chandra_repro` tool and soft proton flares were excluded with the `deflare` task with the `lc_clean` routine analyzing the light curves extracted from the S2 chip when in ACIS-I configuration and from the S3 chip when in ACIS-S configuration. We used the `fluximage` tool to produce images in the 0.5−7.0 keV bands and the appropriate exposure and point spread function maps. For the purpose of background subtraction we used the `blanksky` and `blankskyimage` tools to provide a corresponding background image to be subtracted. We detected the point sources using the `wavdetect` tool, and by means of `dmfilth` we replaced their emission with the mean count rate in a surrounding annulus. Images were smoothed to a resolution of 30 kpc at the cluster redshift to minimize the effect of having different physical sizes for the same pixel scale given the broad redshift range of our sample (see the discussion in Yuan & Han 2020). The peak of the X-ray image used as the center of the cluster has been selected as the brightest pixels in the smoothed image after masking the point sources. When multiple observations were available for the same object, we used the observation with the longest available exposure time. For all cases, our single ObsID images have at least 500 counts, which is a safe limit to have a robust measurement of the X-ray morphological parameters (e.g., Nurgaliev et al. 2013).

[5] `http://cxc.harvard.edu/ciao/threads/index.html`

3.4.2. *XMM-Newton* data reduction and analysis

We used *XMM-Newton* Science Analysis System (SAS) v18.0.0 for *XMM-Newton* European Photon Imaging Camera (EPIC) data reduction (Gabriel et al. 2004). MOS and pn event files are obtained from the observation data files with the tasks `emproc` and `epproc`. The out-of-time (OoT) event files of pn are produced by `epproc` as well. We extracted count images in the 0.5−2.0 keV band. The OoT count maps are directly subtracted from each pn count image following the user guide[6]. The corresponding exposure maps were generated using task `eexpmap` with parameter `withvignetting=yes`. Each exposure map was then multiplied by the on-axis effective area calculated by `arfgen`.

We used stacked filter wheel closed (FWC) event files as non-X-ray background (NXB). For each ObsID, the FWC event files were re-projected using the task `evproject` to match the observation. For the two MOS detectors, the NXB count maps were scaled using the blank regions out-of-FoV. For the pn detector, because of the contamination in out-of-FoV regions, we estimated the scaling factor based on the long-term NXB variation due to solar activities, which will be detailed described in Zhang et al. (in preparation).

Point source detection and removal procedures are the same as the *Chandra* data analysis. For each object, we stacked the point-source-removed NXB-subtracted count images and exposure maps, respectively. The stacked net count image was then divided by the stacked exposure map to obtain the final point source free flux map for morphological analysis. The X-ray peak of each object is determined from the 30 kpc Gaussian smoothed flux map.

4. Classification of radio sources

For each object listed in Table A.1 we searched for diffuse radio sources in the ICM that are not clearly associated with any AGN by visually inspecting the set of LOFAR images at different resolutions (with and without source subtraction) together with the optical and X-ray overlay images. To make the classification of the radio emission as objective as practical at present and easily reproducible, we created a decision tree (Fig. 4) that we followed during the inspection of the images and classified each cluster. Below we define the six classes of objects that form the end points of our decision tree.

"Radio halos" (RH) are extended sources that occupy the region where the bulk of the X-ray emission from the ICM is detected. Historically, they were divided according to their sizes: giant halos extended on cluster-scale and mini-halos covering the cluster central region. Since in this work we are dealing with a large sample of clusters with masses spanning over one order of magnitude of difference, we prefer to not separate mini-halos from giant-radio halos based on the size of the radio emission; instead, we refer generically to radio halos.

"Radio relics" (RR) are elongated sources whose position is offset from the bulk of the X-ray emission from the ICM and consistent with lying in cluster outskirts. We also checked for a sharp edge in the radio emission and a largest-linear size (LLS) $\gtrsim 300$ kpc.

The classification "candidate radio halo" or "candidate radio relic" (cRH or cRR) is used when *Chandra* or *XMM-Newton* X-ray observations are not available and as such the presence of a

[6] `http://xmm-tools.cosmos.esa.int/external/xmm_user_support/documentation/sas_usg/USG/removingOoTimg.html`

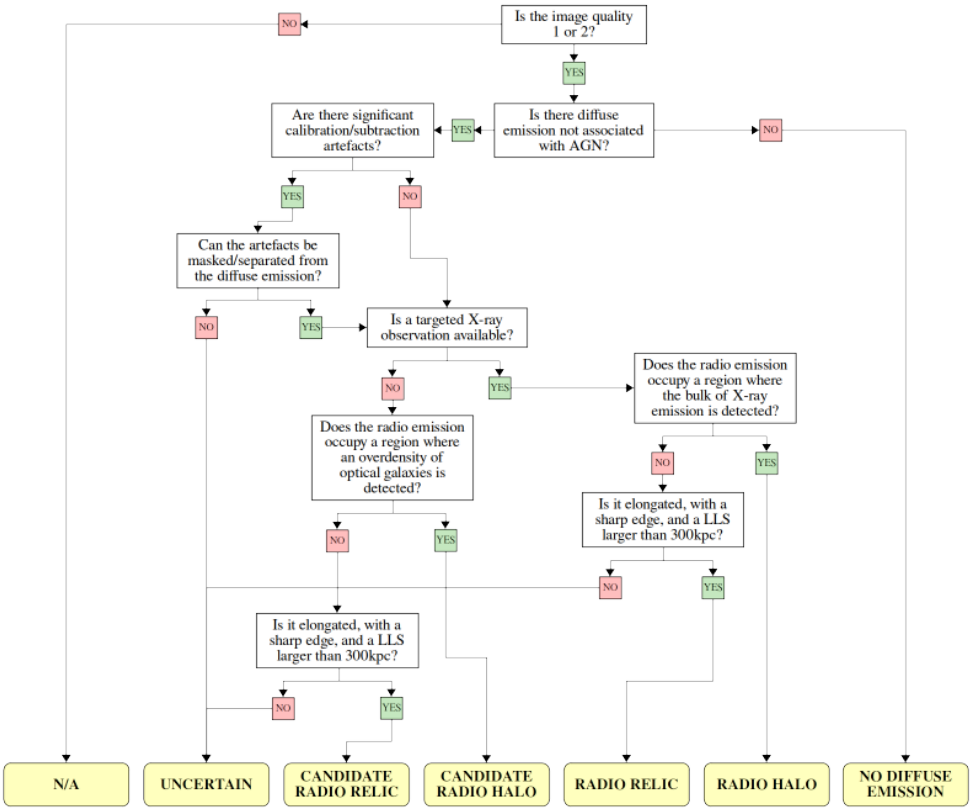

Fig. 4. Decision tree used to classify the diffuse radio sources in the ICM. The classes of objects that form the end points of the decision tree are described in Sect. 4.

halo or relic cannot be firmly claimed because we are uncertain if the emission is in the central or outer region of the ICM. However, it is possible to make an assessment based on the position of the radio emission with respect to the apparent overdensity of galaxies in the optical image. We thus classify the emission as being a candidate radio halo or radio relic if it is consistent with the other properties of these types of sources but colocated with or offset from the overdensity of galaxies rather than the X-ray emission from the ICM.

The "uncertain" (U) classification is for objects whose emission was significantly affected by calibration and/or subtraction artifacts or which did not show a morphology, size, and/or position consistent with the categories of radio halos and relics.

"No diffuse emission" (NDE) indicates that these objects do not show the presence of diffuse emission that could be attributed to the ICM (although they may show the presence of lobes or tails from AGN in the field).

Finally, "not applicable" (N/A) is used if the image quality is 3 (see Sect. 3.3) and as such the object cannot be adequately classified because of the poor data quality.

The classification for each target in the sample performed following the decision tree of Fig. 4, where the endpoints reflect the definitions above, is reported in Table A.1. If a target showed more than one diffuse source not related with any AGN, we repeated the decision tree for each source separately. All the answers to the questions of the decision tree are available on the project website. A gallery highlighting the wide variety of different types of emission is shown in Fig. 5.

We note that during our classification we did not attempt to identify radio phoenixes. These complex sources trace AGN radio plasma that has an ultra-steep ($\alpha \gtrsim 1.8$) spectrum and that is thought to have been reenergized through processes in the ICM, unrelated to the radio galaxy itself. New instances of this class of objects are rapidly emerging thanks to sensitive observations at low frequencies (e.g., de Gasperin et al. 2017; Kale et al. 2018; Mandal et al. 2019, 2020; Duchesne et al. 2020, 2021; **?**; Botteon et al. 2021b; Hodgson et al. 2021, for recent works). Our choice of not yet attempting to classify radio phoenixes is twofold. First, their definition is tightly connected to the spectral index, requiring the analysis of multifrequency observations. Second, their amorphous morphology and small sizes (at most a few hundred kiloparsecs) make a robust classification even more challenging. That said, in Table A.1 we do highlight several instances where a suspected radio phoenix was noted to form a very prominent part of the cluster emission (for example, when it is the dominant emission in the cluster volume).

5. Flux density measurements

In the following subsections, we describe how we computed the total flux density S_ν of the radio halos and relics in our sample. These values were used to calculate the k-corrected radio power of the sources at 150 MHz as

$$P_{150} = 4\pi S_{150} D_{\rm L}^2 (1+z)^{\alpha-1}\,, \tag{5}$$

where $D_{\rm L}$ is the luminosity distance and $S_{150} = S_{144}\left(\frac{144\,\rm MHz}{150\,\rm MHz}\right)^{\alpha}$. Because our integrated flux density measurements are obtained at 144 MHz, S_{150} is only marginally affected by the adopted (unknown) radio spectral index. In this respect, we assumed $\alpha = 1.3$ for radio halos and $\alpha = 1.0$ for radio relics, which are typical values found in the literature for these kinds of sources (see, e.g.,

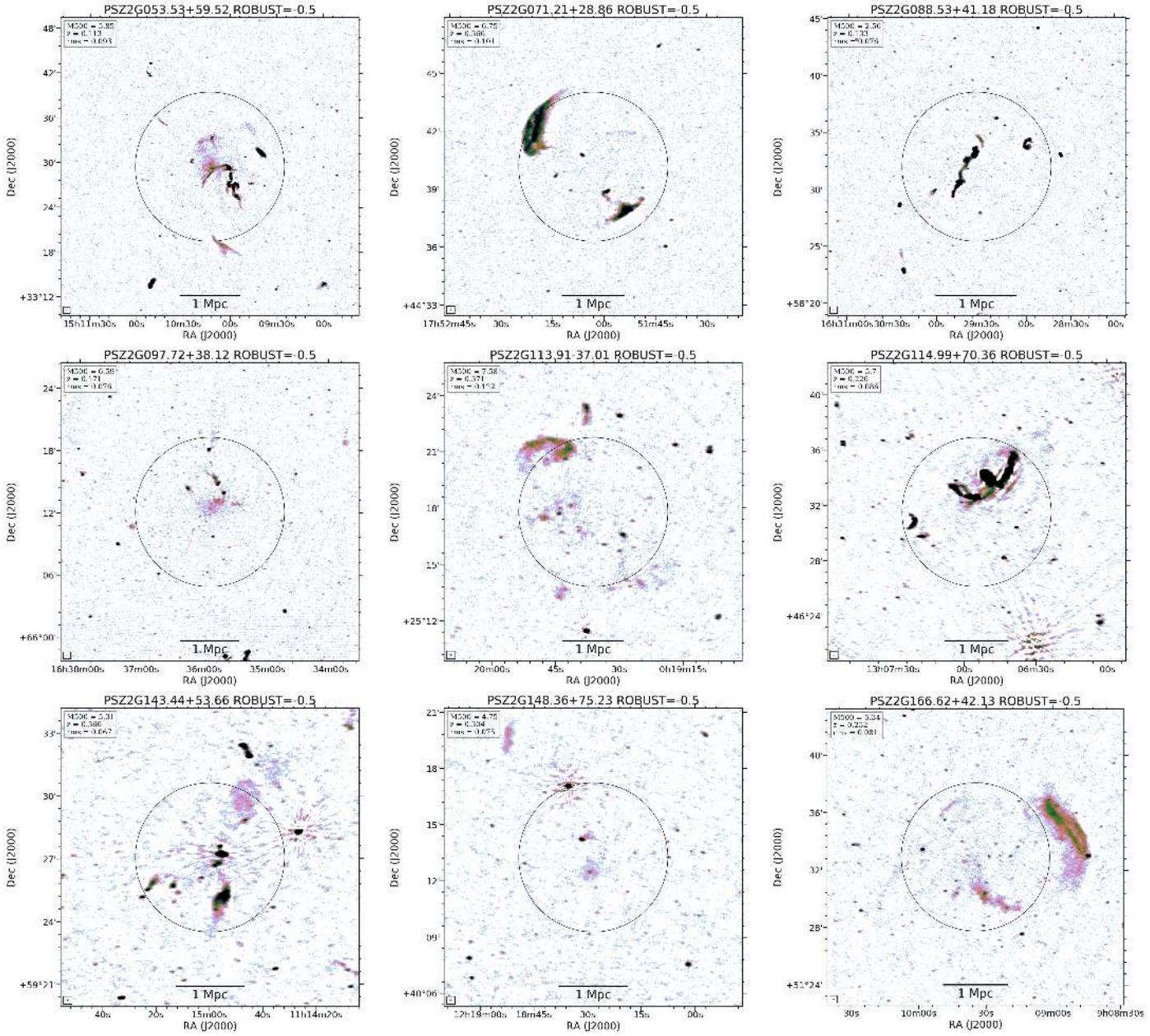

Fig. 5. Collection of clusters that show several types of radio emission. PSZ2 G053.53+59.52 has a central radio halo and a number of sources of uncertain origin. PSZ2G071.21+28.86 has a double radio relic. PSZ2 G088.53+41.18 is a system without diffuse cluster emission as the only emission detected is associated with an optical galaxy. PSZ2 G097.72+38.12 has a radio halo. PSZ2 G113.91-37.01 has a radio halo and two relics. PSZ2 G114.99+70.36 has emission of uncertain origin. PSZ2 G143.44+53.66 has emission of uncertain origin. PSZ2 G148.36+75.23 has a radio halo. PSZ2 G166.62+42.13 has a radio halo and multiple relics. We remark that the classification was done by inspecting all the sets of images available, while the images displayed in this gallery are only the reference ones (i.e., those with `robust=-0.5` and no *uv* taper). For a more complete picture of the large variety of radio structures observed in our sample, we refer the reader to Fig. B.1 and to the project website.

Feretti et al. 2012; van Weeren et al. 2019). Instead, the rest-frame radio power is more sensitive to the spectral index, especially for sources at higher redshift, due to the k-correction term appearing in Eq. 5. The interested reader should take P_{150} with more caution particularly for the radio halos in the sample at high z, which could be characterized by values of $\alpha > 1.3$ (Di Gennaro et al. 2021b).

The quantities derived for the radio halos and relics in our sample are reported in Tables A.3 and A.4, respectively. In the tables, uncertainties on S_{150} (hence, on P_{150}) take into account the statistical ($\sigma_{\rm stat}$), systematic ($\sigma_{\rm sys}$), and subtraction ($\sigma_{\rm sub}$) errors, which were summed in quadrature. The statistical error

$$\sigma_{\rm stat} = {\rm rms}\sqrt{N_{\rm beam}} \quad (6)$$

is related to the rms of the image in the integration area (and, in the case of halos, to the fitting process; see Sect. 5.1). The systematic error,

$$\sigma_{\rm sys} = \delta_{\rm cal} S_{\rm diffuse}, \quad (7)$$

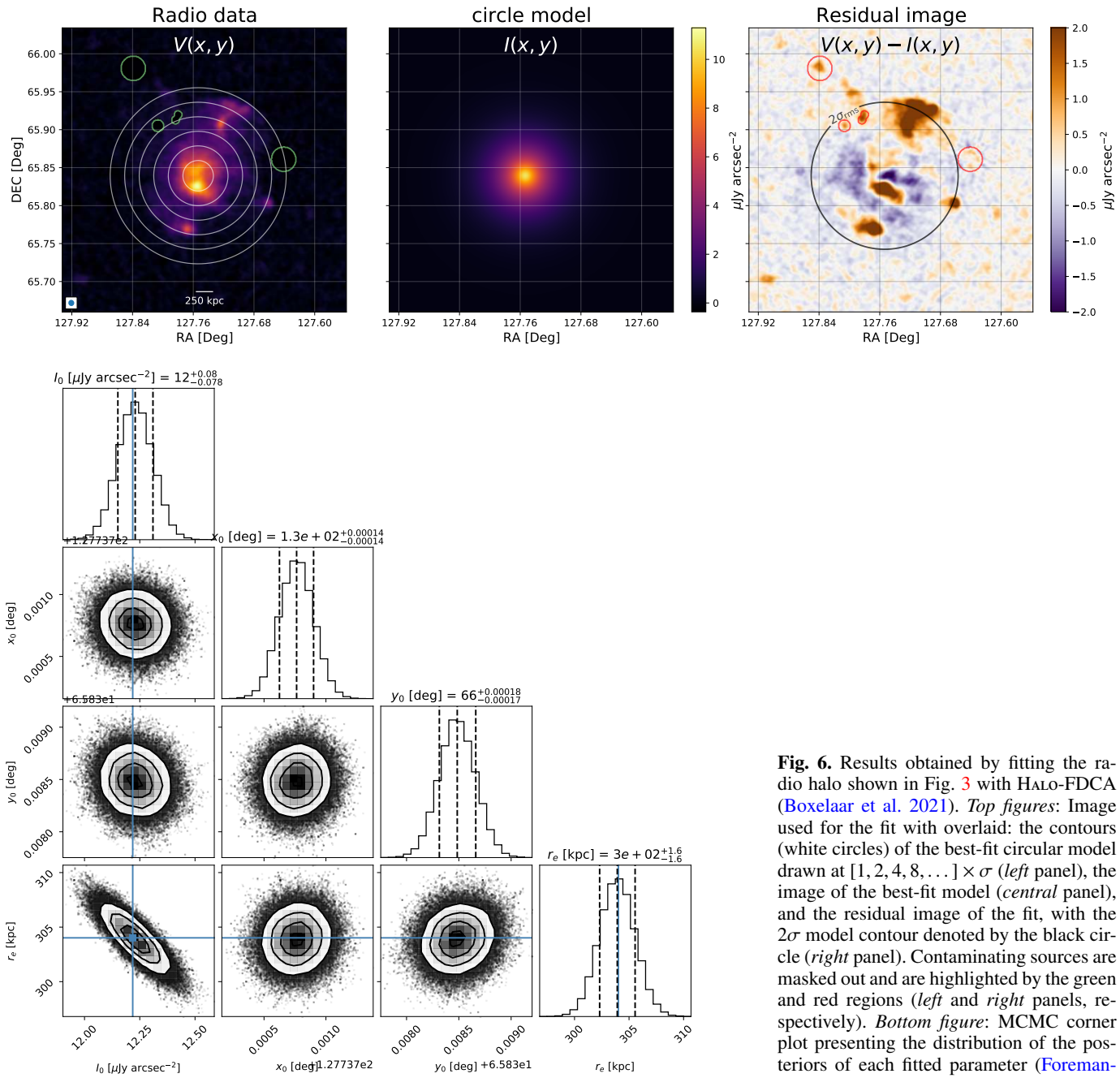

Fig. 6. Results obtained by fitting the radio halo shown in Fig. 3 with HALO-FDCA (Boxelaar et al. 2021). *Top figures*: Image used for the fit with overlaid: the contours (white circles) of the best-fit circular model drawn at $[1, 2, 4, 8, \dots] \times \sigma$ (*left* panel), the image of the best-fit model (*central* panel), and the residual image of the fit, with the 2σ model contour denoted by the black circle (*right* panel). Contaminating sources are masked out and are highlighted by the green and red regions (*left* and *right* panels, respectively). *Bottom figure*: MCMC corner plot presenting the distribution of the posteriors of each fitted parameter (Foreman-Mackey et al. 2013).

is given by the uncertainty of the flux scale calibration, $\delta_{\rm cal}$, which is set to 10% for LoTSS-DR2 (see Sect. 3.2 and Shimwell et al. 2022). The subtraction error,

$$\sigma_{\rm sub} = \xi_{\rm res} S_{\rm discrete}, \tag{8}$$

takes into account the presence of possible residuals in the diffuse emission region from the discrete sources that were subtracted in the *uv*-plane. To determine the fraction of residual contaminating emission, $\xi_{\rm res}$, we visually inspected the images used for the subtraction for a subsample of clusters characterized by different values of flux density in discrete sources, and found that the following percentages,

$$\xi_{\rm res} = \begin{cases} 16\% & \text{if } S_{\rm discrete} < 10 \text{ mJy} \\ 8\% & \text{if } 10 \text{ mJy} < S_{\rm discrete} < 100 \text{ mJy} \\ 4\% & \text{if } 100 \text{ mJy} < S_{\rm discrete} < 1000 \text{ mJy} \\ 2\% & \text{if } S_{\rm discrete} > 1000 \text{ mJy} \end{cases}, \tag{9}$$

provide a good approximation to quantify the level of contamination in our measurements.

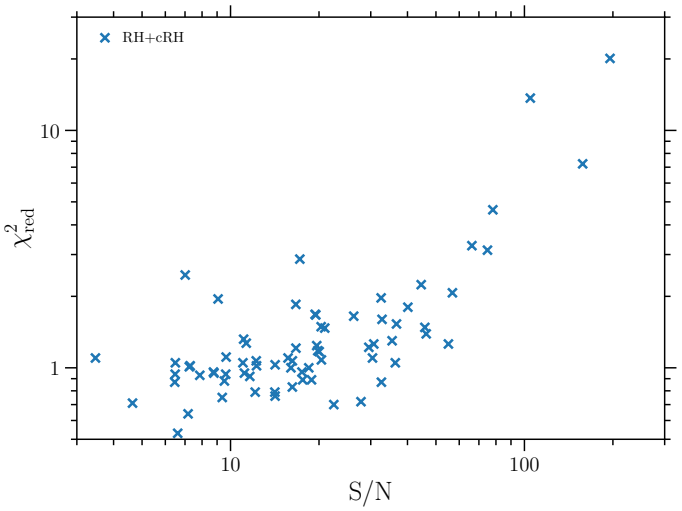

Fig. 7. $\chi^2_{\rm red}$ vs. S/N (i.e., the ratio between the integrated flux density and its fitting uncertainty) for the radio halos and candidate radio halos in our sample. The positive trend indicates that deviations from the exponential model become evident only for the halos that are detected with sufficient significance.

5.1. Radio halos

We employed the Halo-Flux Density CAlculator[7] (Halo-FDCA; Boxelaar et al. 2021) to measure the integrated flux density from the observed radio halos. This code fits the two-dimensional surface brightness profile with a Markov chain Monte Carlo (MCMC) method that estimates the best-fit parameters and associated uncertainties. As proposed by Murgia et al. (2009), for the fitting we assume exponential profiles in the form

$$I(r) = I_0 e^{-G(r)}\,, \tag{10}$$

where the fitted parameters are I_0, which is the central brightness, and $G(r)$, which is a function that determines the model morphology (i.e., circular, elliptical or skewed; see Boxelaar et al. 2021 for more details). As done for the LoTSS-DR1 cluster sample (van Weeren et al. 2021), we primarily used a simple circular exponential model to fit the discrete-source-subtracted images that were obtained with a Gaussian *uv* taper corresponding to 50 kpc at the cluster redshift. If the signal to noise in these images was low or the emission was clearly non circular, we instead used the discrete-source-subtracted images with *uv* taper of 100 kpc or of the elliptical exponential model. In total, the circular model has four free parameters: I_0, the coordinates of the center (x_0 and y_0), and a single *e*-folding radius (r_1). The elliptical model has two additional free parameters: a second *e*-folding radius (r_2) and a rotation angle (ϕ).

Prior to fitting the radio halos we carefully examined the images for contaminating extended sources that had been poorly subtracted, such as tailed radio galaxies and radio relics. We also identified regions affected by residual calibration errors. These problematic regions were manually masked during the fitting. In order to reduce the processing time and the size of the area to manually inspect for masking, we provided as input to Halo-FDCA images with a FoV reduced to approximately $1.5r_{500} \times 1.5r_{500}$.

A qualitative assessment of the fit quality can be done by inspecting the residual images and corner plots produced by Halo-FDCA, which we have made publicly available for each cluster on the project website. An example of these plots for the prominent radio halo that is hosted in the cluster PSZ2 G149.75+34.68 (see Fig. 3) is reported in Fig. 6. We note that Halo-FDCA returns the signal-to-noise ratio (S/N) and the $\chi^2_{\rm red}$ of the fit, which can also be used to assess the fit quality. However, we urge caution in interpreting these values. The S/N in Halo-FDCA is defined as the integrated flux density value divided by the uncertainty introduced by the fit (which is based on the image noise and the number of data points related to the area of the halo), and hence it is not a parameter that determines the significance of the detection. The $\chi^2_{\rm red}$ instead is calculated from the difference between the fitted exponential model and the data, and high $\chi^2_{\rm red}$ values may suggest that a halo has a lot of substructure. For example, this is the case of the halo shown in Fig. 6, where $\chi^2_{\rm red} = 7.23$. We note a positive trend between S/N and $\chi^2_{\rm red}$ for the radio halos and candidate radio halos in our sample (Fig. 7), indicating that the exponential model, while being a reasonable description of the data, may be affected by the presence of asymmetries and substructures that become evident only when the data are of sufficient statistical quality.

To demonstrate the performance of Halo-FDCA, in Appendix C we compare the integrated flux density obtained by integrating the flux density within a circle (or ellipse, depending on the model used in Halo-FDCA) that roughly encompasses the 2σ contour of the radio halo ($S_{2\sigma}$) with that obtained with Halo-FDCA ($S_{\rm fit}$). We generally see good agreement between the two quantities, but, as detailed in the Appendix, we found that the fitting could not be done reliably due to the low significance of the emission for 10 out of the 83 fitted radio halos and candidate halos. These sources are reported as RH*/cRH* in Table A.1 and their integrated flux densities cannot be determined accurately with current data. For all halos except PSZ2 G107.10+65.32 and PSZ2 G139.18+56.37 we use as reference the Halo-FDCA derived integrated flux density. For these two clusters there is significant substructure and we instead derived the integrated flux density by summing the pixels within the 2σ contour level.

As suggested by Murgia et al. (2009), when calculating the Halo-FDCA derived integrated flux densities we integrated the best-fit models up to a radius of three times the *e*-folding radius. This choice leads to a flux density that is ~80% of the one that would be obtained by integrating the model up to infinity and is motivated by the fact that halos do not extend indefinitely.

The quantities derived for the radio halos and candidate radio halo in our sample are reported in Table A.3.

5.2. Radio relics

The integrated flux density of radio relics was computed in polygonal regions encompassing the 2σ contour of the diffuse emission. In the process, particular care was devoted to excluding possible artifacts due to calibration errors and/or other contaminating extended sources in the cluster. As done for halos, we primarily used the images obtained with a Gaussian *uv* taper corresponding to 50 kpc at the cluster redshift with discrete sources removed. In a handful of relics (PSZ2 G089.52+62.34 N2, PSZ2 G091.79-27.00, PSZ2 G113.91-37.01 S, PSZ2 G166.62+42.13 E, and PSZ2 G205.90+73.76 N/S), we instead used the discrete-source-subtracted images with *uv* taper of 100 kpc, where the integrated flux density of the relics is >10% than that obtained in the 50 kpc images. From inspection of the images of PSZ2G190.61+66.46, we found that the relic was partially included in the model for source subtraction and hence that a small fraction of the relic emission was removed. Since there are no

[7] https://github.com/JortBox/Halo-FDCA

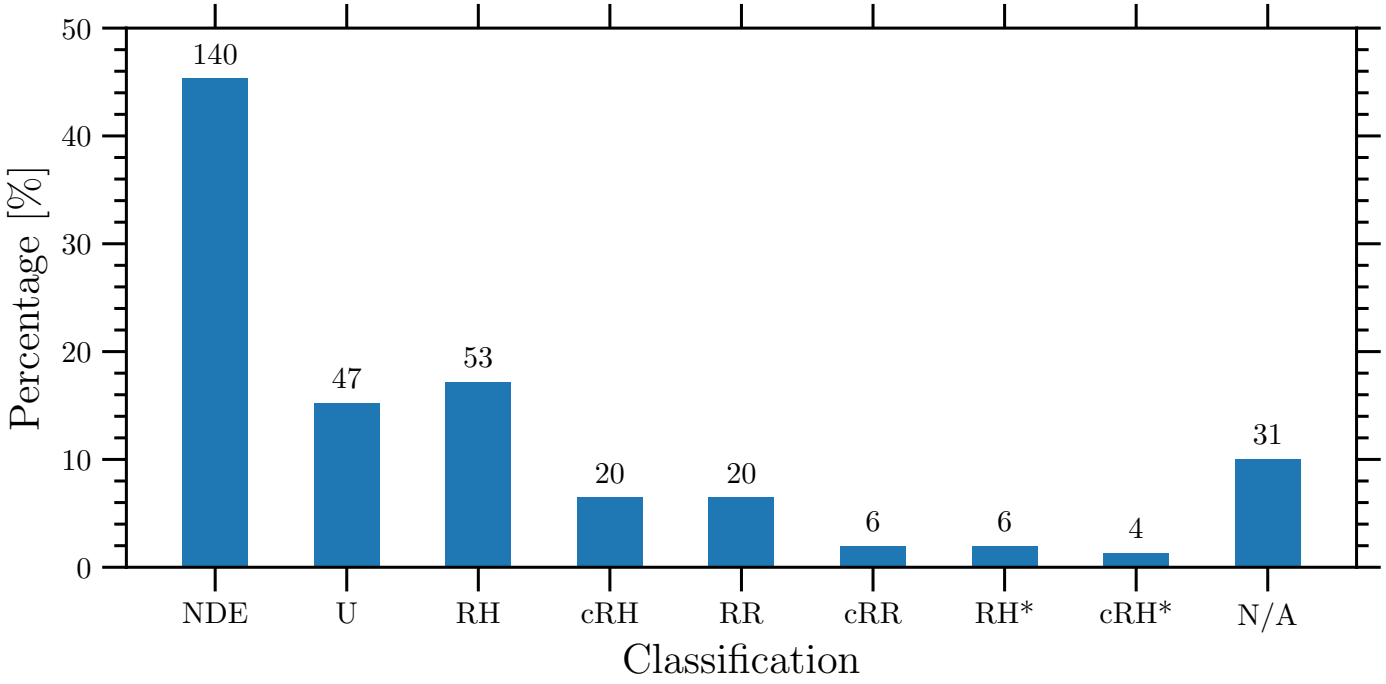

Fig. 8. Summary of the number of clusters classified in our sample divided per category (NDE=no diffuse emission; U=uncertain; RH=radio halo; RR=radio relic; c=candidate; *=flux density measurement not reliable; N/A=not applicable). We note that a cluster can be classified under multiple categories, such as both RH and RR. The percentage on the y axis is with respect to the total number of PSZ2 in LoTSS-DR2 (309 targets).

compact sources in the region of the relic, only for this target we chose to use the 50 kpc image prior to the source subtraction to measure its properties.

We estimated the LLS of each relic by computing the distance between the pixels above 2σ with the largest separation in the diffuse emission. Owing to the reliability of the flux density within a beam, the error in the measured LLS corresponds to the size of the restoring beam of the image.

The downstream extension of radio relics, or relic width, often varies significantly across the extent of the relic. Additionally, the irregular shapes of some radio relics make it challenging to decide at which position to define and measure the width. We therefore decided to take a statistical approach to measuring the width of a relic. The straight line joining the LLS pixel pair typically lies approximately perpendicular to the width direction. This was verified by eye. Therefore, by measuring the largest separation between relic pixels along the line perpendicular to the LLS at each pixel along the LLS, we obtained an estimate of the width at all points along the relic. We then took the median of these width measurements as the characteristic relic width and adopt as error the standard deviation of the measurements, which reflects the spread of values obtained.

We used the coordinates of X-ray centroids as reference points for calculating the projected distance of the radio relics from the clusters. The X-ray centroid of each cluster was calculated within a region of r_{500} centered at the coordinates reported in the PSZ2 catalog. Only for PSZ2 G107.10+65.32 S, we used a region of 500 kpc centered at the X-ray peak due to the PSZ2 coordinates being outside this subcluster.

Due to possible projection effects, the shock front associated with the relic may not be located at the sharp surface brightness edge of the relic, but at the brightest region of the relic. We therefore chose to define the position of the relic as the center of the brightest 10% of pixels within the relic, weighted by their flux density. The distance between the relic and the centroid of the cluster X-ray emission ($D_{\mathrm{RR-c}}$) as well as the separation between double relics ($D_{\mathrm{RR-RR}}$) were computed from these coordinates. We include an additional error to account for the projection between the relic and X-ray centroid axis. Since the merger axis of clusters hosting double radio relics is approximately on the plane of the sky, the additional error corresponds to a projection of 10°. For all other relics we take an offset of 30°.

The quantities derived for the radio relics and candidate radio relics in our sample are reported in Table A.4.

6. Results and discussion

6.1. Number and distribution of sources

With 309 objects, the LoTSS-DR2/PSZ2 sample represents the largest statistical sample of galaxy clusters observed with highly sensitive low-frequency observations that has been ever used to search for and study diffuse synchrotron emission in the ICM. The number of clusters divided per category as defined in Sect. 4 is summarized in Fig. 8. We found 73 clusters hosting a radio halo (i.e., 53 RH and 20 cRH), 26 clusters hosting one or more relics (i.e., 20 RR and 6 cRR), and 47 clusters with diffuse emission of uncertain origin. Additional 10 clusters are found to host a radio halo from visual inspection but since the surface brightness profile fittings were of poor quality they were reported with an asterisk in Fig. 8 and Table A.1 (these are the 6 RH* and 4 cRH* discussed in Appendix C). No diffuse radio emission from the ICM was found for 140 targets while for 36 objects it was not possible to investigate the presence of diffuse emission either due to the impossibility of applying the extraction + recalibration method described in Sect. 3.1 (5 out of 36) or due to the bad image quality (31 out of 36). Notes on individual clusters (including references on previous studies employing radio

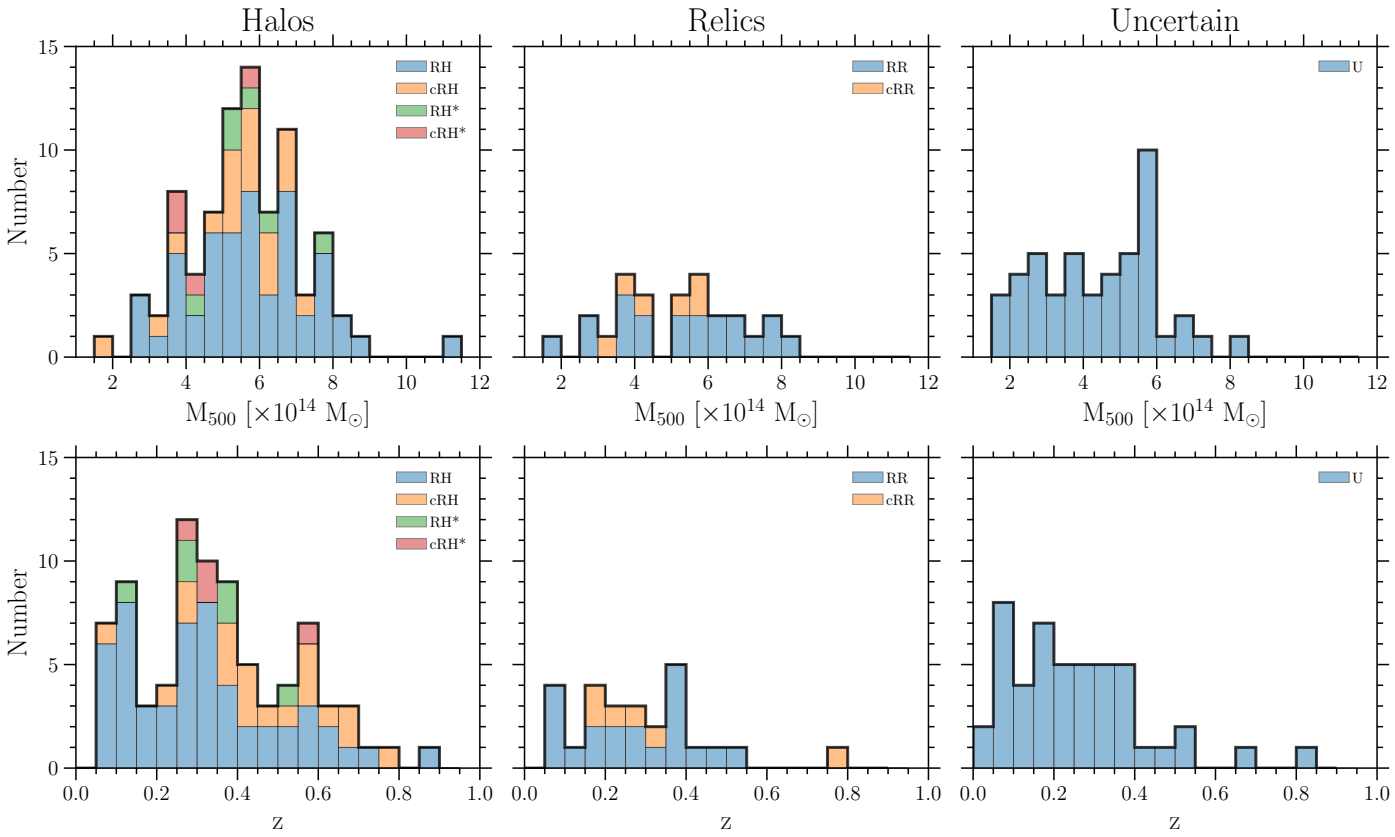

Fig. 9. Histograms of the mass (*top* panels) and redshift (*bottom* panels) distribution for the main categories of objects classified in this work.

observations) are reported in Appendix D.

The number of clusters with newly discovered radio halos and relics in our sample is 50 (i.e., 50% of the total number of halo and relic detections) and these clusters are highlighted in Table A.1. These new discoveries consist of 35 clusters hosting a radio halo (i.e., 21 RH and 14 cRH, namely 48% of the number of halo detections) and 15 clusters hosting one or more radio relics (i.e., 9 RR and 6 cRR, namely 58% of the number of relic detections). In addition, all the 10 halos classified with an asterisk (i.e., 6 RH* and 4 cRH*) except PSZ2 G118.34+68.79 (see van Weeren et al. 2021) are reported in this work for the first time. In Fig. 9 we show the mass and redshift distribution for the clusters hosting halos, (one or more) relics, and uncertain sources in our sample.

We detected radio halos over the entire M_{500} range of the PSZ2 sample we studied, which spans nearly one order of magnitude. The bulk of detections occur in the mass range 5×10^{14} $M_\odot \lesssim M_{500} \lesssim 7 \times 10^{14}$ $M_\odot$. In Cassano et al. (in preparation) we discuss the occurrence of halos with the cluster mass, properly taking into account the selection effects and completeness of the PSZ2 catalog. Of particular interest is the large number of detections of halos in clusters with a mass $M_{500} < 5 \times 10^{14}$ $M_\odot$ (i.e., 17 RH, 4 cRH, 3 cRH*, and 1 cRH*). This mass regime is poorly studied and it has been disclosed only very recently thanks to sensitive observations with new generation instruments (e.g., Hlavacek-Larrondo et al. 2018; Hoang et al. 2019; van Weeren et al. 2021; Botteon et al. 2019a, 2021a,b; Duchesne et al. 2021, for recent works). We note that the candidate radio halo in PSZ2 G192.77+33.14 [$M_{500} = (1.66 \pm 0.20) \times 10^{14}$ $M_\odot$], if confirmed, would be the least massive system presently known to host a radio halo. Radio halos in our sample cover also a wide redshift range, from $z = 0.05$ (PSZ2 G192.77+33.14) up to $z = 0.888$ (PSZ2 G160.83+81.66; see Di Gennaro et al. 2021a,b), with the bulk located at $0.25 \lesssim z \lesssim 0.4$. The discovery of bright radio halos in systems (partially overlapping with our sample) with $z > 0.6$ has been recently made possible thanks to LoTSS observations (Cassano et al. 2019; Di Gennaro et al. 2021a). The evolution of the radio halo properties with redshift will be discussed in Cassano et al. (in preparation). Finally, we note that in Fig. 9 we have not reported the candidate radio halo in PSZ2 G144.23-18.19, which is our only detection in a cluster without redshift and mass, while the double radio halo cluster in PSZ2 G107.10+65.32 (see Botteon et al. 2018) was counted only once.

The radio relic sample has a broad distribution both in terms of M_{500} and z (despite being more limited in size with respect to that of halos). Unlike halos, we find only one radio relic in clusters at $z > 0.6$, namely in PSZ2 G069.39+68.05 ($z = 0.762$). This relic is claimed here for the first time. The least massive cluster in our sample is also that with the lowest redshift: PSZ2 G089.52+62.34 [$M_{500} = (1.83 \pm 0.19) \times 10^{14}$ $M_\odot$ at $z = 0.07$], which was already reported in van Weeren et al. (2021). The total number of relic sources is 35, and the number of clusters hosting more than one relic in the ICM is 8. We only found 6 cases of classic, symmetric (i.e., located in diametrically opposite sides of the cluster), double radio relic systems (PSZ2 G071.21+28.86, PSZ2 G099.48+55.60, PSZ2 G113.91-37.01, PSZ2 G165.46+66.15, PSZ2 G181.06+48.47, PSZ2 G205.90+73.76). We remark that clusters hosting more than one relic are reported only once in Fig. 9. The statistical analysis of radio relics is presented in Jones et al. (in preparation).

Clusters with uncertain diffuse emission are mainly observed for $z < 0.4$ and $M_{500} < 6 \times 10^{14}$ $M_\odot$. From visual inspection, we

expect that a large fraction of these systems may host a radio halo (which, however, cannot be firmly claimed at the moment), while a smaller fraction may contain different kinds of sources in the ICM. Follow-up observations are required to confirm the nature of the emission observed. These clusters are not considered to derive scaling relations in Cuciti et al. (in preparation) and Jones et al. (in preparation), while for the study of the occurrence of radio halos in Cassano et al. (in preparation) we consider the two extreme cases where all or none of the uncertain sources are radio halos.

6.2. Classification

In this work and in the accompanying papers of the series we focus on the detection and characterization of radio halos and relics in the PSZ2 sample. These types of emissions are the most widely studied classes of diffuse synchrotron sources in the ICM, and are arguably the best defined and understood.

Diffuse sources in our sample were classified by visually inspecting LOFAR 120−168 MHz images at different resolutions, with and without discrete sources removed. We also made use of overlays of our radio data with optical and X-ray data when available. The most challenging aspect of the inspections was to disentangle the sources of interest (halos and relics) from other contaminating sources such as AGN and phoenixes and also from calibration artifacts. This separation relied upon the high resolution of LOFAR and availability and high quality of the auxiliary data sets. However, in some cases it still remained very challenging to conclusively classify the emission. Indeed, low-frequency observations are very sensitive to low-energy relativistic electrons in the ICM, which even if emitted from a single compact region can occupy a significant fraction of the cluster volume due to their long lifetimes. As a consequence, the filling factor of emission associated with AGN increases at low frequency, and diffuse emission of somewhat uncertain origin and low significance can be identified almost in all clusters. This highlights the role of seed electrons in the formation of cluster-scale diffuse sources, which are an important ingredient for (re)acceleration models.

Although we found the application of the decision tree (Fig. 4) useful to make the classification less biased and more reproducible, we acknowledge that the visual inspection of the 309 objects in our sample is a painstaking procedure. It is clear that the strategy used in this work needs further development to properly assess significantly larger cluster samples or to eventually conduct a blind search for cluster emission. In this respect, machine-based techniques represent an appealing solution to classify the emission in large object samples (e.g., Aniyan & Thorat 2017; Alhassan et al. 2018; Domínguez Sánchez et al. 2018; Lukic et al. 2018, 2019; Sadeghi et al. 2021; Vavilova et al. 2021). As part of this work, we have made public all our images and the detailed results of our decision-tree-based classification, which we hope can provide a good training set for algorithms that attempt either the full classification or to aid the automation at specific intersections in a decision-tree-type approach. Another approach would be establishing a citizen science project dedicated to galaxy clusters (i.e., a LOFAR Galaxy Clusters Zoo) with the goal of distributing the classification work among citizen scientists, similarly to what is currently done by the LOFAR Radio Galaxy Zoo[8] project, which has the aim of joining different components of the same radio galaxies observed by LoTSS and identifying their optical counterparts.

As a final note, the unprecedented high resolution and high sensitivity at low frequencies provided by LOFAR have the potential of probing previously unseen features of halos and relics, but also to unveil new kinds of emission in the ICM. Collecting the large variety of source morphologies in clusters in an automated way (e.g., Gheller et al. 2018; Mostert et al. 2021) will then help us to study the nature of the sources and the role of the surrounding environment to shape the radio emission.

6.3. Prospects

The fraction of identifications in each of our classifications with respect to the full LoTSS-DR2 sample is shown Fig. 8. In the following, reported fractions were computed excluding the 36 targets of the sample for which we could not verify the presence of diffuse emission in the radio images (i.e., 5 not extracted and 31 N/A). The reported uncertainties are computed based on Poisson statistics.

The fractions of PSZ2 clusters in which a radio halo or one or more radio relics is claimed in this work are $19 \pm 9\%$ and $7 \pm 5\%$, respectively, and increase to $27 \pm 10\%$ and $10 \pm 6\%$ if candidates are also included. If the 10 halos classified with an asterisk for which we could not provide a reliable flux density measurement (Appendix C) are also taken into account, the fraction of clusters with a radio halo detected rises further, to $30 \pm 11\%$. The fraction of clusters hosting sources with uncertain origin is $17 \pm 8\%$, while that of targets that do not show the presence of diffuse synchrotron emission in the ICM is $51 \pm 14\%$.

In our earlier work (van Weeren et al. 2021) we presented the first statistical analysis of galaxy clusters observed with LoTSS and studied the 26 PSZ2 clusters residing in the ~420 deg^2 covered by LoTSS-DR1 (this region is contained within LoTSS-DR2). We found that $73 \pm 15\%$ of PSZ2 clusters hosted some type of diffuse ICM related radio emission. More specifically, $62 \pm 15\%$ and $27 \pm 10\%$ PSZ2 clusters hosted a radio halo or one or more relics (including candidates), respectively. When comparing the fraction of diffuse emission in LoTSS-DR1 with that of LoTSS-DR2 one should take into account three important factors. Firstly, the LoTSS-DR1 area is on average more sensitive than LoTSS-DR2, as it covers a sky area above declination +45°, while LoTSS-DR2 goes down to declination +16°, where the sensitivity of LOFAR is reduced (Shimwell et al. 2022). This observational limitation makes the detection of faint ICM emission more challenging and likely biases low the fraction of extended sources in LoTSS-DR2 compared to LoTSS-DR1. Secondly, the area covered by LoTSS-DR1 comprises a relatively small region of the sky, about 2% of the northern sky, and may therefore be affected by cosmic variance. LoTSS-DR2 instead spans about 27% of the northern sky, enabling the possibility of performing reliable statistical studies. Thirdly, 28 PSZ2 entries in the LoTSS-DR2 sample (i.e., 9% of the total) lack z and M_{500}, and are not confirmed galaxy clusters at the moment, while all the PSZ2 detections in LoTSS-DR1 are confirmed galaxy clusters. If the sources without z and M_{500} in LoTSS-DR2 were *Planck* false detections, they should be rejected from the sample, resulting in an increase in the fraction of clusters hosting diffuse radio emission in the ICM (as all these 28 entries except PSZ2 G144.23-18.19 have been classified as NDE). We checked the quality flag `Q_NEURAL` reported in the PSZ2 catalog for these 28 entries and found that 15 have `Q_NEURAL<0.4`, which the threshold below which Aghanim et al. (2015) classify low reliability detections. This suggests that about half of the clusters for which we do not have z and M_{500} are likely spurious *Planck* detections.

The area covered by LoTSS-DR2 is ideal to study the extra-

[8] `http://lofargalaxyzoo.nl`

galactic sky as it avoids regions at low Galactic latitude and low-declination fields (i.e., between declination 0° and +15°), where the sensitivity of LoTSS is generally a factor of 2−3 lower than the nominal survey noise[9]. Compared to LoTSS-DR1, it has a sky coverage ∼13 times larger (5634 deg^2 vs. 424 deg^2) and it samples a broader declination and right ascension range. This makes the new data release more representative of the quality of LoTSS for extragalactic studies. We thus use our findings to refine the predictions on the number of PSZ2 sources that will be found to contain relics and halos at the completion of LoTSS.

We consider that there are 835 detections in the PSZ2 catalog above a declination of 0° and assume a uniform sensitivity for LoTSS for simplicity. We note that the presence of the Galactic plane is taken into account in the PSZ2 selection due to the lack of *Planck* detections in the zone of avoidance. The results found in LoTSS-DR2 indicate that we will find 251 ± 92 clusters that host a halo and 83 ± 50 clusters that host one or more relics (including candidates), and, as in our study, approximately half of them should be new discoveries. When extrapolating the number of halos, we considered the fraction of 30 ± 11%, which takes into account also the ten halos reported with an asterisk, as in these systems the visual inspection and classification tree led to the class of RH or cRH. If we assume that also all uncertain sources trace a halo, we obtain a conservative upper limit on the number of clusters hosting a radio halo that LoTSS should find in PSZ2 clusters at its completion, namely < 401 ± 117. By considering the number of relic sources found in LoTSS-DR2, we instead predict that at the completion of the survey LoTSS will have observed 109 ± 58 radio relics in PSZ2 clusters.

In the context of the turbulent re-acceleration models for radio halos, Cassano et al. (2010a, 2012) predicted the observation of 350−450 radio halos at $z \leq 0.6$ in LoTSS, while the number of radio relics expected to be observed in LoTSS according to Nuza et al. (2012) is ∼2500. As these model expectations were not tailored for PSZ2 clusters, the comparison between the number of halos and relics at completion of LoTSS and the extrapolations obtained from our analysis of the LoTSS-DR2/PSZ2 sample is not straightforward. In this respect, the thoroughly statistical analysis of the results obtained for the PSZ2 clusters in LoTSS-DR2 and implications on our understanding of halos and relics will be presented in the forthcoming papers of the series, where expectations will be further refined by considering: the sensitivity of present observations, the PSZ2 selection functions, and the new $P_{150} - M_{500}$ correlations. Moreover, as radio halos and relics can be found in LoTSS even in non-PSZ2 clusters, a census of diffuse radio emission in non-PSZ2 clusters in LoTSS-DR2 is also currently ongoing (Hoang et al. 2022).

An important parameter to test the models of particle acceleration in the ICM is the spectrum of diffuse emission. For example, turbulent re-acceleration models predict the existence of a population of radio halos with steep spectra while spectral gradients in relics depend on the mechanisms of particle (re)acceleration at cluster shocks. Interestingly, we note that about half of the radio halos reported in this work are new discoveries (see Sect. 6.1) and the turbulent re-acceleration scenario predicts that about half of the radio halos in LoTSS should have ultra-steep spectra (Cassano et al. 2012). If follow up observations of the radio halos in LoTSS-DR2 will confirm that about 50% of them have very steep spectra, this would be an important corroboration of such a class of models. Still, since LoTSS is currently exploring an uncharted territory in terms of resolution and sensitivity compared to other completed surveys, it is not yet possible to perform spectral analysis for the full cluster sample. In this respect, we have planned a series of targeted observations for a selected number of objects with MeerKAT, VLA, and uGMRT. For a systematic study, ongoing and future sensitive radio surveys covering the northern sky, such as LoLSS (de Gasperin et al. 2021), LoDeSS[10], APERture Tile In Focus (Apertif; Hess et al., in preparation), and VLA Sky Survey (VLASS; Lacy et al. 2020), will supplement LoTSS providing a multifrequency view of clusters that will be critical to investigate the statistics of the spectral properties of halos and relics as well as to properly disentangle diffuse sources from the emission of AGN, allowing us to determine the role of seed relativistic electrons in the ICM.

The presence of X-ray data is critical for the classification of diffuse sources in the ICM, and therefore the ongoing *eROSITA* All-Sky Survey (eRASS; Merloni et al. 2012; Predehl et al. 2021) will be fundamental for providing the X-ray detection of many clusters that currently do not have pointed *XMM-Newton* or *Chandra* observations (i.e., about half of the targets in our sample). This instrument will also allow the detection of low-mass and/or high-z clusters (Pillepich et al. 2012) that are currently not confirmed or missed by *Planck* due to its low sensitivity. Indeed, combining X-ray and SZ surveys is particularly efficient to find new galaxy clusters and derive their mass (see, e.g., ComPRASS; Tarrío et al. 2019). The potential of the joint analysis of LOFAR and *eROSITA* observations of galaxy clusters has been demonstrated by recent papers (e.g., Ghirardini et al. 2021; Pasini et al. 2021; Brienza et al. 2021). Until the eRASS data are publicly released, we are planning to follow-up a subsample of clusters with *Chandra* and/or *XMM-Newton*.

Finally, we note that there are opportunities to further improve the image quality with respect to that presented in this paper. This could be achieved by reapplying the extraction + self-calibration step and fine-tuning the parameters of the self-calibration (van Weeren et al. 2021). The subtraction of discrete sources can also be more careful than that obtained during the analysis of this sample. Moreover, the addition of LOFAR international baselines will help to improve the calibration of the targets affected by the sidelobes of a central bright AGN, enabling the search for diffuse emission in regions that cannot be thoroughly examined with the current calibration. In this respect, we note that a number of targets presented in this sample will be the subject of focused studies in the future (see Appendix D).

7. Conclusions

We have presented the largest statistical sample of galaxy clusters used to date to search for and study diffuse synchrotron sources in the ICM. We examined the 120−168 MHz radio emission from 309 galaxy clusters selected from PSZ2 that span a redshift and mass range of $0.016 < z < 0.9$ and 1.1×10^{14} M$_\odot$ $< M_{500} < 11.7 \times 10^{14}$ M$_\odot$, respectively, and have been covered by LoTSS-DR2. We produced radio images with different resolutions and with or without the discrete source subtracted as well as overlays with Pan-STARRS optical images for all the targets in our sample. When available, we also used targeted *Chandra* and *XMM-Newton* observations to compare the radio emission with that of the X-rays and derive morphological parameters of

[9] The sensitivity of LoTSS observations scales with the elevation of the target as $A \times \cos(90° - \text{elevation})^{-2}$, where $A = 63$ μJy beam^{-1} and the dependence on elevation is fixed according to the projected size of the LOFAR stations (Shimwell et al. 2022).

[10] The LOFAR Decametre Sky Survey is a groundbreaking 14−30 MHz survey that will cover the sky above declination +20°.

the ICM. All these images are publicly available on the project website [11].

We divided the diffuse synchrotron emission into the classes of halos, relics, and uncertain sources. The physical properties of halos and relics have been collected into tables (also available on the website) and are used in Cassano et al. (in preparation), Cuciti et al. (in preparation), and Jones et al. (in preparation) to discuss their statistical properties, such as occurrence and scaling relations. Overall, we found 83 clusters that host a radio halo and 26 clusters that host one or more radio relic (including candidates), of which about half are new discoveries. These numbers correspond to a detection fraction in our sample of $30 \pm 11\%$ and $10 \pm 6\%$, respectively. Based on these results, we expect to find 251 ± 92 cluster that host a halo and 83 ± 50 clusters that host at least one relic in the PSZ2 catalog at the completion of LoTSS. Other searches are being made to examine different cluster samples and try to gauge how many more halos and relics can be found in LoTSS in non-PSZ2 clusters (Hoang et al. 2022).

In the future, LoTSS will benefit from the synergy of complementary radio surveys (e.g., LoLSS, LoDeSS, and Apertif), which will be fundamental for studying the spectral properties of the observed sources. The all-sky survey with *eROSITA* will enable a systematic comparison of the radio and X-ray properties of the PSZ2 clusters as well as the discoveries of new galaxy clusters (especially with low mass and at high z).

Acknowledgements. We thank the anonymous referee for constructive comments that helped to improve the presentation of our results. ABot and RJvW acknowledge support from the VIDI research programme with project number 639.042.729, which is financed by the Netherlands Organisation for Scientific Research (NWO). RC, FG, MR and GB acknowledge support from INAF mainstream project 'Galaxy Clusters Science with LOFAR' 1.05.01.86.05. VC and GDG acknowledge support from the Alexander von Humboldt Foundation. XZ acknowledges support from Chinese Scholarship Council (CSC) and thanks Vittorio Ghirardini for useful discussions. AS is supported by the Women In Science Excel (WISE) programme of the NWO, and acknowledges the World Premier Research Center Initiative (WPI) and the Kavli IPMU for the continued hospitality. RJvW and CG acknowledge support from the ERC-Stg ClusterWeb 804208. MB and FdG acknowledge support from the Deutsche Forschungsgemeinschaft under Germany's Excellence Strategy - EXC 2121 "Quantum Universe" - 390833306. DNH and ABon acknowledge support from ERC-Stg DRANOEL 714245. MJH acknowledges from the UK Science and Technology Facilities Council [ST/V000624/1]. AI acknowledges the Italian PRIN-Miur 2017 (PI A. Cimatti). ABon acknowledges support from MIUR FARE grant "SMS". AD acknowledges support by the BMBF Verbundforschung under the grant 05A20STA. LOFAR (van Haarlem et al. 2013) is the LOw Frequency ARray designed and constructed by ASTRON. It has observing, data processing, and data storage facilities in several countries, which are owned by various parties (each with their own funding sources), and are collectively operated by the ILT foundation under a joint scientific policy. The ILT resources have benefitted from the following recent major funding sources: CNRS-INSU, Observatoire de Paris and Université d'Orléans, France; BMBF, MIWF-NRW, MPG, Germany; Science Foundation Ireland (SFI), Department of Business, Enterprise and Innovation (DBEI), Ireland; NWO, The Netherlands; The Science and Technology Facilities Council, UK; Ministry of Science and Higher Education, Poland; Istituto Nazionale di Astrofisica (INAF), Italy. This research made use of the Dutch national e-infrastructure with support of the SURF Cooperative (e-infra 180169) and the LOFAR e-infra group, and of the LOFAR-IT computing infrastructure supported and operated by INAF, and by the Physics Dept. of Turin University (under the agreement with Consorzio Interuniversitario per la Fisica Spaziale) at the C3S Supercomputing Centre, Italy. The Jülich LOFAR Long Term Archive and the German LOFAR network are both coordinated and operated by the Jülich Supercomputing Centre (JSC), and computing resources on the supercomputer JUWELS at JSC were provided by the Gauss Centre for Supercomputing e.V. (grant CHTB00) through the John von Neumann Institute for Computing (NIC). This research made use of the University of Hertfordshire high-performance computing facility and the LOFAR-UK computing facility located at the University of Hertfordshire and supported by STFC [ST/P000096/1]. The scientific results reported in this article are based in part on data obtained from the *Chandra* Data Archive and on observations obtained with *XMM-Newton*, an ESA science mission with instruments and contributions directly funded by ESA Member States and NASA. SRON Netherlands Institute for Space Research is supported financially by the NWO. This research made use of APLpy, an open-source plotting package for Python (Robitaille & Bressert 2012), Astropy, a community-developed core Python package for Astronomy (Astropy Collaboration et al. 2013, 2018), Matplotlib (Hunter 2007), NumPy (Harris et al. 2020), and SciPy (Virtanen et al. 2020).

[11] https://lofar-surveys.org/planck_dr2.html

References

Adam, R., Goksu, H., Brown, S., Rudnick, L., & Ferrari, C. 2021, A&A, 648, A60
Aghanim, N., Hurier, G., Diego, J. M., et al. 2015, A&A, 580, A138
Aguado-Barahona, A., Barrena, R., Streblyanska, A., et al. 2019, A&A, 631, A148
Alhassan, W., Taylor, A., & Vaccari, M. 2018, MNRAS, 480, 2085
Aniyan, A. & Thorat, K. 2017, ApJS, 230, 20
Astropy Collaboration, Price-Whelan, A. M., Sipőcz, B., et al. 2018, AJ, 156, 123
Astropy Collaboration, Robitaille, T. P., Tollerud, E. J., et al. 2013, A&A, 558, A33
Bacchi, M., Feretti, L., Giovannini, G., & Govoni, F. 2003, A&A, 400, 465
Barrena, R., Streblyanska, A., Ferragamo, A., et al. 2018, A&A, 616, A42
Biava, N., Brienza, M., Bonafede, A., et al. 2021a, A&A, 650, A170
Biava, N., de Gasperin, F., Bonafede, A., et al. 2021b, MNRAS, 508, 3995
Bîrzan, L., Rafferty, D., Brüggen, M., et al. 2020, MNRAS, 496, 2613
Bîrzan, L., Rafferty, D., Cassano, R., et al. 2019, MNRAS, 487, 4775
Blasi, P. & Colafrancesco, S. 1999, Astropart. Phys., 12, 169
Boada, S., Hughes, J. P., Menanteau, F., et al. 2019, ApJ, 871, 188
Bonafede, A., Brüggen, M., van Weeren, R. J., et al. 2012, MNRAS, 426, 40
Bonafede, A., Brunetti, G., Rudnick, L., et al. 2022, arXiv e-prints, arXiv:2203.01958
Bonafede, A., Brunetti, G., Vazza, F., et al. 2021, ApJ, 907, 32
Bonafede, A., Feretti, L., Murgia, M., et al. 2010, A&A, 513, A30
Bonafede, A., Giovannini, G., Feretti, L., Govoni, F., & Murgia, M. 2009, A&A, 494, 429
Botteon, A., Brunetti, G., van Weeren, R. J., et al. 2020a, ApJ, 897, 93
Botteon, A., Cassano, R., Eckert, D., et al. 2019a, A&A, 630, A77
Botteon, A., Cassano, R., van Weeren, R. J., et al. 2021a, ApJ, 914, L29
Botteon, A., Gastaldello, F., Brunetti, G., & Dallacasa, D. 2016, MNRAS, 460, L84
Botteon, A., Giacintucci, S., Gastaldello, F., et al. 2021b, A&A, 649, A37
Botteon, A., Shimwell, T. W., Bonafede, A., et al. 2018, MNRAS, 478, 885
Botteon, A., Shimwell, T. W., Bonafede, A., et al. 2019b, A&A, 622, A19
Botteon, A., van Weeren, R. J., Brunetti, G., et al. 2020b, MNRAS, 499, L11
Boxelaar, J. M., van Weeren, R. J., & Botteon, A. 2021, A&C, 35, 100464
Brienza, M., Morganti, R., Harwood, J. J., et al. 2020, A&A, 638, A29
Brienza, M., Shimwell, T. W., de Gasperin, F., et al. 2021, Nature Astron., 5, 1261
Briggs, D. 1995, in Bulletin of the American Astronomical Society, Vol. 27, American Astronomical Society Meeting Abstracts, 1444
Brown, S. & Rudnick, L. 2011, MNRAS, 412, 2
Brüggen, M., Rafferty, D., Bonafede, A., et al. 2018, MNRAS, 477, 3461
Brüggen, M. & Vazza, F. 2020, MNRAS, 493, 2306
Brunetti, G., Cassano, R., Dolag, K., & Setti, G. 2009, A&A, 507, 661
Brunetti, G. & Jones, T. W. 2014, IJMPD, 23, 30007
Brunetti, G., Zimmer, S., & Zandanel, F. 2017, MNRAS, 472, 1506
Buddendiek, A., Schrabback, T., Greer, C., et al. 2015, MNRAS, 450, 4248
Buote, D. A. 2001, ApJ, 553, L15
Burenin, R. 2017, Astron. Lett., 43, 507
Burenin, R., Bikmaev, I., Khamitov, I., et al. 2018, Astron. Lett., 44, 297
Cassano, R., Botteon, A., Di Gennaro, G., et al. 2019, ApJ, 881, L18
Cassano, R. & Brunetti, G. 2005, MNRAS, 357, 1313
Cassano, R., Brunetti, G., Norris, R. P., et al. 2012, A&A, 548, A100
Cassano, R., Brunetti, G., Röttgering, H. J., & Brüggen, M. 2010a, A&A, 509, A68
Cassano, R., Brunetti, G., & Setti, G. 2006, MNRAS, 369, 1577
Cassano, R., Brunetti, G., Setti, G., Govoni, F., & Dolag, K. 2007, MNRAS, 378, 1565
Cassano, R., Brunetti, G., Venturi, T., et al. 2008, A&A, 480, 687
Cassano, R., Ettori, S., Giacintucci, S., et al. 2010b, ApJ, 721, L82
Chambers, K. C., Magnier, E., Metcalfe, N., et al. 2016, arXiv e-prints, arXiv:1612.05560
Clarke, A., Scaife, A., Shimwell, T. W., et al. 2019, A&A, 627, A176
Clarke, T. E., Randall, S. W., Sarazin, C. L., Blanton, E. L., & Giacintucci, S. 2013, ApJ, 772, 84
Cohen, A. & Clarke, T. E. 2011, AJ, 141, 149
Condon, J., Cotton, W., Greisen, E., et al. 1998, AJ, 115, 1693
Cuciti, V., Cassano, R., Brunetti, G., et al. 2015, A&A, 580, A97

Cuciti, V., Cassano, R., Brunetti, G., et al. 2021, A&A, 647, A50
de Gasperin, F., Dijkema, T. J., Drabent, A., et al. 2019, A&A, 622, A5
de Gasperin, F., Intema, H. T., Shimwell, T. W., et al. 2017, Science Adv., 3, e1701634
de Gasperin, F., Ogrean, G., van Weeren, R. J., et al. 2015, MNRAS, 448, 2197
de Gasperin, F., van Weeren, R. J., Brüggen, M., et al. 2014, MNRAS, 444, 3130
de Gasperin, F., Williams, W. L., Best, P. N., et al. 2021, A&A, 648, A104
Dennison, B. 1980, ApJ, 239, L93
Di Gennaro, G., van Weeren, R. J., Brunetti, G., et al. 2021a, Nature Astron., 5, 268
Di Gennaro, G., van Weeren, R. J., Cassano, R., et al. 2021b, A&A, 654, A166
Domínguez Sánchez, H., Huertas-Company, M., Bernardi, M., Tuccillo, D., & Fischer, J. 2018, MNRAS, 476, 3661
Drabent, A., Hoeft, M., Pizzo, R. F., et al. 2015, A&A, 575, A8
Duchesne, S. W., Johnston-Hollitt, M., & Bartalucci, I. 2021, PASA, 38, e053
Duchesne, S. W., Johnston-Hollitt, M., Zhu, Z.-H., Wayth, R., & Line, J. 2020, PASA, 37, e037
Farnsworth, D., Rudnick, L., Brown, S., & Brunetti, G. 2013, ApJ, 779, 189
Feretti, L., Giovannini, G., Govoni, F., & Murgia, M. 2012, A&A Rev., 20, 54
Feretti, L. & Neumann, D. 2006, A&A, 450, L21
Feretti, L., Orrù, E., Brunetti, G., et al. 2004, A&A, 423, 111
Foreman-Mackey, D., Hogg, D. W., Lang, D., & Goodman, J. 2013, PASP, 125, 306
Fruscione, A., McDowell, J. C., Allen, G. E., et al. 2006, Society of Photo-Optical Instrumentation Engineers (SPIE) Conference Series, Vol. 6270, CIAO: Chandra's data analysis system, 62701V
Gabriel, C., Denby, M., Fyfe, D., et al. 2004, in Astronomical Society of the Pacific Conference Series, Vol. 314, Astron. Data Anal. Softw. Syst. XIII, ed. F. Ochsenbein, M. G. Allen, & D. Egret, 759
George, L. T., Kale, R., & Wadadekar, Y. 2021, MNRAS, 507, 4487
Gheller, C., Vazza, F., & Bonafede, A. 2018, MNRAS, 480, 3749
Ghirardini, V., Bulbul, E., Hoang, D. N., et al. 2021, A&A, 647, A4
Giacintucci, S., Markevitch, M., Cassano, R., et al. 2017, ApJ, 841, 71
Giacintucci, S., Markevitch, M., Venturi, T., et al. 2014, ApJ, 781, 9
Giacintucci, S., Venturi, T., Cassano, R., Dallacasa, D., & Brunetti, G. 2009, ApJ, 704, L54
Giacintucci, S., Venturi, T., Murgia, M., et al. 2007, A&A, 476, 99
Giovannini, G., Bonafede, A., Feretti, L., et al. 2009, A&A, 507, 1257
Giovannini, G. & Feretti, L. 2000, New Astron., 5, 335
Giovannini, G., Feretti, L., Govoni, F., Murgia, M., & Pizzo, R. F. 2006, Astron. Nachrichten, 327, 563
Giovannini, G., Feretti, L., & Stanghellini, C. 1991, A&A, 252, 528
Giovannini, G., Feretti, L., Venturi, T., Kim, K.-T., & Kronberg, P. P. 1993, ApJ, 406, 399
Giovannini, G., Tordi, M., & Feretti, L. 1999, New Astron., 4, 141
Gitti, M. 2013, MNRAS, 436, L84
Gitti, M., Brunetti, G., Feretti, L., & Setti, G. 2004, A&A, 417, 1
Govoni, F., Feretti, L., Giovannini, G., et al. 2001, A&A, 376, 803
Govoni, F., Ferrari, C., Feretti, L., et al. 2012, A&A, 545, A74
Govoni, F., Murgia, M., Giovannini, G., Vacca, V., & Bonafede, A. 2011, A&A, 529, A69
Govoni, F., Murgia, M., Markevitch, M., et al. 2009, A&A, 499, 371
Govoni, F., Orrù, E., Bonafede, A., et al. 2019, Science, 364, 981
Gupta, Y., Ajithkumar, B., Kale, H., et al. 2017, Curr. Sci., 113, 707
Hales, S., Baldwin, J., & Warner, P. 1988, MNRAS, 234, 919
Hales, S., Masson, C., Warner, P., & Baldwin, J. 1990, MNRAS, 246, 256
Hallman, E. J., Alden, B., Rapetti, D., Datta, A., & Burns, J. O. 2018, ApJ, 859, 44
Hardcastle, M. J., Croston, J., Shimwell, T. W., et al. 2019, MNRAS, 488, 3416
Hardcastle, M. J., Gürkan, G., van Weeren, R. J., et al. 2016, MNRAS, 462, 1910
Hardcastle, M. J., Shimwell, T. W., Tasse, C., et al. 2021, A&A, 648, A10
Harris, C. R., Millman, K. J., van der Walt, S. J., et al. 2020, Nature, 585, 357
Hlavacek-Larrondo, J., Gendron-Marsolais, M.-L., Fecteau-Beaucage, D., et al. 2018, MNRAS, 475, 2743
Hoang, D. N., Shimwell, T. W., Osinga, E., et al. 2021a, MNRAS, 501, 576
Hoang, D. N., Shimwell, T. W., van Weeren, R. J., et al. 2018, MNRAS, 478, 2218
Hoang, D. N., Shimwell, T. W., van Weeren, R. J., et al. 2019, A&A, 622, A21
Hoang, D. N., Zhang, X., Stuardi, C., et al. 2021b, A&A, 656, A154
Hoang, D. N., Brüggen, M., Botteon, A., et al. 2022, A&A, submitted
Hodgson, T., Bartalucci, I., Johnston-Hollitt, M., et al. 2021, ApJ, 909, 198
Hoeft, M., Dumba, C., Drabent, A., et al. 2021, A&A, 654, A68
Hogbom, J. & Brouw, W. 1974, A&A, 33, 289
Hotan, A., Bunton, J., Chippendale, A., et al. 2021, PASA, 38, e009
Huber, P. J. 1981, Robust statistics
Hunter, J. D. 2007, Comput. Sci. Eng., 9, 90
HyeongHan, K., Jee, M. J., Rudnick, L., et al. 2020, ApJ, 900, 127
Ignesti, A., Gitti, M., Brunetti, G., Feretti, L., & Giovannini, G. 2017, A&A, 604, A21
Ignesti, A., Shimwell, T. W., Brunetti, G., et al. 2020, A&A, 643, A172
Ignesti, A., Vulcani, B., Poggianti, B. M., et al. 2022, ApJ, 924, 64
Jeltema, T. E. & Profumo, S. 2011, ApJ, 728, 53
Jonas, J. 2009, IEEE Proceedings, 97, 1522
Kale, R. & Gitti, M. 2017, MNRAS, 466, L19
Kale, R., Parekh, V., & Dwarakanath, K. 2018, MNRAS, 480, 5352
Kale, R., Venturi, T., Giacintucci, S., et al. 2013, A&A, 557, A99
Kempner, J. C. & Sarazin, C. L. 2001, ApJ, 548, 639
Kim, K.-T., Kronberg, P. P., Giovannini, G., & Venturi, T. 1989, Nature, 341, 720
Kokotanekov, G., Wise, M. W., de Vries, M., & Intema, H. T. 2018, A&A, 618, A152
Lacy, M., Baum, S. A., Chandler, C., et al. 2020, PASP, 132, 35001
Liang, H., Hunstead, R. W., Birkinshaw, M., & Andreani, P. 2000, ApJ, 544, 686
Locatelli, N., Rajpurohit, K., Vazza, F., et al. 2020, MNRAS, 496, L48
Lovisari, L., Forman, W. R., Jones, C., et al. 2017, ApJ, 846, 51
Lukic, V., Brüggen, M., Banfield, J., et al. 2018, MNRAS, 476, 246
Lukic, V., Brüggen, M., Mingo, B., et al. 2019, MNRAS, 487, 1729
Macario, G., Venturi, T., Brunetti, G., et al. 2010, A&A, 517, A43
Macario, G., Venturi, T., Intema, H. T., et al. 2013, A&A, 551, A141
Mandal, S., Intema, H. T., Shimwell, T. W., et al. 2019, A&A, 622, A22
Mandal, S., Intema, H. T., van Weeren, R. J., et al. 2020, A&A, 634, A4
Markevitch, M. & Vikhlinin, A. 2007, Phys. Rep., 443, 1
Merloni, A., Predehl, P., Becker, W., et al. 2012, arXiv e-prints [arXiv:1209.3114]
Moffet, A. & Birkinshaw, M. 1989, AJ, 98, 1148
Mohr, J. J., Fabricant, D. G., & Geller, M. J. 1993, ApJ, 413, 492
Mostert, R. I., Duncan, K. J., Röttgering, H. J., et al. 2021, A&A, 645, A89
Murgia, M., Govoni, F., Markevitch, M., et al. 2009, A&A, 499, 679
Nurgaliev, D., McDonald, M., Benson, B., et al. 2013, ApJ, 779, 112
Nuza, S., Gelszinnis, J., Hoeft, M., & Yepes, G. 2017, MNRAS, 470, 240
Nuza, S., Hoeft, M., van Weeren, R. J., Gottlöber, S., & Yepes, G. 2012, MNRAS, 420, 2006
Offringa, A. R., McKinley, B., Hurley-Walker, N., et al. 2014, MNRAS, 444, 606
Offringa, A. R. & Smirnov, O. M. 2017, MNRAS, 471, 301
Orrù, E., Murgia, M., Feretti, L., et al. 2007, A&A, 467, 943
Osinga, E., van Weeren, R. J., Boxelaar, J. M., et al. 2021, A&A, 648, A11
Owen, F. N. & Ledlow, M. J. 1997, ApJS, 108, 41
Owen, F. N., Morrison, G. E., & Voges, W. 1999, in Diffuse Thermal and Relativistic Plasma in Galaxy Clusters, ed. H. Boehringer, L. Feretti, & P. Schuecker, 9
Parekh, V., van der Heyden, K., Ferrari, C., Angus, G., & Holwerda, B. 2015, A&A, 575, A127
Pasini, T., Brüggen, M., Hoang, D. N., et al. 2021, arXiv e-prints, arXiv:2106.14524
Paul, S., Gupta, P., Salunkhe, S., et al. 2021, MNRAS, 506, 5389
Paul, S., Salunkhe, S., Sonkamble, S., et al. 2020, A&A, 633, A59
Pedregosa, F., Varoquaux, G., Gramfort, A., et al. 2012, arXiv e-prints, arXiv:1201.0490
Perley, R. A., Chandler, C., Butler, B., & Wrobel, J. 2011, ApJ, 739, L1
Pillepich, A., Porciani, C., & Reiprich, T. H. 2012, MNRAS, 422, 44
Planck Collaboration XXII. 2016, A&A, 594, A22
Planck Collaboration XXVII. 2016, A&A, 594, A27
Poole, G., Fardal, M., Babul, A., et al. 2006, MNRAS, 373, 881
Predehl, P., Andritschke, R., Arefiev, V., et al. 2021, A&A, 647, A1
Rasia, E., Meneghetti, M., & Ettori, S. 2013, Astron. Rev., 8, 40
Roberts, I. D., van Weeren, R. J., McGee, S. L., et al. 2021a, A&A, 650, A111
Roberts, I. D., van Weeren, R. J., McGee, S. L., et al. 2021b, A&A, 652, A153
Roberts, I. D., van Weeren, R. J., Timmerman, R., et al. 2022, A&A, 658, A44
Robitaille, T. P. & Bressert, E. 2012, APLpy: Astronomical Plotting Library in Python, Astrophysics Source Code Library
Roger, R., Costain, C., & Bridle, A. 1973, AJ, 78, 1030
Rossetti, M., Gastaldello, F., Eckert, D., et al. 2017, MNRAS, 468, 1917
Rudnick, L. & Lemmerman, J. 2009, ApJ, 697, 1341
Sadeghi, M., Javaherian, M., & Miraghaei, H. 2021, AJ, 161, 94
Santos, J., Rosati, P., Tozzi, P., et al. 2008, A&A, 483, 35
Savini, F., Bonafede, A., Brüggen, M., et al. 2019, A&A, 622, A24
Savini, F., Bonafede, A., Brüggen, M., et al. 2018a, MNRAS, 478, 2234
Savini, F., Bonafede, A., Brüggen, M., et al. 2018b, MNRAS, 474, 5023
Schellenberger, G., David, L. P., O'Sullivan, E., Vrtilek, J. M., & Haines, C. P. 2019, ApJ, 882, 59
Sehgal, N., Hughes, J. P., Wittman, D., et al. 2008, ApJ, 673, 163
Sen, P. K. 1968, J. Am. Stat. Assoc., 63, 1379
Shimwell, T. W., Hardcastle, M. J., Tasse, C., et al. 2022, A&A, 659, A1
Shimwell, T. W., Luckin, J., Brüggen, M., et al. 2016, MNRAS, 459, 277
Shimwell, T. W., Röttgering, H. J., Best, P. N., et al. 2017, A&A, 598, A104
Shimwell, T. W., Tasse, C., Hardcastle, M. J., et al. 2019, A&A, 622, A1
Smirnov, O. M. & Tasse, C. 2015, MNRAS, 449, 2668
Sommer, M. W., Basu, K., Intema, H. T., et al. 2017, MNRAS, 466, 996
Streblyanska, A., Aguado-Barahona, A., Ferragamo, A., et al. 2019, A&A, 628, A13
Streblyanska, A., Barrena, R., Rubiño-Martín, J., et al. 2018, A&A, 617, A71

Sunyaev, R. & Zel'dovich, Y. 1972, CoASP, 4, 173
Swarup, G., Ananthakrishnan, S., Kapahi, V., et al. 1991, Curr. Sci., 60, 95
Tarrío, P., Melin, J.-B., & Arnaud, M. 2019, A&A, 626, A7
Tasse, C. 2014a, arXiv e-prints [arXiv:1410.8706]
Tasse, C. 2014b, A&A, 566, A127
Tasse, C., Hugo, B., Mirmont, M., et al. 2018, A&A, 611, A87
Tasse, C., Shimwell, T. W., Hardcastle, M. J., et al. 2021, A&A, 648, A1
Terni de Gregory, B., Feretti, L., Giovannini, G., et al. 2017, A&A, 608, A58
Thierbach, M., Klein, U., & Wielebinski, R. 2003, A&A, 397, 53
Thompson, A., Clark, B., Wade, C., & Napier, P. 1980, ApJS, 44, 151
Timmerman, R., van Weeren, R. J., Callingham, J., et al. 2022, A&A, 658, A5
Tingay, S. J., Goeke, R., Bowman, J. D., et al. 2013, PASA, 30, e007
Vacca, V., Murgia, M., Govoni, F., et al. 2010, A&A, 514, A71
van Haarlem, M., Wise, M. W., Gunst, A., et al. 2013, A&A, 556, A2
van Weeren, R. J., Bonafede, A., Ebeling, H., et al. 2012, MNRAS, 425, L36
van Weeren, R. J., Brüggen, M., Röttgering, H. J., et al. 2011, A&A, 533, A35
van Weeren, R. J., de Gasperin, F., Akamatsu, H., et al. 2019, Space Sci. Rev., 215, 16
van Weeren, R. J., Röttgering, H. J., Brüggen, M., & Cohen, A. 2009, A&A, 508, 75
van Weeren, R. J., Shimwell, T. W., Botteon, A., et al. 2021, A&A, 651, A115
van Weeren, R. J., Williams, W. L., Hardcastle, M. J., et al. 2016, ApJS, 223, 2
Vavilova, I., Dobrycheva, D., Vasylenko, M. Y., et al. 2021, A&A, 648, A122
Venturi, T., Giacintucci, S., Brunetti, G., et al. 2007, A&A, 463, 937
Venturi, T., Giacintucci, S., Dallacasa, D., et al. 2011, MNRAS, 414, L65
Venturi, T., Giacintucci, S., Dallacasa, D., et al. 2008, A&A, 484, 327
Venturi, T., Giacintucci, S., Dallacasa, D., et al. 2013, A&A, 551, A24
Virtanen, P., Gommers, R., Oliphant, T. E., et al. 2020, Nat. Methods, 17, 261
Wen, Z. & Han, J. 2013, MNRAS, 436, 275
Wilber, A. G., Brüggen, M., Bonafede, A., et al. 2019, A&A, 622, A25
Wilber, A. G., Brüggen, M., Bonafede, A., et al. 2018, MNRAS, 473, 3536
Williams, W. L., van Weeren, R. J., Röttgering, H. J., et al. 2016, MNRAS, 460, 2385
Yuan, Z. & Han, J. 2020, MNRAS, 497, 5485
Yuan, Z., Han, J., & Wen, Z. 2015, ApJ, 813, 77
Zandanel, F. & Ando, S. 2014, MNRAS, 440, 663
Zohren, H., Schrabback, T., van der Burg, R. F., et al. 2019, MNRAS, 488, 2523

[1] Leiden Observatory, Leiden University, PO Box 9513, NL-2300 RA Leiden, The Netherlands
e-mail: botteon@strw.leidenuniv.nl
[2] ASTRON, the Netherlands Institute for Radio Astronomy, Postbus 2, NL-7990 AA Dwingeloo, The Netherlands
[3] INAF - IRA, via P. Gobetti 101, I-40129 Bologna, Italy
[4] Hamburger Sternwarte, Universität Hamburg, Gojenbergsweg 112, D-21029 Hamburg, Germany
[5] SRON Netherlands Institute for Space Research, Niels Bohrweg 4, NL-2333 CA Leiden, The Netherlands
[6] Dipartimento di Fisica e Astronomia, Università di Bologna, via P. Gobetti 93/2, I-40129 Bologna, Italy
[7] INAF - IASF Milano, via A. Corti 12, I-20133 Milano, Italy
[8] Dipartimento di Fisica, Università degli Studi di Milano, via Celoria 16 , I-20133 Milano, Italy
[9] Kavli Institute for the Physics and Mathematics of the Universe (WPI), The University of Tokyo, Kashiwa, Chiba 277-8583, Japan
[10] Centre for Astrophysics Research, University of Hertfordshire, College Lane, Hatfield AL10 9AB, UK
[11] INAF - Astronomical Observatory of Padova, vicolo dell'Osservatorio 5, I-35122 Padova, Italy
[12] Thüringer Landessternwarte, Sternwarte 5, D-07778 Tautenburg, Germany

Appendix A: Tables

In this appendix we collect the tables listing: the main properties of the targets in the full PSZ2/LoTSS-DR2 sample (Table A.1), the X-ray morphological parameters for the clusters observed with *Chandra*/*XMM-Newton* (Table A.2), and the quantities derived for the radio halos (Table A.3) and radio relics (Table A.4) observed. All tables are available in FITS format on the project website `https://lofar-surveys.org/planck_dr2.html`.

Table A.1. Full sample of PSZ2 clusters in LoTSS-DR2.

Name	RA [deg]	Dec [deg]	z	M_{500} [$\times 10^{14}$ $M_\odot$]	$M_{500\mathrm{err}}$ [$\times 10^{14}$ $M_\odot$]	r_{500} [kpc]	$r_{500\mathrm{err}}$ [kpc]	IQ	rms [mJy beam^{-1}]	Classification	X-ray	Comment
PSZ2 G023.17+86.71	196.4731	26.5262	0.306	5.03	0.56	1093	41	1	0.093	RH	C/X	New RH
PSZ2 G031.93+78.71	205.4709	26.3684	0.072	2.72	0.24	966	28	2	0.099	RH, U	C/X	U emission on the SE, outside R500
PSZ2 G033.81+77.18	207.2221	26.5946	0.062	4.47	0.14	1144	12	3	0.102	N/A	C/X	—
PSZ2 G040.58+77.12	207.3622	28.0946	0.075	2.63	0.22	955	26	2	0.112	RH	C/X	New RH
PSZ2 G045.13+67.78	217.9958	29.5567	0.219	4.83	0.45	1113	35	1	0.105	NDE	—	—
PSZ2 G045.87+57.70	229.5874	29.4696	0.611	7.03	0.68	1085	35	1	0.110	RH	X	—
PSZ2 G046.88+56.48	231.0469	29.9129	0.115	5.31	0.23	1191	17	1	0.124	RH	C/X	—
PSZ2 G048.10+57.16	230.3161	30.6278	0.078	3.59	0.21	1058	21	1	0.101	RH, RR	C/X	—
PSZ2 G048.75+53.18	234.9669	30.6960	0.098	2.53	0.31	935	39	1	0.124	NDE	C	—
PSZ2 G049.18+65.05	221.1194	31.2334	0.234	4.73	0.49	1099	38	1	0.096	NDE	C	—
PSZ2 G049.32+44.37	245.1404	29.8941	0.097	3.67	0.26	1059	25	2	0.116	RH	C/X	New RH
PSZ2 G050.46+67.54	218.1680	31.5879	0.131	2.92	0.34	971	38	1	0.098	NDE	C	—
PSZ2 G052.08+46.13	243.4439	32.0814						1	0.093	NDE	—	—
PSZ2 G053.53+59.52	227.5546	33.4915	0.113	5.85	0.23	1231	16	1	0.093	RH, U	C/X	U emissions in the outskirts
PSZ2 G053.80+36.49	254.9008	31.7432						1	0.115	NDE	—	—
PSZ2 G054.85+54.30	233.8283	34.3446	0.235	4.39	0.46	1072	38	2	0.099	NDE	—	—
PSZ2 G054.99+53.41	234.9018	34.4313	0.229	5.73	0.38	1174	26	3	0.122	N/A	C/X	—
PSZ2 G055.59+31.85	260.6150	32.1354	0.224	7.78	0.31	1302	17	1	0.106	RH	C/X	—
PSZ2 G055.80+32.90	259.4624	32.5608	0.105	2.58	0.31	939	37	1	0.124	NDE	—	—
PSZ2 G056.14+28.06	265.0748	31.6030	0.426	5.53	0.57	1077	37	1	0.133	NDE	—	—
PSZ2 G056.38+23.36	270.3845	30.3962						2	0.226	NDE	—	—
PSZ2 G056.62+88.42	194.4923	27.7528	0.045	3.30	0.07	1039	7	-1	-1.000	—	—	Toward the direction of the Coma cluster
PSZ2 G056.77+36.32	255.6663	34.0511	0.095	4.38	0.20	1124	17	1	0.123	RH	C/X	New RH
PSZ2 G057.61+34.93	257.4672	34.4613	0.080	3.73	0.19	1071	18	2	0.140	RR, U	C/X	U emission in the center
PSZ2 G057.73+51.58	237.1413	36.1034	0.238	5.59	0.51	1160	36	1	0.113	NDE	—	—
PSZ2 G057.78+52.32	236.2149	36.1219	0.065	2.38	0.22	926	28	1	0.124	NDE	C/X	—
PSZ2 G057.80+88.00	194.9118	27.9537	0.023	7.17	0.09	1356	6	-1	-1.000	—	—	Coma cluster
PSZ2 G057.92+27.64	266.0678	32.9986	0.076	2.68	0.21	961	25	2	0.118	NDE	C/X	—
PSZ2 G058.29+18.55	276.3360	30.4320	0.065	3.88	0.17	1091	16	3	0.555	N/A	C/X	—
PSZ2 G058.31+41.96	249.0508	36.0554						1	0.095	NDE	—	—
PSZ2 G059.18+32.91	260.2029	35.3248	0.383	5.21	0.56	1074	39	1	0.145	NDE	—	—
PSZ2 G059.29+44.49	245.9901	36.9729	0.343	5.76	0.69	1128	45	1	0.123	NDE	—	—
PSZ2 G059.47+33.06	260.0786	35.6002	0.387	6.09	0.58	1129	36	2	0.170	U	C/X	—
PSZ2 G059.52+16.23	279.3393	30.6642	0.284	4.37	0.55	1052	45	3	2.503	N/A	—	Redshift updated from Streblyanska et al. (2019)
PSZ2 G059.76+14.59	281.1949	30.2468	0.303	4.80	0.51	1077	38	3	0.457	N/A	—	Redshift updated from Streblyanska et al. (2019)
PSZ2 G060.10+15.59	280.2784	30.9322	0.190	4.67	0.47	1112	37	-1	-1.000	—	—	—
PSZ2 G060.16+64.50	221.0737	35.9376	0.361	5.00	0.63	1068	45	1	0.088	NDE	—	—
PSZ2 G060.55+27.00	267.5745	35.0761	0.171	3.48	0.41	1015	40	2	0.147	NDE	C/X	—
PSZ2 G061.75+88.11	194.7270	28.0231	0.044	3.40	0.63	1051	66	-1	-1.000	—	—	Toward the direction of the Coma cluster
PSZ2 G062.94+43.69	247.1565	39.5602	0.030	2.87	0.12	997	14	3	0.123	N/A	C/X	—
PSZ2 G063.38+53.44	234.5073	39.4147	0.422	6.24	0.60	1123	36	1	0.111	cRH	—	New cRH
PSZ2 G065.28+44.53	246.0751	41.2470	0.182	3.90	0.48	1050	44	1	0.099	NDE	C	—
PSZ2 G065.45+78.10	204.8180	33.0102	0.273	4.07	0.53	1031	46	1	0.111	NDE	—	—
PSZ2 G065.79+41.80	249.7168	41.5990	0.336	5.22	0.59	1094	42	1	0.094	NDE	—	—
PSZ2 G065.89+31.59	263.2231	40.6419	0.133	2.74	0.36	949	42	1	0.119	NDE	—	—
PSZ2 G066.26+20.82	276.8511	38.2587	0.278	4.13	0.50	1034	42	2	0.194	NDE	—	—
PSZ2 G066.34+26.14	270.3078	39.8546	0.622	6.10	0.67	1031	38	2	0.110	cRH	—	New cRH. Redshift updated from Aguado-Barahona et al. (2019)
PSZ2 G066.41+27.03	269.2019	40.1327	0.576	7.70	0.53	1134	26	1	0.118	RH	C/X	New RH
PSZ2 G066.68+68.44	215.4320	37.2821	0.163	3.79	0.34	1047	32	1	0.083	NDE	C/X	—
PSZ2 G066.85+22.48	275.0416	39.2985	0.190	3.14	0.41	974	43	3	0.354	N/A	—	Redshift updated from Aguado-Barahona et al. (2019)
PSZ2 G067.17+67.46	216.5032	37.8160	0.171	7.24	0.26	1295	16	2	0.192	U	C/X	—
PSZ2 G067.52+34.75	259.3134	42.4618	0.175	4.54	0.34	1107	28	2	0.112	NDE	C/X	—
PSZ2 G068.36+81.81	200.6946	31.6565	0.308	6.60	0.43	1195	26	2	0.163	NDE	X	—
PSZ2 G069.39+68.05	215.4044	38.3613	0.762	5.69	0.77	952	43	2	0.183	cRH, cRR	—	New cRH and cRR. Redshift updated from Buddendiek et al. (2015)
PSZ2 G070.89+49.26	239.1791	44.6533	0.610	6.46	0.69	1055	38	1	0.087	NDE	X	—
PSZ2 G071.21+28.86	268.0130	44.6695	0.366	6.75	0.45	1178	26	1	0.101	RH, RR	X	Double RR
PSZ2 G071.39+59.54	225.3359	42.3464	0.292	5.87	0.42	1157	27	2	0.084	RH*	C/X	New RH*
PSZ2 G071.63+29.78	266.8257	45.1899	0.157	4.13	0.29	1080	25	1	0.101	NDE	C/X	Possible revived fossil plasma in the S
PSZ2 G072.62+41.46	250.0941	46.7103	0.228	11.69	0.26	1490	11	3	0.111	N/A	C/X	—
PSZ2 G073.31+67.52	215.1737	39.9245	0.609	6.74	0.59	1071	31	3	0.475	N/A	C/X	—
PSZ2 G073.97-27.82	328.4233	17.6986	0.233	9.80	0.28	1402	13	2	0.216	NDE	C/X	—
PSZ2 G074.37+71.11	210.9114	38.4697	0.485	5.75	0.58	1067	36	3	0.169	N/A	C	—
PSZ2 G075.08+19.83	281.6991	45.7759	0.200	3.45	0.38	1002	37	-1	-1.000	—	—	Redshift updated from Streblyanska et al. (2019)
PSZ2 G076.55+60.29	223.0302	44.4554	0.287	4.13	0.48	1031	40	1	0.067	RH*	C	New RH*. Redshift updated from Streblyanska et al. (2018)
PSZ2 G077.90-26.63	330.2281	20.9701	0.147	5.06	0.26	1160	20	2	0.216	RH*	C/X	New RH*
PSZ2 G080.16+57.65	225.2369	47.2874	0.088	2.51	0.21	937	26	1	0.127	RR	C/X	—
PSZ2 G080.41-33.24	336.5396	17.3767	0.107	3.77	0.27	1066	26	1	0.139	NDE	C/X	Revived fossil plasma
PSZ2 G080.55-24.82	330.8550	23.9105	0.266	4.28	0.53	1051	43	1	0.135	NDE	—	—
PSZ2 G080.64+64.31	216.8313	44.1308	0.502	5.23	0.59	1026	39	1	0.133	NDE	C	—
PSZ2 G080.70+48.31	238.2988	51.1483	0.235	3.20	0.41	965	41	1	0.068	cRH	—	New cRH
PSZ2 G081.02+50.57	234.8082	50.6137	0.501	4.69	0.54	991	38	1	0.061	RH	X	New RH
PSZ2 G081.72+70.15	210.0995	41.0129	0.250	4.16	0.44	1047	37	1	0.097	U	C	Two uncertain sources located to the W with respect to the bulk of the X-ray emission
PSZ2 G083.14+66.57	213.4445	43.6523	0.089	2.07	0.26	878	36	2	0.077	NDE	—	—
PSZ2 G083.29-31.03	337.1296	20.6221	0.412	8.27	0.44	1239	22	1	0.118	RH	C/X	New RH
PSZ2 G083.86+85.09	196.4623	30.8931	0.183	4.66	0.33	1114	27	1	0.079	NDE	C/X	—
PSZ2 G084.10+58.72	222.3158	48.5589	0.731	5.40	0.62	947	36	1	0.073	RH	C/X	—
PSZ2 G084.13-35.41	340.4853	17.5233	0.314	5.50	0.58	1122	40	2	0.127	RH, U	X	New RH. U emission to the S of the RH
PSZ2 G084.69+42.28	246.7659	55.4802	0.130	2.70	0.26	946	31	1	0.068	NDE	X	—
PSZ2 G085.23+39.42	251.6292	56.4674	0.257	3.88	0.39	1021	35	1	0.083	cRH	—	New cRH
PSZ2 G086.28+74.76	204.4773	38.8708	0.699	5.61	0.71	972	41	3	0.091	N/A	—	Redshift updated from Streblyanska et al. (2018)
PSZ2 G086.43-24.95	335.5578	27.1430	0.231	3.81	0.50	1024	46	1	0.127	NDE	—	—
PSZ2 G086.54-26.67	336.7802	25.8145	0.165	3.45	0.39	1015	39	1	0.120	NDE	C	—
PSZ2 G086.58+73.11	205.8750	40.1328	0.222	3.83	0.50	1029	45	1	0.073	cRR, U	—	New cRR. U emission in the center
PSZ2 G086.93+53.18	228.4787	52.7984	0.675	5.45	0.51	971	30	1	0.101	RH	C/X	—
PSZ2 G087.39-34.58	342.3068	19.7139	0.760	6.06	0.63	973	34	2	0.184	NDE	—	Redshift updated from Streblyanska et al. (2018)
PSZ2 G087.39+50.92	231.5690	54.1431	0.748	5.16	0.57	927	34	3	0.098	N/A	X	—
PSZ2 G087.44-21.56	334.0988	30.4251	0.258	4.15	0.51	1043	43	1	0.120	NDE	—	—
PSZ2 G088.53+41.18	247.3887	58.5338	0.133	2.56	0.34	929	42	1	0.076	NDE	—	Complex radio emission associated to the brightest optical galaxy

Table A.1. continued.

Name	RA [deg]	Dec [deg]	z	M_{500} [$\times 10^{14}$ M$_\odot$]	$M_{500\mathrm{err}}$ [$\times 10^{14}$ M$_\odot$]	r_{500} [kpc]	$r_{500\mathrm{err}}$ [kpc]	IQ	rms [mJy beam^{-1}]	Classification	X-ray	Comment
PSZ2 G088.98+55.07	224.7806	52.8020	0.702	4.92	0.62	929	39	3	0.105	N/A	C/X	—
PSZ2 G089.39+69.36	208.4259	43.4835	0.680	5.75	0.72	987	41	1	0.067	cRH	—	—
PSZ2 G089.52+62.34	215.5299	48.4769	0.070	1.83	0.19	847	30	2	0.078	RR	C	Two RR located in the N
PSZ2 G091.27-38.62	347.3346	17.8953	0.105	3.14	0.39	1003	42	2	0.146	NDE	—	Redshift updated from Barrena et al. (2018)
PSZ2 G091.79-27.00	341.3603	28.1444	0.362	6.31	0.48	1154	29	1	0.104	RR	X	New RR
PSZ2 G092.11-33.73	345.4059	22.4833						2	0.161	NDE	—	—
PSZ2 G092.46-35.22	346.4589	21.3244						1	0.141	NDE	—	—
PSZ2 G092.69+59.92	216.6347	51.2521	0.462	4.79	0.60	1013	43	1	0.078	NDE	C/X	Redshift updated from Aguado-Barahona et al. (2019)
PSZ2 G092.71+73.46	203.8014	41.0004	0.228	8.13	0.27	1320	14	3	0.075	N/A	C/X	—
PSZ2 G093.04-32.38	345.4276	24.0403	0.512	6.34	0.72	1090	42	2	0.200	NDE	—	Redshift updated from Barrena et al. (2018)
PSZ2 G093.71-30.90	345.1839	25.6114						3	0.350	N/A	—	—
PSZ2 G093.94-38.82	349.3656	18.7010	0.042	2.22	0.17	912	23	1	0.192	U	C/X	—
PSZ2 G094.44+36.13	255.2898	64.2391	0.453	4.09	0.43	964	34	1	0.078	NDE	C/X	—
PSZ2 G094.56+51.03	227.0614	57.8918	0.539	5.87	0.44	1051	26	3	0.086	N/A	X	—
PSZ2 G094.61-41.24	350.9896	16.7655	0.042	1.76	0.23	845	37	2	0.128	U	C/X	—
PSZ2 G095.00-37.14	349.3564	20.5736						1	0.144	NDE	—	—
PSZ2 G095.22+67.41	207.8526	46.3557	0.062	1.50	0.21	795	38	1	0.084	U	X	—
PSZ2 G095.29+44.13	238.1346	62.0545	0.331	4.03	0.35	1006	29	2	0.103	cRH*	—	New cRH*
PSZ2 G096.14+56.24	218.8388	55.1414	0.140	2.77	0.25	951	28	2	0.086	NDE	—	—
PSZ2 G096.43-20.89	342.0362	35.5560	0.350	5.39	0.51	1100	34	2	0.122	cRR	—	New cRR. Redshift updated from Boada et al. (2019)
PSZ2 G096.83+52.49	223.2488	58.0366	0.318	4.92	0.37	1080	27	1	0.073	RH	C	—
PSZ2 G097.15+39.20	246.9034	65.3963	0.206	2.94	0.32	948	34	1	0.088	NDE	—	—
PSZ2 G097.52+51.70	223.8162	58.8752	0.700	5.18	0.51	946	31	2	0.105	U	X	—
PSZ2 G097.72+38.12	248.9776	66.2023	0.171	6.59	0.16	1255	10	1	0.076	RH	C/X	—
PSZ2 G097.78+46.95	231.0525	62.0227	0.338	3.43	0.39	950	36	2	0.104	NDE	—	—
PSZ2 G098.30-41.15	353.5972	18.0003	0.436	7.05	0.61	1164	34	1	0.100	cRH	—	New cRH
PSZ2 G098.38+77.22	199.6059	38.5853	0.780	6.62	0.71	994	36	1	0.102	NDE	—	Redshift updated from Boada et al. (2019)
PSZ2 G098.39+57.68	215.5698	54.9011						1	0.091	NDE	—	—
PSZ2 G098.44+56.59	216.7791	55.7497	0.132	2.83	0.27	960	30	1	0.090	NDE	—	—
PSZ2 G098.62+51.76	222.8271	59.3306	0.298	3.35	0.48	958	47	2	0.075	NDE	—	Redshift updated from Streblyanska et al. (2018)
PSZ2 G098.75-28.63	348.4410	29.6117						2	0.113	NDE	—	—
PSZ2 G099.24+42.54	238.0378	65.3405	0.223	2.80	0.39	927	43	1	0.104	U	—	U emissions in the center and outskirts
PSZ2 G099.48+37.72	248.6714	67.6423	0.167	2.51	0.28	911	34	1	0.104	U	—	—
PSZ2 G099.48+55.60	217.1485	56.8766	0.105	2.81	0.21	967	25	1	0.098	RR	C/X	New RR. Double RR
PSZ2 G099.55+34.23	257.6109	68.7321	0.310	3.61	0.38	977	34	1	0.112	cRH*, U	—	New cRH*. U emission in the W. Redshift updated from Aguado-Barahona et al. (2019)
PSZ2 G099.86+58.45	213.6782	54.7836	0.630	6.85	0.49	1067	25	2	0.075	RH	C/X	—
PSZ2 G100.14+41.67	239.0257	66.3545	0.234	4.04	0.28	1044	24	3	0.315	N/A	C	—
PSZ2 G100.22-29.64	350.2543	29.2136	0.485	7.64	0.59	1173	30	2	0.135	NDE	—	—
PSZ2 G100.22+33.81	258.4193	69.3734	0.598	4.61	0.47	947	33	2	0.169	NDE	—	Redshift updated from Streblyanska et al. (2019)
PSZ2 G100.45-38.42	354.1311	21.1519	0.057	1.84	0.27	853	42	1	0.143	NDE	C/X	Revived fossil plasma
PSZ2 G100.96-24.07	348.3483	34.5796	0.424	5.70	0.73	1089	47	2	0.119	cRH	—	—
PSZ2 G101.52-29.98	351.5963	29.3258	0.227	4.88	0.52	1114	39	1	0.114	NDE	—	—
PSZ2 G102.90-31.04	353.3020	28.7678	0.592	6.73	0.72	1078	39	2	0.111	NDE	—	—
PSZ2 G103.40-32.99	354.5043	27.0818	0.031	1.51	0.13	805	23	3	0.164	N/A	X	—
PSZ2 G104.15-38.85	357.2018	21.7235						1	0.095	NDE	—	—
PSZ2 G105.55+77.21	197.7544	39.2463	0.072	2.20	0.22	900	30	1	0.140	U	X	—
PSZ2 G105.76+54.73	212.5897	59.6801	0.316	4.41	0.45	1042	36	1	0.149	NDE	—	—
PSZ2 G105.82-38.36	358.3931	22.5789						1	0.098	NDE	—	—
PSZ2 G106.41+50.82	216.3149	63.1860	0.139	2.89	0.25	964	27	1	0.073	U	C/X	—
PSZ2 G106.61+66.71	202.6355	49.1529	0.331	4.67	0.56	1056	42	1	0.055	RH	C	—
PSZ2 G107.10+65.32	203.1777	50.5183	0.280	8.22	0.28	1300	15	1	0.075	RH, RR	C/X	Double RH. Radio bridge. RR in A1758S. Revived fossil plasma
PSZ2 G107.11-39.50	359.7704	21.7518	0.533	6.93	0.67	1114	36	1	0.102	U	—	—
PSZ2 G107.39-31.48	357.6390	29.5399	0.150	3.45	0.45	1019	45	1	0.104	NDE	—	—
PSZ2 G107.67-39.78	0.3019	21.5932	0.415	5.73	0.75	1095	48	2	0.101	U	—	—
PSZ2 G108.24+58.11	207.2301	57.3469	0.322	3.85	0.53	994	46	1	0.183	U	—	—
PSZ2 G108.27+48.66	216.7773	65.6528	0.674	4.93	0.49	940	32	1	0.134	cRH	—	New cRH
PSZ2 G109.14-28.02	358.2865	33.2800	0.457	6.92	0.62	1147	34	3	0.096	N/A	—	—
PSZ2 G109.22-44.01	2.5556	17.7559	0.173	3.26	0.48	993	49	2	0.190	cRR	—	New cRR
PSZ2 G109.97+52.84	209.9356	62.5279	0.326	4.81	0.38	1069	28	1	0.067	RH	C	New RH
PSZ2 G111.75+70.37	198.2642	46.2812	0.183	4.34	0.33	1088	27	1	0.076	RH, RR	C/X	RR in the NE
PSZ2 G112.07-39.86	3.8730	22.2454						2	0.135	NDE	—	—
PSZ2 G112.35-32.86	2.6884	29.1673	0.348	5.50	0.68	1108	46	2	0.166	NDE	X	—
PSZ2 G112.48+56.99	203.9932	59.2210	0.070	2.99	0.15	998	17	1	0.058	RH	C	New RH
PSZ2 G112.54+59.53	202.4759	56.8123	0.830	5.76	0.66	930	36	1	0.071	NDE	—	Redshift updated from Zohren et al. (2019)
PSZ2 G113.27+48.39	209.7444	67.4431						1	0.072	NDE	—	—
PSZ2 G113.29-29.69	2.9363	32.4325	0.107	3.71	0.27	1060	25	2	0.114	U	C/X	—
PSZ2 G113.91-37.01	4.9004	25.2965	0.371	7.58	0.55	1223	30	1	0.122	RH, RR	C/X	New RH and RR. Double RR
PSZ2 G114.14+58.96	201.3065	57.5834	0.116	2.17	0.30	884	41	2	0.069	NDE	—	Possible revived fossil plasma
PSZ2 G114.31+64.89	198.7658	51.8329	0.284	6.76	0.37	1216	22	1	0.071	RH	C/X	—
PSZ2 G114.39-20.98	2.2522	41.1782	0.154	3.81	0.35	1053	32	1	0.187	NDE	—	—
PSZ2 G114.79-33.71	5.1456	28.6657	0.094	3.82	0.22	1075	21	2	0.133	NDE	C/X	—
PSZ2 G114.83+57.25	201.4457	59.3305	0.170	3.27	0.30	995	31	1	0.076	NDE	—	—
PSZ2 G114.90-34.35	5.3526	28.0504	0.095	2.47	0.32	929	41	2	0.140	U	—	—
PSZ2 G114.99+70.36	196.7286	46.5257	0.226	5.70	0.35	1174	24	2	0.086	U	C	Complex radio emission
PSZ2 G115.58-44.56	7.3620	17.9947	0.170	4.32	0.40	1091	34	1	0.100	NDE	—	—
PSZ2 G115.67-27.57	5.0172	34.8529	0.457	5.31	0.75	1050	50	1	0.100	cRH	—	—
PSZ2 G116.32-36.33	6.9294	26.2373	0.367	5.31	0.63	1087	43	3	0.128	N/A	C/X	—
PSZ2 G116.50-44.47	8.0345	18.1536	0.396	7.61	0.60	1213	32	1	0.111	RH*, RR	X	New RH* and RR
PSZ2 G118.34+68.79	195.3484	48.2419	0.255	3.77	0.49	1012	44	1	0.071	cRH*	—	—
PSZ2 G118.49+48.17	201.0202	68.6690	0.320	3.68	0.41	980	37	1	0.077	NDE	—	Redshift updated from Aguado-Barahona et al. (2019)
PSZ2 G118.92+52.38	198.5514	64.5643	0.220	4.39	0.29	1078	24	1	0.059	U	—	—
PSZ2 G119.92+59.12	195.7642	57.9334	0.196	3.44	0.33	1002	32	1	0.072	U	—	—
PSZ2 G120.08-44.41	10.7148	18.4071	0.267	4.65	0.64	1080	49	2	0.218	NDE	—	—
PSZ2 G121.03+57.02	194.9266	60.0741	0.344	5.69	0.43	1123	28	1	0.089	RR, U	C	New RR. U emission in the center
PSZ2 G121.13+49.64	195.8869	67.4415	0.221	3.17	0.36	967	37	1	0.091	NDE	X	—
PSZ2 G121.77+51.75	194.5723	65.3600	0.233	3.98	0.41	1038	35	1	0.056	NDE	—	—
PSZ2 G121.87-45.97	12.0892	16.8876						2	0.237	NDE	—	—
PSZ2 G122.30+54.52	193.6463	62.5963	0.318	4.53	0.45	1050	35	1	0.094	NDE	—	—

Table A.1. continued.

Name	RA [deg]	Dec [deg]	z	M_{500} [$\times 10^{14}$ M$_\odot$]	$M_{500\mathrm{err}}$ [$\times 10^{14}$ M$_\odot$]	r_{500} [kpc]	$r_{500\mathrm{err}}$ [kpc]	IQ	rms [mJy beam^{-1}]	Classification	X-ray	Comment
PSZ2 G122.47-38.41	12.4689	24.4527	0.082	2.52	0.31	939	38	2	0.115	U	—	—
PSZ2 G122.89-36.82	12.8246	26.0510	0.346	5.57	0.73	1114	49	1	0.083	NDE	—	—
PSZ2 G123.00-35.52	12.9231	27.3461	0.380	6.47	0.65	1156	39	2	0.077	RH*	X	New RH*
PSZ2 G123.66+67.25	192.4223	49.8718	0.284	4.38	0.51	1053	41	1	0.064	NDE	C	—
PSZ2 G124.20-36.48	14.0018	26.3784	0.197	7.65	0.36	1308	20	3	0.113	N/A	C/X	—
PSZ2 G125.30-27.99	15.4081	34.8346	0.223	5.02	0.55	1126	41	1	0.111	U	—	—
PSZ2 G125.71+53.86	189.2251	63.1843	0.302	6.55	0.33	1195	20	3	0.072	N/A	C/X	—
PSZ2 G126.20-33.17	16.0136	29.6172	0.358	5.45	0.74	1101	50	1	0.123	NDE	—	—
PSZ2 G126.28+65.62	190.6409	51.4447	0.820	5.54	0.66	922	37	1	0.055	U	—	Redshift updated from Burenin et al. (2018)
PSZ2 G126.57+51.61	187.4359	65.3561	0.815	6.47	0.61	973	31	1	0.066	NDE	C	Redshift updated from Burenin et al. (2018)
PSZ2 G126.61-37.63	16.0784	25.1450	0.166	3.84	0.50	1050	46	3	0.169	N/A	X	—
PSZ2 G126.72-21.03	17.6030	41.6924	0.220	4.11	0.57	1055	49	1	0.110	NDE	—	Redshift updated from Burenin et al. (2018)
PSZ2 G127.44-34.74	17.0569	27.9786	0.249	4.90	0.71	1106	54	2	0.131	NDE	—	—
PSZ2 G127.50-30.52	17.5164	32.1829	0.353	5.29	0.67	1092	46	1	0.107	NDE	X	—
PSZ2 G128.15-24.71	18.8768	37.9135	0.263	4.48	0.60	1068	48	1	0.069	NDE	—	Redshift updated from Streblyanska et al. (2019)
PSZ2 G129.99-22.42	21.3891	39.9803						1	0.081	NDE	—	—
PSZ2 G130.25-26.50	20.9524	35.9025	0.216	4.49	0.50	1088	40	2	0.102	NDE	—	—
PSZ2 G131.27-25.82	22.2049	36.4447						1	0.141	NDE	—	—
PSZ2 G132.54-42.16	20.4346	20.1398	0.194	3.99	0.51	1054	45	1	0.152	NDE	X	—
PSZ2 G133.59+50.68	176.7040	65.0891	0.529	5.16	0.57	1011	37	1	0.076	RH*	X	New RH*
PSZ2 G133.60+69.04	187.2235	47.6123	0.254	5.88	0.40	1173	27	1	0.069	RH	C	Possible revived fossil plasma
PSZ2 G133.92-42.73	21.4010	19.4054	0.636	7.24	0.96	1085	48	1	0.116	NDE	—	Redshift updated from Burenin (2017)
PSZ2 G134.26-44.28	21.3587	17.8353						1	0.152	NDE	—	—
PSZ2 G134.59+53.38	177.7969	62.3578	0.345	4.45	0.54	1034	42	2	0.080	NDE	—	—
PSZ2 G134.70+48.91	173.3085	66.3869	0.116	3.40	0.22	1027	22	2	0.107	NDE	C/X	—
PSZ2 G135.06+54.39	178.0903	61.3191	0.317	5.41	0.42	1115	29	1	0.065	NDE	—	—
PSZ2 G135.17+65.43	184.8205	50.9217	0.544	6.01	0.60	1057	35	2	0.071	RH, RR	C	—
PSZ2 G135.19+57.88	180.5387	58.0593	0.103	2.21	0.23	893	31	3	0.133	N/A	C	—
PSZ2 G136.31+54.67	176.9598	60.7656	0.477	5.98	0.51	1084	31	1	0.069	NDE	—	Redshift updated from Streblyanska et al. (2019)
PSZ2 G136.33-44.53	22.8257	17.3003						1	0.197	NDE	—	—
PSZ2 G136.64-25.03	28.2988	36.1888	0.016	1.12	0.11	732	24	2	0.125	NDE	C/X	—
PSZ2 G136.92+59.46	180.0852	56.2524	0.065	1.81	0.16	846	25	2	0.103	U	X	—
PSZ2 G137.24+53.93	175.2772	61.1942	0.470	7.00	0.48	1146	26	1	0.063	NDE	—	Redshift updated from Boada et al. (2019)
PSZ2 G137.58+53.88	174.8622	61.1503						1	0.084	NDE	—	—
PSZ2 G137.74-27.08	28.7835	33.9443	0.087	2.83	0.28	975	32	2	0.123	NDE	X	Possible revived fossil plasma
PSZ2 G138.32-39.82	25.5157	21.5330	0.280	5.98	0.56	1169	37	1	0.138	RH	C	—
PSZ2 G139.00+50.92	170.0451	63.2596	0.784	5.90	0.70	955	38	1	0.077	NDE	—	Redshift updated from Aguado-Barahona et al. (2019)
PSZ2 G139.18+56.37	175.5928	58.5227	0.322	6.87	0.38	1205	22	1	0.068	RH	C/X	—
PSZ2 G139.72-17.13	34.9806	42.8317	0.155	3.61	0.44	1033	42	1	0.153	NDE	—	Redshift updated from Streblyanska et al. (2019)
PSZ2 G141.05-32.61	30.0905	27.8208	0.554	6.92	0.77	1104	41	2	0.124	cRH	—	New cRH
PSZ2 G141.98+69.31	183.2387	46.3648	0.713	5.29	0.68	948	40	1	0.087	NDE	—	Redshift updated from Aguado-Barahona et al. (2019)
PSZ2 G143.26+65.24	179.8427	49.7742	0.363	7.65	0.43	1230	23	1	0.061	RH	C/X	—
PSZ2 G143.44+53.66	168.7489	59.4513	0.366	5.31	0.57	1088	39	2	0.067	U	—	Possible revived fossil plasma
PSZ2 G143.62+42.61	150.8432	67.1371	0.206	4.95	0.34	1127	26	1	0.087	NDE	—	—
PSZ2 G144.23-18.19	39.7214	40.1886						1	0.096	cRH	—	New cRH
PSZ2 G144.33+62.85	177.3062	51.6086	0.132	2.66	0.35	940	42	1	0.063	NDE	—	—
PSZ2 G144.84-35.16	32.4230	24.3554						1	0.092	NDE	—	—
PSZ2 G144.99-24.64	37.1891	34.0270	0.190	4.25	0.50	1077	42	2	0.097	cRR, U	—	New cRR. U emission located in the center of the images
PSZ2 G145.25+50.84	163.3572	60.8620						1	0.073	NDE	—	—
PSZ2 G145.65+59.30	173.1514	54.2102	0.347	4.73	0.61	1054	46	2	0.076	U	X	—
PSZ2 G146.13+40.97	144.7845	66.4371	0.342	4.70	0.65	1054	49	1	0.076	NDE	—	Redshift updated from Aguado-Barahona et al. (2019)
PSZ2 G146.82+40.97	144.1849	65.9752	0.259	4.49	0.27	1071	21	1	0.070	NDE	—	—
PSZ2 G147.17+42.67	147.4525	64.9221	0.460	5.65	0.72	1071	46	1	0.078	NDE	—	Redshift updated from Aguado-Barahona et al. (2019)
PSZ2 G147.88+53.24	164.3924	58.0187	0.600	6.47	0.60	1060	33	1	0.065	cRH	—	—
PSZ2 G148.36+75.23	184.6185	40.2211	0.304	4.75	0.50	1073	38	1	0.075	RH	C	New RH
PSZ2 G149.22+54.18	164.6039	56.7926	0.137	5.87	0.22	1222	15	2	0.083	RH	C	—
PSZ2 G149.75+34.68	127.7147	65.8623	0.182	8.86	0.32	1381	17	1	0.069	RH	C/X	—
PSZ2 G150.24+48.72	155.8514	59.8085	0.205	3.56	0.42	1010	40	1	0.066	NDE	—	—
PSZ2 G150.56+46.67	152.1830	60.7778	0.398	5.21	0.62	1068	42	1	0.061	cRH	—	—
PSZ2 G150.56+58.32	168.7952	53.3275	0.470	7.55	0.51	1175	26	2	0.075	RH	C/X	—
PSZ2 G151.19+48.27	154.4084	59.5510	0.289	5.08	0.47	1103	34	2	0.059	RH, RR	C/X	—
PSZ2 G151.62+54.78	163.7128	55.3610	0.486	5.37	0.72	1042	47	3	0.155	N/A	—	—
PSZ2 G152.33+81.28	187.6699	34.6290	0.333	5.36	0.55	1105	38	2	0.084	NDE	—	Possible revived fossil plasma
PSZ2 G152.40+75.00	183.3147	39.8577	0.453	5.14	0.70	1040	47	1	0.074	NDE	—	Redshift updated from Streblyanska et al. (2018)
PSZ2 G152.47+42.11	142.4647	61.6579	0.900	6.58	0.77	946	37	1	0.096	NDE	—	Redshift updated from Aguado-Barahona et al. (2019)
PSZ2 G153.29+36.56	130.6776	62.6758	0.650	6.32	1.27	1031	68	1	0.077	NDE	—	—
PSZ2 G153.56+36.82	131.1332	62.4117						1	0.068	NDE	—	—
PSZ2 G153.57+36.26	129.9422	62.5148	0.132	3.37	0.39	1018	39	1	0.077	NDE	—	—
PSZ2 G153.68+36.96	131.3866	62.2867						1	0.070	NDE	—	—
PSZ2 G153.80+33.79	124.5597	62.6820						1	0.070	NDE	—	—
PSZ2 G154.13+40.19	137.8076	61.1324	0.290	5.47	0.45	1131	31	1	0.087	cRH	—	New cRH
PSZ2 G155.80+70.40	178.4833	42.8600	0.333	4.42	0.56	1036	44	1	0.071	NDE	—	Possible revived fossil plasma
PSZ2 G156.26+59.64	167.1024	50.2811	0.588	6.77	0.60	1081	32	2	0.096	cRH	—	—
PSZ2 G157.63+78.02	184.3872	36.7167	0.377	5.56	0.57	1100	38	2	0.072	U	—	—
PSZ2 G159.86+42.57	139.8791	56.3460	0.270	4.61	0.57	1076	44	1	0.080	NDE	—	—
PSZ2 G160.83+81.66	186.7250	33.5703	0.888	5.70	0.66	906	35	1	0.087	RH	C/X	—
PSZ2 G160.94+44.85	143.3681	54.9523						1	0.082	NDE	—	—
PSZ2 G163.61+34.30	124.7099	54.5333	0.596	5.76	0.74	1021	44	2	0.079	cRH*	—	New cRH*
PSZ2 G163.69+53.52	155.5975	50.1197	0.158	4.73	0.31	1130	24	2	0.090	U	C	—
PSZ2 G163.87+48.54	148.2005	51.8883	0.214	3.62	0.43	1013	41	1	0.059	NDE	C	—
PSZ2 G164.65+46.37	144.5898	52.0336	0.342	6.01	0.55	1144	35	1	0.070	RH	C	New RH
PSZ2 G165.06+54.13	155.9404	49.1327	0.144	4.94	0.28	1152	22	1	0.078	RH	C	—
PSZ2 G165.46+66.15	170.9186	43.0135	0.196	3.70	0.42	1027	39	1	0.108	RR	C	Double RR
PSZ2 G165.68+44.01	140.5859	51.8876	0.210	3.76	0.50	1027	46	1	0.072	NDE	—	—
PSZ2 G165.76+31.15	119.5415	52.5986	0.259	4.43	0.66	1066	54	2	0.131	NDE	—	—
PSZ2 G165.95+41.01	135.7227	52.2021	0.062	1.79	0.26	843	40	1	0.079	NDE	C/X	—
PSZ2 G166.09+43.38	139.4836	51.7221	0.217	6.85	0.32	1251	20	1	0.074	RH	C/X	—
PSZ2 G166.62+42.13	137.3948	51.5489	0.232	5.34	0.40	1145	28	1	0.081	RH, RR	C	RH contaminated by RR emission. Multiple RR

Table A.1. continued.

Name	RA [deg]	Dec [deg]	z	M_{500} [$\times 10^{14}$ M$_\odot$]	$M_{500\mathrm{err}}$ [$\times 10^{14}$ M$_\odot$]	r_{500} [kpc]	$r_{500\mathrm{err}}$ [kpc]	IQ	rms [mJy beam^{-1}]	Classification	X-ray	Comment
PSZ2 G168.33+69.73	174.0505	40.1032	0.288	4.79	0.50	1083	37	1	0.102	U	C	Possible revived fossil plasma
PSZ2 G169.62+33.84	124.1776	49.5502	0.347	5.92	0.63	1136	40	3	0.125	N/A	—	—
PSZ2 G170.26+73.90	178.0167	37.2537	0.165	3.12	0.42	981	45	2	0.094	U	—	—
PSZ2 G170.98+39.45	132.7602	48.5104	0.538	8.08	0.68	1170	33	2	0.092	U	C	—
PSZ2 G172.63+35.15	126.3699	47.1532	0.127	3.90	0.34	1071	31	1	0.180	RH	C	New RH
PSZ2 G172.74+65.30	167.9029	40.8574	0.079	2.45	0.21	932	27	2	0.105	U	C/X	Possible revived fossil plasma
PSZ2 G175.60+35.47	127.0828	44.7549	0.145	3.08	0.40	983	43	2	0.109	U	C	—
PSZ2 G176.27+37.54	130.0378	44.3618	0.567	6.14	0.86	1056	50	2	0.091	RH	C	—
PSZ2 G177.03+32.64	123.3526	43.2651	0.511	6.07	0.76	1075	45	1	0.120	NDE	—	Redshift updated from Aguado-Barahona et al. (2019)
PSZ2 G178.00+42.32	136.6840	43.1361	0.237	3.97	0.54	1036	47	1	0.073	NDE	—	—
PSZ2 G178.94+56.00	154.9481	41.0098	0.092	2.23	0.30	899	40	1	0.074	NDE	—	—
PSZ2 G179.09+60.12	160.1864	39.9592	0.137	3.84	0.33	1061	30	1	0.093	RH	C/X	New RH
PSZ2 G180.60+76.65	179.3110	33.6110	0.214	6.30	0.34	1218	22	2	0.094	NDE	C	—
PSZ2 G180.88+31.04	121.9739	39.7755	0.365	5.99	0.70	1133	44	3	0.112	N/A	X	—
PSZ2 G181.06+48.47	144.8501	40.7576	0.240	4.23	0.49	1057	41	1	0.066	RR	C	New RR. Double RR
PSZ2 G182.59+55.83	154.2574	39.0280	0.206	5.83	0.34	1191	23	3	0.095	N/A	C/X	—
PSZ2 G183.30+34.98	127.4335	38.4548	0.392	6.56	0.64	1156	38	2	0.097	cRH, U	—	New cRH. U emisssion located in the E
PSZ2 G183.90+42.99	137.6963	38.8112	0.561	6.95	0.74	1102	39	1	0.096	RH	X	—
PSZ2 G184.24+43.69	138.6019	38.6019	0.397	5.41	0.63	1082	42	1	0.077	NDE	—	—
PSZ2 G184.68+28.91	120.2399	36.0972	0.288	5.50	0.52	1134	36	1	0.088	RH	C/X	New RH
PSZ2 G185.08+34.02	126.5397	36.8505	0.365	5.41	0.66	1095	44	1	0.111	NDE	—	—
PSZ2 G186.37+37.26	130.7485	36.3528	0.282	11.00	0.37	1431	16	1	0.107	RH	C/X	—
PSZ2 G186.61+62.94	162.6646	35.8429	0.509	5.68	0.65	1052	40	1	0.067	cRH	—	New cRH
PSZ2 G186.99+38.65	132.5385	36.0766	0.378	6.84	0.52	1178	30	2	0.092	RH, RR	C	New RH and RR
PSZ2 G187.53+21.92	113.0646	31.6261	0.171	5.17	0.39	1158	29	2	0.160	U	C/X	—
PSZ2 G187.74+20.66	111.7531	31.0220	0.193	4.29	0.50	1080	42	3	0.218	N/A	—	—
PSZ2 G189.23+20.55	112.1961	29.6730	0.398	5.46	0.74	1085	50	2	0.147	NDE	—	—
PSZ2 G189.31+59.24	157.9544	35.0406	0.126	3.24	0.31	1007	32	1	0.103	RH	C	New RH. Revived fossil plasma
PSZ2 G190.61+66.46	166.5376	33.5720	0.488	5.55	0.65	1053	41	1	0.077	RH, RR	C	New RH and RR
PSZ2 G191.57+58.88	157.4152	33.9099						1	0.107	NDE	—	—
PSZ2 G192.18+56.12	154.0911	33.6604	0.124	3.62	0.30	1045	29	1	0.089	RH	C/X	New RH
PSZ2 G192.77+33.14	127.1718	30.4022	0.050	1.66	0.20	825	34	2	0.116	cRH	—	New cRH
PSZ2 G192.90+29.63	123.3039	29.3652	0.360	5.17	0.76	1080	53	1	0.119	cRH	—	New cRH
PSZ2 G193.63+54.85	152.5729	32.8307	0.292	5.19	0.52	1110	37	2	0.134	U	X	—
PSZ2 G194.98+54.12	151.7502	32.0212	0.375	5.66	0.66	1108	43	2	0.120	U	C	—
PSZ2 G195.24+29.34	123.6579	27.3366	0.284	4.94	0.62	1095	46	2	0.113	U	—	—
PSZ2 G195.60+44.06	140.0993	30.5038	0.295	6.13	0.48	1172	31	2	0.105	NDE	C/X	—
PSZ2 G197.13+33.46	128.6143	26.9731	0.456	5.87	0.69	1086	43	1	0.109	U	—	—
PSZ2 G198.46+46.01	142.7118	28.8476	0.299	5.55	0.54	1132	37	1	0.088	cRR, U	—	New cRR
PSZ2 G199.61+53.41	151.2012	29.2311	0.371	5.54	0.59	1101	39	1	0.095	NDE	—	—
PSZ2 G199.75+46.59	143.5387	28.0764	0.553	5.91	0.76	1048	45	2	0.098	NDE	—	—
PSZ2 G200.06+77.22	178.5581	29.2431	0.361	4.62	0.61	1041	46	3	0.130	N/A	—	—
PSZ2 G202.66+66.98	166.8142	28.7965	0.483	5.28	0.70	1038	46	1	0.115	NDE	—	Redshift updated from Streblyanska et al. (2018)
PSZ2 G203.22+66.40	166.1721	28.5492	0.580	5.89	0.71	1036	42	3	0.130	N/A	—	—
PSZ2 G205.90+73.76	174.5534	27.9203	0.447	7.39	0.55	1177	29	1	0.101	RH, RR	C	New RH and RR. Double RR

Notes. Column 1: PSZ2 name; Cols. 2 and 3: coordinates; Col. 4: redshift; Cols. 5 and 6: mass and its error; Cols. 7 and 8: radius and its error; Cols. 9 and 10: image quality (IQ; see Sect. 3.3) and rms noise of the reference LOFAR image (-1 denotes the targets that were not extracted and self-calibrated); Col. 11: classification of the radio emission (see Sect. 4); Col. 12: presence of archival X-ray observations (C=*Chandra*, X=*XMM-Newton*); Col. 13: comments. Columns 1-6 are provided by the PSZ2 catalog (Planck Collaboration XXVII 2016).

Table A.2. Subsample of galaxy clusters with *Chandra*/*XMM-Newton* data available for which we computed the X-ray morphological parameters.

Name	Subcluster	c	$c_{\rm err}$	w	$w_{\rm err}$	X-ray
PSZ2 G023.17+86.71		1.23e-01	1.00e-02	2.17e-02	2.65e-03	C+X
PSZ2 G031.93+78.71		2.14e-01	1.53e-03	2.83e-02	2.39e-04	X
PSZ2 G033.81+77.18		4.26e-01	1.77e-03	8.67e-03	2.43e-03	C+X
PSZ2 G040.58+77.12		2.27e-01	6.40e-03	6.11e-03	6.80e-04	C+X
PSZ2 G045.87+57.70		2.54e-01	5.10e-03	2.18e-02	7.02e-04	X
PSZ2 G046.88+56.48		8.24e-02	4.15e-03	2.34e-02	1.75e-03	C+X
PSZ2 G048.10+57.16		8.80e-02	2.87e-03	5.91e-02	7.59e-03	C+X
PSZ2 G048.75+53.18		3.40e-01	8.41e-03	6.49e-03	1.22e-03	C
PSZ2 G049.18+65.05		2.87e-01	1.71e-02	7.97e-03	3.10e-03	C
PSZ2 G049.32+44.37		1.84e-01	6.00e-03	1.09e-02	1.10e-03	C+X
PSZ2 G050.46+67.54		3.61e-01	5.14e-03	1.86e-03	5.16e-04	C
PSZ2 G053.53+59.52		1.39e-01	2.72e-03	1.32e-02	3.49e-03	C+X
PSZ2 G054.99+53.41		1.44e-01	1.09e-02	1.65e-02	3.19e-03	C+X
PSZ2 G055.59+31.85		3.00e-01	1.49e-02	5.65e-03	3.84e-03	C+X
PSZ2 G056.77+36.32		3.03e-01	1.05e-02	3.88e-03	1.78e-03	C+X
PSZ2 G057.61+34.93		1.08e-01	4.11e-03	1.40e-02	1.02e-03	C+X
PSZ2 G057.78+52.32	E	2.26e-01	1.83e-03	6.11e-03	4.55e-04	X
PSZ2 G057.78+52.32	W	2.25e-01	5.74e-03	1.61e-02	1.44e-03	X
PSZ2 G057.92+27.64		4.52e-01	1.96e-02	5.48e-03	3.93e-03	C+X
PSZ2 G058.29+18.55	E	1.25e-01	1.53e-02	3.63e-02	2.22e-02	C+X
PSZ2 G058.29+18.55	W	4.22e-01	3.26e-03	1.34e-02	5.43e-04	X
PSZ2 G059.47+33.06		3.66e-01	3.98e-02	1.36e-02	9.59e-04	C+X
PSZ2 G060.55+27.00		4.22e-01	1.05e-02	4.26e-03	8.72e-04	C+X
PSZ2 G062.94+43.69		4.36e-01	3.40e-04	3.00e-03	1.95e-05	X
PSZ2 G065.28+44.53		2.11e-01	6.56e-03	3.44e-02	1.78e-03	C
PSZ2 G066.41+27.03		8.83e-02	8.98e-03	2.75e-02	2.28e-02	C+X
PSZ2 G066.68+68.44		3.42e-01	8.91e-03	8.70e-03	3.25e-03	C+X
PSZ2 G067.17+67.46		2.23e-01	8.98e-03	4.29e-02	1.61e-03	C+X
PSZ2 G067.52+34.75		3.89e-01	2.42e-03	4.10e-03	2.71e-04	X
PSZ2 G068.36+81.81		1.37e-01	3.05e-03	2.69e-02	8.34e-04	X
PSZ2 G070.89+49.26		1.36e-01	4.25e-03	2.06e-02	1.20e-03	X
PSZ2 G071.21+28.86		6.38e-02	4.45e-03	1.29e-02	2.08e-03	X
PSZ2 G071.39+59.54		1.53e-01	1.51e-02	1.65e-02	3.03e-03	C+X
PSZ2 G071.63+29.78		8.24e-02	3.34e-03	2.45e-02	1.38e-02	C+X
PSZ2 G072.62+41.46		1.30e-01	7.29e-03	2.68e-02	5.08e-03	C+X
PSZ2 G073.31+67.52		1.56e-01	1.42e-02	1.58e-02	2.81e-03	C+X
PSZ2 G073.97-27.82		2.77e-01	5.97e-03	1.11e-02	5.59e-04	C+X
PSZ2 G074.37+71.11		1.43e-01	2.00e-02	2.82e-02	6.10e-03	C
PSZ2 G076.55+60.29		2.38e-01	1.70e-02	2.87e-02	3.84e-03	C
PSZ2 G077.90-26.63		2.19e-01	7.61e-03	1.80e-02	1.05e-03	C+X
PSZ2 G080.16+57.65		1.30e-01	1.12e-02	3.27e-02	2.05e-03	C+X
PSZ2 G080.41-33.24		1.98e-01	1.72e-02	5.85e-02	1.31e-02	C+X
PSZ2 G080.64+64.31		4.53e-01	1.24e-02	6.22e-03	1.50e-03	C
PSZ2 G081.02+50.57		1.49e-01	5.22e-03	3.77e-02	1.37e-03	X
PSZ2 G081.72+70.15		1.21e-01	1.80e-02	1.83e-02	5.38e-03	C
PSZ2 G083.29-31.03		1.77e-01	1.27e-02	2.97e-02	1.07e-02	C+X
PSZ2 G083.86+85.09		1.89e-01	9.11e-03	3.33e-02	4.09e-03	C+X
PSZ2 G084.10+58.72		1.77e-01	2.79e-02	2.04e-02	9.05e-03	C+X
PSZ2 G084.13-35.41		9.53e-02	5.82e-03	3.79e-02	2.14e-03	X
PSZ2 G084.69+42.28		2.70e-01	4.30e-03	1.29e-02	5.93e-04	X
PSZ2 G086.54-26.67		3.04e-01	6.40e-03	5.42e-03	8.78e-04	C
PSZ2 G086.93+53.18		1.26e-01	1.86e-02	1.86e-02	3.51e-03	C+X
PSZ2 G087.39+50.92		2.13e-01	1.16e-02	2.34e-02	2.13e-03	X
PSZ2 G088.98+55.07		2.94e-01	1.20e-01	6.44e-02	1.62e-02	C+X
PSZ2 G089.52+62.34		1.13e-01	9.41e-03	3.20e-02	2.26e-03	C
PSZ2 G091.79-27.00		7.29e-02	6.16e-03	4.54e-02	2.52e-03	X
PSZ2 G092.69+59.92		1.29e-01	4.45e-02	6.63e-02	4.53e-02	C+X
PSZ2 G092.71+73.46		1.54e-01	5.69e-03	1.44e-02	2.21e-03	C+X
PSZ2 G093.94-38.82	EN	2.14e-01	2.36e-03	4.07e-02	5.69e-04	X
PSZ2 G093.94-38.82	ES	1.93e-01	2.30e-03	3.18e-02	5.75e-04	X
PSZ2 G093.94-38.82	W	3.29e-01	3.09e-03	1.68e-02	5.35e-04	X
PSZ2 G094.44+36.13		2.83e-01	2.85e-02	1.33e-02	4.92e-03	C+X
PSZ2 G094.56+51.03		1.02e-01	4.14e-03	5.69e-02	1.67e-03	X
PSZ2 G094.61-41.24		3.23e-01	1.26e-03	7.82e-03	2.16e-04	X
PSZ2 G095.22+67.41		1.25e-01	2.28e-03	2.06e-02	8.51e-04	X
PSZ2 G096.83+52.49		2.09e-01	3.63e-03	8.69e-03	8.71e-04	C
PSZ2 G097.52+51.70		2.17e-01	8.06e-03	1.92e-02	1.10e-03	X

Table A.2. continued.

Name	Subcluster	c	$c_{\rm err}$	w	$w_{\rm err}$	X-ray
PSZ2 G097.72+38.12		1.70e-01	6.56e-03	3.21e-02	7.91e-03	C+X
PSZ2 G099.48+55.60		8.41e-02	4.91e-03	2.55e-02	3.21e-03	C+X
PSZ2 G099.86+58.45		1.33e-01	1.04e-02	2.15e-02	5.58e-03	C+X
PSZ2 G100.14+41.67		2.50e-01	3.02e-03	5.67e-02	5.84e-04	C
PSZ2 G100.45-38.42		4.11e-01	1.50e-03	2.64e-03	1.35e-04	X
PSZ2 G103.40-32.99		1.08e-01	1.21e-03	5.21e-03	5.06e-04	X
PSZ2 G105.55+77.21		1.82e-01	2.31e-03	2.52e-02	6.40e-04	X
PSZ2 G106.41+50.82		3.49e-01	2.12e-02	1.90e-02	1.22e-03	C+X
PSZ2 G106.61+66.71		1.40e-01	3.20e-02	5.08e-02	7.99e-03	C
PSZ2 G107.10+65.32	N	1.07e-01	5.96e-03	8.61e-02	1.15e-03	C+X
PSZ2 G107.10+65.32	S	1.42e-01	6.93e-03	3.60e-02	2.18e-03	C+X
PSZ2 G109.97+52.84		3.34e-01	5.04e-03	8.21e-03	8.83e-04	C
PSZ2 G111.75+70.37		9.16e-02	6.56e-03	5.71e-02	3.19e-03	C+X
PSZ2 G112.35-32.86		2.63e-01	9.71e-03	1.35e-02	1.41e-03	X
PSZ2 G112.48+56.99		1.74e-01	4.69e-03	4.60e-03	9.61e-04	C
PSZ2 G113.29-29.69		1.69e-01	1.02e-02	1.33e-02	5.02e-03	C+X
PSZ2 G113.91-37.01		1.57e-01	1.65e-02	4.60e-02	2.54e-03	C+X
PSZ2 G114.31+64.89		1.66e-01	2.70e-02	1.28e-02	1.92e-03	C+X
PSZ2 G114.79-33.71		1.53e-01	9.18e-03	7.39e-03	4.54e-03	C+X
PSZ2 G114.99+70.36		1.46e-01	5.90e-03	1.72e-02	1.80e-03	C
PSZ2 G116.32-36.33	N	1.50e-01	1.70e-02	1.24e-02	4.73e-03	C+X
PSZ2 G116.32-36.33	S	2.97e-01	1.26e-02	9.13e-03	1.50e-03	X
PSZ2 G116.50-44.47		1.30e-01	6.75e-03	5.60e-02	2.37e-03	X
PSZ2 G121.03+57.02		9.77e-02	7.83e-03	1.10e-01	3.74e-03	C
PSZ2 G121.13+49.64		9.88e-02	5.27e-03	3.28e-02	1.94e-03	X
PSZ2 G123.00-35.52		1.56e-01	5.28e-03	2.39e-02	1.08e-03	X
PSZ2 G123.66+67.25		2.50e-01	3.05e-02	1.59e-02	5.27e-03	C
PSZ2 G124.20-36.48	N	3.06e-01	3.56e-03	5.41e-02	8.91e-04	C+X
PSZ2 G124.20-36.48	S	1.01e-01	1.04e-02	1.90e-02	6.16e-03	C+X
PSZ2 G125.71+53.86		1.96e-01	1.68e-02	1.04e-02	3.56e-03	C+X
PSZ2 G126.61-37.63		1.70e-01	5.69e-03	8.77e-03	1.09e-03	X
PSZ2 G127.50-30.52		1.16e-01	7.32e-03	1.39e-02	2.04e-03	X
PSZ2 G132.54-42.16		2.11e-01	8.94e-03	2.55e-03	1.58e-03	X
PSZ2 G133.59+50.68		9.27e-02	5.08e-03	1.94e-02	2.18e-03	X
PSZ2 G133.60+69.04		8.67e-02	8.92e-03	3.80e-02	3.49e-03	C
PSZ2 G134.70+48.91		2.52e-01	2.79e-02	5.34e-03	1.98e-03	C+X
PSZ2 G135.17+65.43		1.05e-01	1.87e-02	4.72e-02	7.64e-03	C
PSZ2 G135.19+57.88		1.66e-01	9.31e-03	1.33e-02	2.56e-03	C
PSZ2 G136.92+59.46		9.37e-02	2.33e-03	8.87e-02	1.22e-03	X
PSZ2 G137.74-27.08		1.46e-01	2.35e-03	4.31e-02	6.91e-04	X
PSZ2 G138.32-39.82		1.98e-01	6.58e-03	1.32e-02	1.33e-03	C
PSZ2 G139.18+56.37		8.60e-02	5.90e-03	4.70e-02	8.49e-03	C+X
PSZ2 G143.26+65.24		1.42e-01	2.62e-02	2.46e-02	1.49e-03	C+X
PSZ2 G145.65+59.30		1.44e-01	6.56e-03	1.20e-02	1.45e-03	X
PSZ2 G148.36+75.23		2.06e-01	9.02e-03	5.27e-02	2.43e-03	C
PSZ2 G149.22+54.18		1.36e-01	3.42e-03	3.72e-03	8.17e-04	C
PSZ2 G149.75+34.68		1.72e-01	3.39e-03	6.13e-02	3.66e-03	C+X
PSZ2 G150.56+58.32		1.33e-01	1.62e-02	3.16e-02	1.77e-02	C+X
PSZ2 G151.19+48.27		7.73e-02	8.77e-03	2.41e-02	1.18e-02	C+X
PSZ2 G160.83+81.66		2.78e-01	3.08e-02	1.72e-02	3.92e-03	C+X
PSZ2 G163.69+53.52		1.98e-01	5.88e-03	8.31e-03	1.41e-03	C
PSZ2 G163.87+48.54		4.61e-01	3.51e-03	1.61e-03	3.40e-04	C
PSZ2 G164.65+46.37		2.46e-01	1.00e-02	6.05e-02	2.10e-03	C
PSZ2 G165.06+54.13		1.88e-01	5.22e-03	1.77e-02	1.53e-03	C
PSZ2 G165.46+66.15		6.96e-02	5.22e-03	3.31e-02	3.13e-03	C
PSZ2 G166.09+43.38		1.84e-01	6.80e-03	1.83e-02	5.71e-03	C+X
PSZ2 G166.62+42.13		6.85e-02	5.52e-03	3.48e-02	3.03e-03	C
PSZ2 G168.33+69.73		2.64e-01	3.00e-02	1.91e-02	4.29e-03	C
PSZ2 G170.98+39.45		1.14e-01	1.61e-02	2.69e-02	6.51e-03	C
PSZ2 G172.63+35.15		1.84e-01	8.75e-03	2.01e-02	2.14e-03	C
PSZ2 G172.74+65.30		2.18e-01	1.10e-02	2.44e-02	1.69e-02	C+X
PSZ2 G175.60+35.47		2.66e-01	1.13e-02	1.05e-02	2.00e-03	C
PSZ2 G176.27+37.54		2.43e-01	1.69e-02	1.90e-02	3.87e-03	C
PSZ2 G179.09+60.12		5.15e-01	6.11e-03	6.54e-03	2.17e-03	C+X
PSZ2 G180.60+76.65		2.89e-01	6.39e-03	2.41e-03	5.32e-04	C
PSZ2 G180.88+31.04		1.01e-01	1.15e-02	1.83e-02	4.22e-03	X
PSZ2 G181.06+48.47		1.41e-01	1.05e-02	6.95e-02	3.04e-03	C

Table A.2. continued.

Name	Subcluster	c	$c_{\rm err}$	w	$w_{\rm err}$	X-ray
PSZ2 G182.59+55.83		2.86e-01	1.26e-02	5.95e-03	9.26e-04	C+X
PSZ2 G183.90+42.99		1.56e-01	4.77e-03	1.82e-02	1.13e-03	X
PSZ2 G184.68+28.91		2.93e-01	1.47e-02	7.89e-03	2.99e-03	C+X
PSZ2 G186.37+37.26		1.47e-01	8.43e-03	9.89e-03	5.32e-03	C+X
PSZ2 G186.99+38.65		1.99e-01	8.38e-03	3.85e-02	2.11e-03	C
PSZ2 G187.53+21.92		3.04e-01	1.59e-02	7.20e-03	5.27e-03	C+X
PSZ2 G189.31+59.24		2.45e-01	3.64e-03	4.76e-02	7.56e-04	C
PSZ2 G190.61+66.46		1.05e-01	1.61e-02	2.87e-02	5.77e-03	C
PSZ2 G192.18+56.12		1.72e-01	7.12e-03	1.70e-02	1.12e-02	C+X
PSZ2 G193.63+54.85		1.67e-01	7.38e-03	5.62e-02	1.86e-03	X
PSZ2 G194.98+54.12		1.84e-01	1.37e-02	6.07e-02	3.54e-03	C
PSZ2 G195.60+44.06	E1	9.39e-02	5.86e-03	1.94e-02	2.35e-03	X
PSZ2 G195.60+44.06	E2	1.23e-01	7.51e-03	4.63e-02	1.97e-02	C+X
PSZ2 G195.60+44.06	W1	2.83e-01	7.56e-03	8.57e-03	9.76e-04	X
PSZ2 G195.60+44.06	W2	9.70e-02	2.07e-03	4.79e-02	7.30e-04	X
PSZ2 G205.90+73.76		2.12e-01	1.79e-02	1.35e-02	3.23e-03	C

Notes. Col. 1: PSZ2 name; Col. 2: position of the subcluster; Cols. 3 and 4: concentration parameter and its error; Cols. 5 and 6: centroid shift and its error; Col. 7: instrument used (C=*Chandra*, X=*XMM-Newton*).

Table A.3. Sample of radio halos and candidate radio halos found in this work.

Name	S_{150} (2σ) [mJy]	$S_{150\mathrm{err}}$ (2σ) [mJy]	S_{150} (fit) [mJy]	$S_{150\mathrm{err}}$ (fit) [mJy]	P_{150} [W Hz^{-1}]	$P_{150\mathrm{err}}$ [W Hz^{-1}]	I_0 [μJy arcsec^{-2}]	$I_{0\mathrm{err}}$ [μJy arcsec^{-2}]	r_1 [kpc]	$r_{1\mathrm{err}}$ [kpc]	r_2 [kpc]	$r_{2\mathrm{err}}$ [kpc]	Model	S/N	rms [mJy beam^{-1}]	χ^2_{red}	Comment
PSZ2 G023.17+86.71	25.73	3.12	29.84	3.62	9.76e+24	1.18e+24	5.79	0.34	232.8	11.7	95.1	6.4	rotated_ellipse	19.81	0.347	1.18	—
PSZ2 G031.93+78.71	189.84	78.34	176.45	78.03	2.28e+24	1.01e+24	11.39	0.20	78.7	1.1			circle	66.26	0.168	3.27	—
PSZ2 G040.58+77.12	50.33	6.76	42.92	7.82	6.04e+23	1.10e+23	0.67	0.10	165.3	21.0			circle	7.01	0.082	2.46	—
PSZ2 G045.87+57.70	10.78	2.59	11.75	2.79	2.11e+25	5.03e+24	14.18	1.90	89.0	9.6			circle	9.66	0.877	1.11	—
PSZ2 G046.88+56.48	177.19	20.99	236.45	27.77	8.36e+24	9.81e+23	1.57	0.07	369.9	13.6			circle	22.46	0.131	0.70	—
PSZ2 G048.10+57.16	300.00	39.36	354.88	44.67	5.43e+24	6.84e+23	1.58	0.05	463.4	15.6	220.7	6.3	rotated_ellipse	32.61	0.160	0.87	—
PSZ2 G049.32+44.37	45.87	7.71	70.64	10.61	1.73e+24	2.59e+23	0.61	0.05	281.2	19.7			circle	12.13	0.099	0.79	—
PSZ2 G053.53+59.52	519.08	57.38	387.17	45.84	1.32e+25	1.56e+24	11.66	0.11	171.5	1.4			circle	104.71	0.141	13.68	—
PSZ2 G055.59+31.85	30.25	5.21	33.57	5.46	5.29e+24	8.60e+23	17.48	0.71	72.3	2.3			circle	30.72	0.433	1.26	—
PSZ2 G056.77+36.32	79.79	26.53	83.39	26.97	1.95e+24	6.30e+23	1.10	0.10	223.3	15.5			circle	14.15	0.099	0.79	—
PSZ2 G063.38+53.44	27.53	5.02	29.40	5.19	2.09e+25	3.70e+24	10.76	0.58	133.0	5.8			circle	20.38	0.713	1.08	—
PSZ2 G066.34+26.14	98.35	12.89	82.29	11.71	1.55e+26	2.20e+25	22.02	0.70	190.5	5.1			circle	32.77	1.304	1.60	—
PSZ2 G066.41+27.03	89.88	10.47	111.34	12.61	1.72e+26	1.95e+25	15.50	0.42	374.5	11.0	173.6	5.1	rotated_ellipse	36.36	1.096	1.05	—
PSZ2 G069.39+68.05	14.60	2.46	18.49	4.42	5.86e+25	1.40e+25	4.73	1.01	211.9	38.5			circle	4.64	0.826	0.71	—
PSZ2 G071.21+28.86	45.99	7.74	67.70	10.82	3.41e+25	5.44e+24	1.53	0.13	490.3	35.6			circle	11.08	0.260	1.32	—
PSZ2 G080.70+48.31	8.18	2.89	6.39	2.86	1.12e+24	5.03e+23	4.58	0.65	64.1	6.5			circle	8.75	0.324	0.96	—
PSZ2 G081.02+50.57	5.39	1.08	10.59	2.09	1.15e+25	2.28e+24	1.45	0.33	238.3	36.7			circle	6.46	0.175	0.87	—
PSZ2 G083.29-31.03	53.22	5.88	54.71	6.00	3.67e+25	4.03e+24	6.71	0.28	226.5	7.8			circle	26.25	0.341	1.65	—
PSZ2 G084.10+58.72	3.80	0.85	3.97	0.96	1.13e+25	2.74e+24	6.03	1.79	85.5	17.5			circle	6.49	0.320	1.05	—
PSZ2 G084.13-35.41	51.57	13.14	56.55	13.48	1.97e+25	4.69e+24	6.16	0.31	201.8	8.4			circle	20.03	0.565	1.17	—
PSZ2 G085.23+39.42	55.35	7.81	68.62	8.84	1.49e+25	1.92e+24	5.12	0.18	211.5	4.8			circle	40.12	0.262	1.80	—
PSZ2 G086.93+53.18	8.91	1.69	11.50	2.20	2.67e+25	5.09e+24	3.29	0.54	190.7	25.2			circle	7.29	0.486	1.02	—
PSZ2 G089.39+69.36	11.77	2.17	10.93	2.14	2.58e+25	5.05e+24	10.47	0.79	104.6	6.2			circle	16.23	0.532	0.83	—
PSZ2 G096.83+52.49	39.63	7.45	45.21	7.80	1.62e+25	2.80e+24	7.92	0.23	211.0	5.9	122.2	3.9	rotated_ellipse	36.70	0.417	1.53	—
PSZ2 G097.72+38.12	152.51	16.07	140.24	14.94	1.19e+25	1.27e+24	7.44	0.14	183.2	2.9			circle	55.12	0.276	1.26	—
PSZ2 G098.30-41.15	46.52	7.17	42.00	6.87	3.24e+25	5.31e+24	40.22	1.10	83.8	1.7			circle	44.54	0.746	2.24	—
PSZ2 G099.86+58.45	21.92	4.82	19.92	4.74	3.87e+25	9.21e+24	7.36	0.49	163.2	8.6			circle	15.69	0.687	1.10	—
PSZ2 G100.96-24.07	17.18	7.03	18.45	7.24	1.33e+25	5.21e+24	5.82	0.75	143.7	14.6			circle	8.78	0.544	0.95	—
PSZ2 G106.61+66.71	19.45	2.41	17.91	2.27	7.07e+24	8.98e+23	12.82	0.52	81.7	2.5			circle	32.54	0.257	1.97	—
PSZ2 G107.10+65.32	270.18	36.21	154.77	29.94	7.16e+25	9.60e+24	22.66	1.44	251.1	16.0	102.9	7.0	rotated_ellipse	17.21	0.253	2.87	P_{150} derived from S_{150} (2σ)
PSZ2 G108.27+48.66	10.26	3.30	9.39	3.23	2.17e+25	7.47e+24	6.42	0.84	123.3	12.0			circle	9.63	0.563	0.94	—
PSZ2 G109.97+52.84	13.61	1.91	16.25	2.58	6.18e+24	9.80e+23	1.39	0.16	233.5	25.0			circle	9.07	0.127	1.95	—
PSZ2 G111.75+70.37	28.12	20.02	29.28	20.05	2.90e+24	1.99e+24	2.53	0.14	218.1	12.9	105.7	6.5	rotated_ellipse	20.34	0.149	1.49	—
PSZ2 G112.48+56.99	41.72	7.00	55.16	8.36	6.71e+23	1.02e+23	0.80	0.05	160.7	9.3			circle	16.05	0.071	1.00	—
PSZ2 G113.91-37.01	78.03	8.22	122.78	13.64	6.38e+25	7.09e+24	5.09	0.23	365.3	15.0			circle	20.92	0.786	1.47	—
PSZ2 G114.31+64.89	41.10	11.72	66.61	13.27	1.83e+25	3.64e+24	12.40	0.59	143.9	6.6			circle	19.50	0.369	1.67	—
PSZ2 G115.67-27.57	4.61	0.84	4.53	0.74	3.93e+24	6.39e+23	5.00	1.33	80.3	14.0			circle	7.86	0.287	0.93	—
PSZ2 G133.60+69.04	145.00	18.87	162.80	20.30	3.43e+25	4.28e+24	7.07	0.17	377.1	5.2	200.9	4.3	rotated_ellipse	74.85	0.248	3.13	—
PSZ2 G135.17+65.43	35.76	6.89	40.76	7.35	5.46e+25	9.84e+24	6.43	0.50	232.7	12.1			circle	19.65	0.576	1.24	—
PSZ2 G138.32-39.82	28.07	4.29	31.00	4.80	8.22e+24	1.27e+24	2.89	0.24	201.7	14.3			circle	12.23	0.419	1.07	—
PSZ2 G139.18+56.37	398.78	49.86	288.44	41.53	1.47e+26	1.84e+25	45.75	0.25	170.2	0.8			circle	195.52	0.369	20.10	P_{150} derived from S_{150} (2σ)
PSZ2 G141.05-32.61	66.30	8.94	71.57	9.78	1.00e+26	1.37e+25	6.30	0.32	314.6	12.8			circle	19.40	0.525	1.68	—
PSZ2 G143.26+65.24	33.72	4.79	34.02	5.12	1.68e+25	2.53e+24	4.30	0.27	206.5	11.7			circle	16.23	0.389	1.07	—
PSZ2 G144.23-18.19	17.33	3.12	23.80	3.96	2.10e+24	3.79e+23	1.80	0.18	174.2	15.0			circle	11.02	0.214	1.05	P_{150} and r_1 computed assuming $z = 0.2$
PSZ2 G147.88+53.24	12.90	3.63	21.86	4.27	3.75e+25	7.33e+24	5.87	0.38	187.0	10.9			circle	14.18	0.595	1.03	—
PSZ2 G148.36+75.23	20.97	2.33	18.86	2.16	6.07e+24	6.95e+23	8.57	0.58	96.6	5.1			circle	18.46	0.343	1.00	—
PSZ2 G149.22+54.18	332.74	52.81	315.77	51.81	1.64e+25	2.69e+24	6.42	0.11	246.1	3.6			circle	56.88	0.234	2.07	—
PSZ2 G149.75+34.68	711.34	74.64	574.12	61.67	5.62e+25	6.04e+24	12.23	0.08	303.9	1.6			circle	157.82	0.184	7.23	—
PSZ2 G150.56+46.67	13.87	1.58	16.18	1.88	9.98e+24	1.16e+24	4.17	0.26	153.0	7.6			circle	17.50	0.388	0.96	—
PSZ2 G150.56+58.32	54.22	11.09	60.83	11.53	5.65e+25	1.07e+25	10.66	0.37	315.3	11.2	132.6	4.8	rotated_ellipse	29.55	0.607	1.22	—
PSZ2 G151.19+48.27	38.62	7.69	47.05	9.01	1.34e+25	2.57e+24	1.66	0.13	335.5	23.7			circle	11.15	0.202	0.95	—
PSZ2 G154.13+40.19	13.50	1.82	13.20	1.83	3.80e+24	5.26e+23	9.04	0.64	76.2	4.1			circle	17.60	0.422	0.89	—
PSZ2 G156.26+59.64	6.59	1.65	7.81	1.97	1.27e+25	3.22e+24	9.74	1.90	85.9	13.7			circle	6.48	0.948	0.94	—
PSZ2 G160.83+81.66	11.67	2.70	10.56	2.67	4.98e+25	1.26e+25	15.90	1.26	91.7	5.5			circle	16.69	0.647	1.21	—
PSZ2 G164.65+46.37	23.52	5.28	22.40	5.29	9.56e+24	2.26e+24	5.87	0.33	217.1	12.0	87.5	5.4	rotated_ellipse	18.86	0.413	0.89	—
PSZ2 G165.06+54.13	43.38	9.18	60.61	10.76	3.51e+24	6.23e+23	0.88	0.06	305.0	18.4			circle	14.18	0.108	0.76	—
PSZ2 G166.09+43.38	142.10	15.44	112.78	12.81	1.65e+25	1.87e+24	7.19	0.16	202.0	3.9			circle	46.32	0.210	1.39	—
PSZ2 G166.62+42.13													—				Cannot be disentangled from RR emission
PSZ2 G172.63+35.15	56.64	7.29	68.09	9.27	2.99e+24	4.07e+23	1.79	0.16	202.5	15.1			circle	12.26	0.172	1.02	—
PSZ2 G176.27+37.54	4.73	1.11	6.47	2.12	9.62e+24	3.16e+24	2.96	1.05	139.6	40.7			circle	3.47	0.375	1.10	—
PSZ2 G179.09+60.12	25.21	6.99	36.51	8.04	1.89e+24	4.17e+23	2.55	0.22	133.0	10.4			circle	11.31	0.293	1.27	—
PSZ2 G183.30+34.98	24.35	7.35	32.35	8.01	1.92e+25	4.76e+24	5.65	0.49	184.1	13.8			circle	11.63	0.761	0.92	—
PSZ2 G183.90+42.99	57.09	5.92	52.12	5.40	7.55e+25	7.81e+24	16.35	0.39	167.6	3.1			circle	45.83	0.606	1.48	—
PSZ2 G184.68+28.91	7.03	1.23	6.86	1.41	1.94e+24	3.98e+23	5.40	0.93	70.7	9.8			circle	7.17	0.473	0.64	—
PSZ2 G186.37+37.26	88.01	9.11	85.31	9.04	2.30e+25	2.44e+24	12.40	0.43	162.2	4.8			circle	30.41	0.533	1.10	—
PSZ2 G186.61+62.94	3.10	1.10	3.21	1.11	3.64e+24	1.26e+24	2.85	0.82	94.9	18.6			circle	6.61	0.191	0.53	—
PSZ2 G186.99+38.65	54.29	7.14	55.06	7.28	3.00e+25	3.96e+24	27.68	0.90	106.1	2.8			circle	35.46	0.625	1.30	—
PSZ2 G189.31+59.24	334.87	68.03	252.77	64.40	1.09e+25	2.78e+24	25.80	0.39	102.3	1.2			circle	78.08	0.189	4.63	—
PSZ2 G190.61+66.46	17.61	2.44	35.59	4.35	3.63e+25	4.44e+24	3.22	0.23	290.5	15.0			circle	16.68	0.252	1.85	—
PSZ2 G192.18+56.12	14.92	2.52	19.45	3.59	8.10e+23	1.50e+23	0.66	0.10	174.9	22.1			circle	7.24	0.102	1.01	—
PSZ2 G192.77+33.14	108.18	14.63	118.30	18.72	7.10e+23	1.12e+23	0.54	0.06	211.7	20.8			circle	9.37	0.062	0.75	—
PSZ2 G192.90+29.63	21.71	3.05	33.96	5.14	1.64e+25	2.48e+24	2.91	0.29	249.5	21.1			circle	9.53	0.412	0.88	—
PSZ2 G205.90+73.76	45.01	6.79	36.67	6.28	3.01e+25	5.15e+24	34.30	1.53	103.3	4.7	71.7	3.1	rotated_ellipse	27.79	0.763	0.72	—

Notes. Col. 1: PSZ2 name; Cols. 2 and 3: flux density integrated within the 2σ region and its error; Cols. 4 and 5: flux density obtained from the surface brightness profile fitting and its error; Cols. 6 and 7: radio power and its error; Cols. 8 and 9: best-fit central brightness and its error; Cols. 10-13: best-fit first and second *e*-folding radii and their errors; Col. 14: model adopted for the fitting; Col. 15: S/N of the radio halo; Col. 16: rms noise of the image used to fit the surface brightness profile; Col. 17: χ^2_{red} of the fit; Col. 18: comments.

Table A.4. Sample of radio relics and candidate radio relics found in this work.

Name	Position	RA_{RR} [deg]	DEC_{RR} [deg]	S_{150} [mJy]	S_{150err} [mJy]	P_{150} [W Hz^{-1}]	P_{150err} [W Hz^{-1}]	LLS [kpc]	LLS_{err} [kpc]	Width [kpc]	$Width_{err}$ [kpc]	Average SB [μJy beam^{-1}]	D_{RR-c} [kpc]	$D_{RR-cerr}$ [kpc]	D_{RR-RR} [kpc]	$D_{RR-RRerr}$ [kpc]
PSZ2 G048.10+57.16		230.0114	30.5267	264.28	26.83	3.96e+24	4.02e+23	998	35	395	182	2940	1515	206		
PSZ2 G057.61+34.93		257.7043	34.5640	426.57	42.90	6.74e+24	6.77e+23	1361	44	450	167	5579	1269	176		
PSZ2 G069.39+68.05		215.4091	38.3299	28.47	4.58	7.61e+25	1.22e+25	1489	56	109	153	1237				
PSZ2 G071.21+28.86	N	268.0816	44.7043	518.11	51.83	2.37e+26	2.37e+25	1254	39	291	149	6205	998	42	1941	39
PSZ2 G071.21+28.86	S	267.9735	44.6313	179.66	17.99	8.23e+25	8.24e+24	813	39	136	86	5134	965	42	1941	39
PSZ2 G080.16+57.65		225.5644	47.1942	37.63	4.78	7.27e+23	9.24e+22	1073	50	173	86	1667	1418	196		
PSZ2 G086.58+73.11		205.9581	39.9924	4.28	0.66	6.22e+23	9.53e+22	394	44	121	42	584				
PSZ2 G089.52+62.34	N2	215.8002	48.7878	92.49	9.94	1.10e+24	1.19e+23	1213	35	296	200	2742	1721	233		
PSZ2 G089.52+62.34	N1	215.5888	48.5719	50.64	6.63	6.04e+23	7.90e+22	273	35	107	39	5147	484	74		
PSZ2 G091.79-27.00		341.3831	28.2727	16.48	2.55	7.36e+24	1.14e+24	1535	41	164	96	1176	2510	339		
PSZ2 G096.43-20.89		341.9545	35.5495	33.56	4.16	1.38e+25	1.71e+24	1482	53	279	173	839				
PSZ2 G099.48+55.60	N	216.8435	57.0057	108.16	11.44	3.04e+24	3.22e+23	1711	45	354	173	1398	1366	49	2405	45
PSZ2 G099.48+55.60	S	217.2878	56.7582	69.38	7.49	1.95e+24	2.11e+23	1090	45	229	160	1609	1068	48	2405	45
PSZ2 G107.10+65.32		203.2562	50.4015	21.49	2.25	5.29e+24	5.53e+23	538	50	266	113	1258	1211	170		
PSZ2 G109.22-44.01		2.6228	17.7278	148.71	15.75	1.24e+25	1.31e+24	1168	40	211	100	3216				
PSZ2 G111.75+70.37		198.3618	46.3271	120.37	12.07	1.14e+25	1.14e+24	874	56	317	93	4520	898	133		
PSZ2 G113.91-37.01	N	4.9365	25.3543	164.61	16.57	7.78e+25	7.84e+24	1172	43	412	155	2033	1210	47	2605	43
PSZ2 G113.91-37.01	S	4.8569	25.2329	40.41	4.43	1.91e+25	2.10e+24	1481	43	296	128	1361	1464	49	2605	43
PSZ2 G116.50-44.47		8.0645	18.1766	13.00	1.54	7.17e+24	8.48e+23	555	47	118	79	946	890	128		
PSZ2 G121.03+57.02		194.9253	60.0416	12.26	1.57	4.86e+24	6.21e+23	542	44	141	45	759	570	88		
PSZ2 G135.17+65.43		184.7975	50.8694	6.61	0.93	7.78e+24	1.10e+24	654	54	125	63	552	1110	158		
PSZ2 G144.99-24.64		37.2926	33.9827	10.45	2.12	1.07e+24	2.18e+23	773	48	153	82	749				
PSZ2 G151.19+48.27		154.4696	59.5328	19.24	2.05	5.09e+24	5.44e+23	812	43	122	90	816	682	101		
PSZ2 G165.46+66.15	N	170.8381	43.1768	89.07	9.43	9.79e+24	1.04e+24	1069	49	339	120	2270	843	51	2115	49
PSZ2 G165.46+66.15	S	170.9279	43.0079	171.63	17.51	1.89e+25	1.92e+24	1638	49	385	188	2571	1387	53	2115	49
PSZ2 G166.62+42.13	W	137.2336	51.5893	454.39	45.53	7.29e+25	7.30e+24	1901	39	718	238	2529	1462	200		
PSZ2 G166.62+42.13	N	137.4405	51.6072	32.37	3.67	5.19e+24	5.88e+23	932	39	364	163	675	917	129		
PSZ2 G166.62+42.13	E	137.5390	51.5332	12.21	6.52	1.96e+24	1.05e+24	1100	39	148	71	1080	1204	166		
PSZ2 G181.06+48.47	N	144.9131	40.8741	28.22	2.98	4.89e+24	5.17e+23	1394	39	135	67	925	1660	47	2694	39
PSZ2 G181.06+48.47	S	144.8281	40.6879	66.76	6.83	1.16e+25	1.18e+24	1660	39	207	122	1083	1035	42	2694	39
PSZ2 G186.99+38.65		132.5838	36.1125	12.42	1.58	6.14e+24	7.80e+23	723	46	136	73	705	1030	145		
PSZ2 G190.61+66.46		166.5720	33.5517	60.49	6.43	5.48e+25	5.82e+24	573	48	184	180	2331	865	126		
PSZ2 G198.46+46.01		142.7257	28.7635	41.68	4.64	1.19e+25	1.33e+24	1494	43	247	172	694				
PSZ2 G205.90+73.76	N	174.5111	27.9806	5.37	0.97	3.95e+24	7.12e+23	664	48	125	42	791	1490	53	2958	48
PSZ2 G205.90+73.76	S	174.5439	27.8404	7.55	1.12	5.55e+24	8.26e+23	655	48	155	58	1028	1540	54	2958	48

Notes. Col. 1: PSZ2 name; Col. 2: position of the relic with respect to the cluster; Cols. 3 and 4: coordinates of the radio relic; Cols. 5 and 6: flux density; Cols. 7 and 8: radio power and its error; Cols. 9 and 10: largest-linear size and its error; Cols. 11 and 12: width and its error; Col. 13: average surface brightness; Cols. 14 and 15: distance between radio relic and X-ray centroid and its error; Cols. 16 and 17: distance between double radio relics and its error.

Appendix B: Image gallery

Figure B.1 shows a collection of LOFAR images of the targets in our LoTSS-DR2/PSZ2 sample.

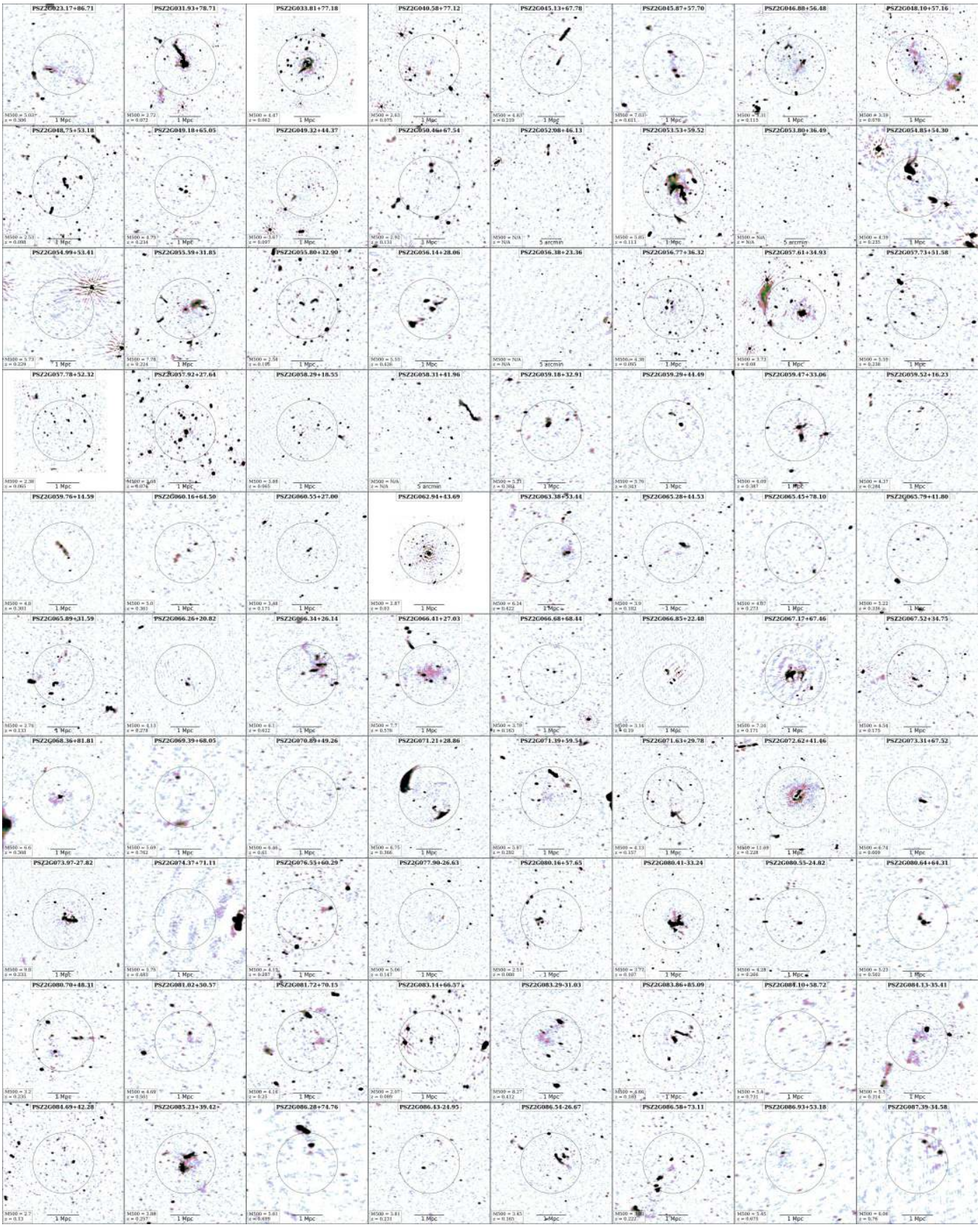

Fig. B.1. LOFAR image gallery of the targets in our sample, excluding the five objects for which it was not possible to apply the extraction + recalibration scheme (see end of Sect. 3.1). The collage is available at full resolution on the project website, `https://lofar-surveys.org/planck_dr2.html`.

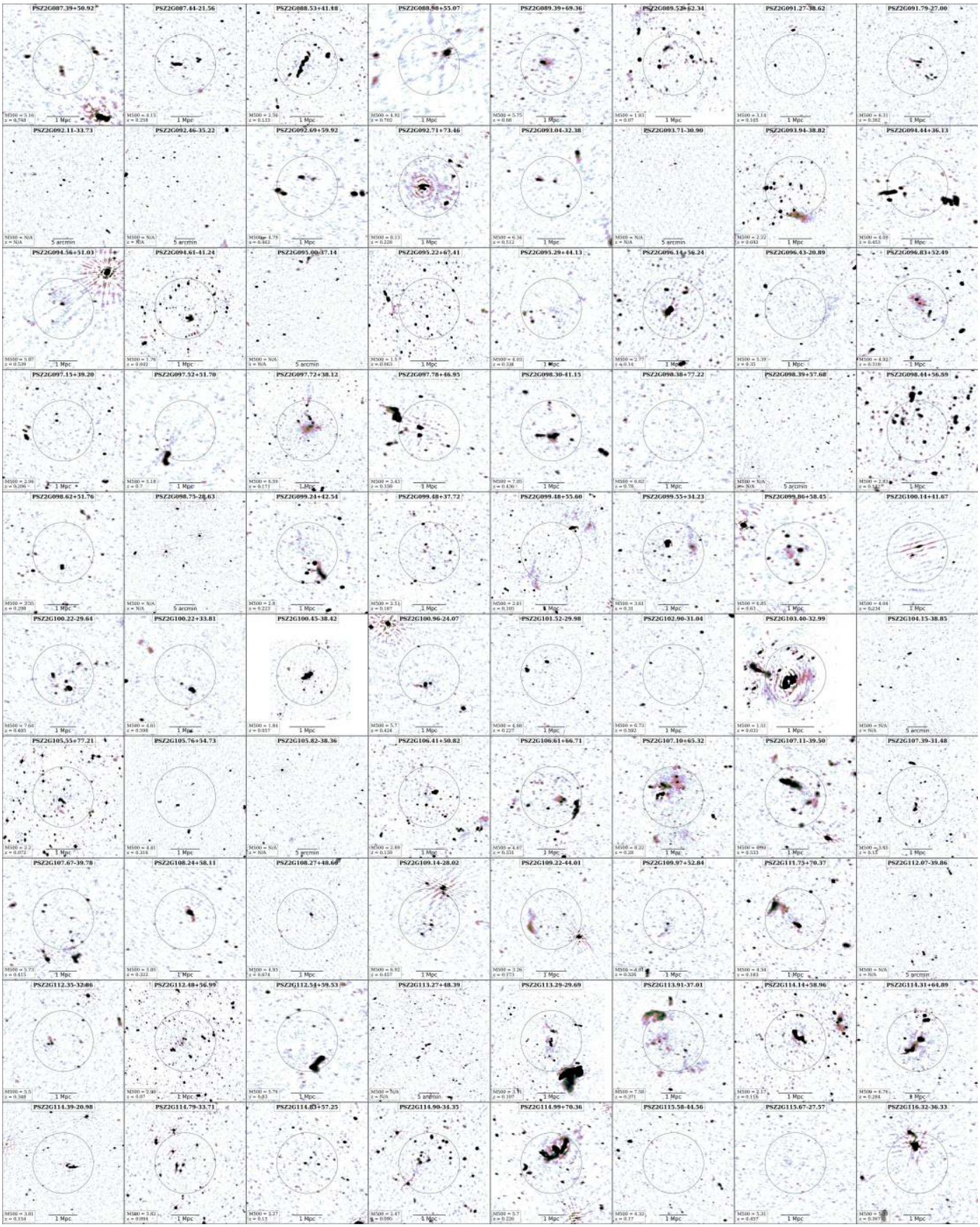

Fig. B.1. continued.

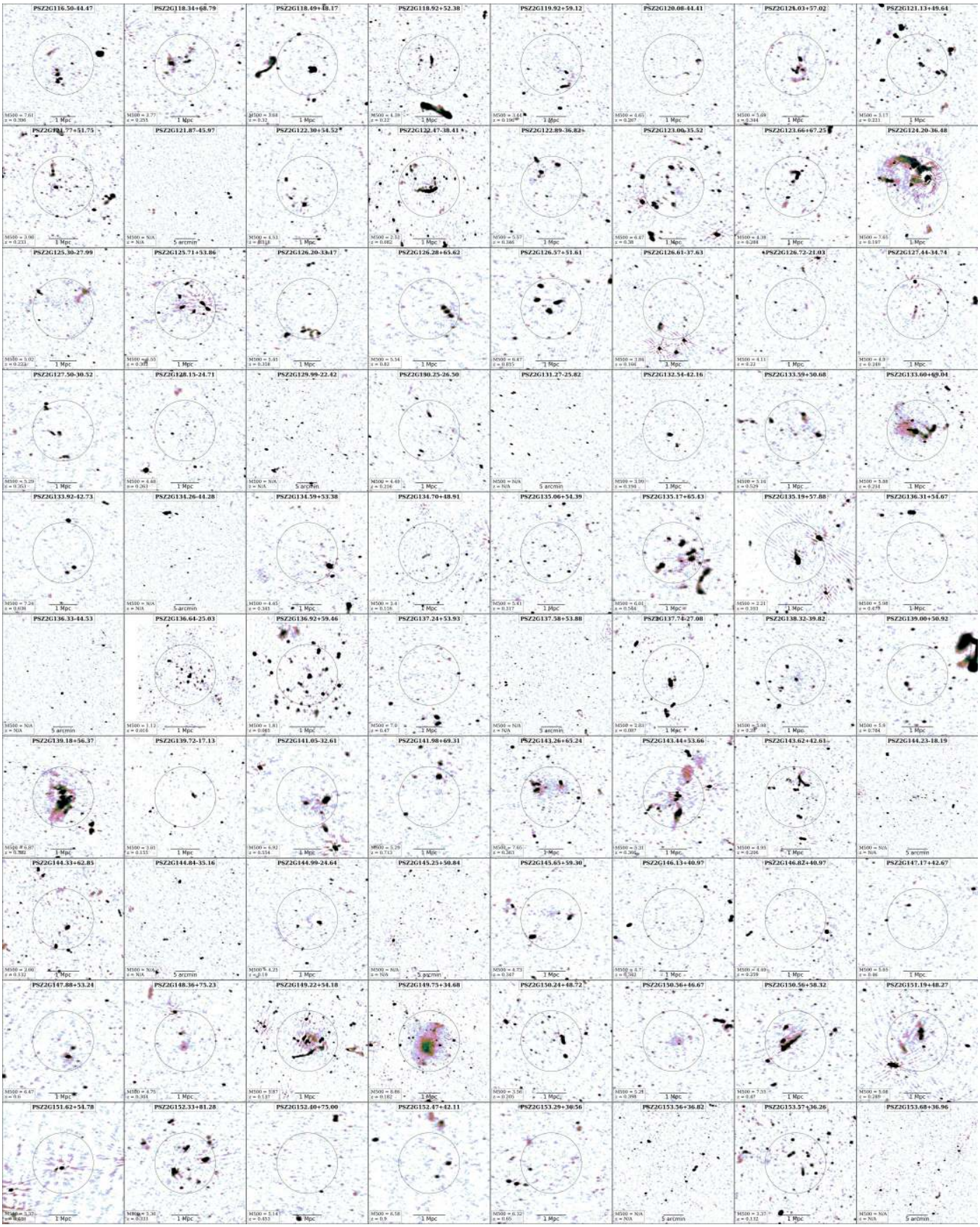

Fig. B.1. continued.

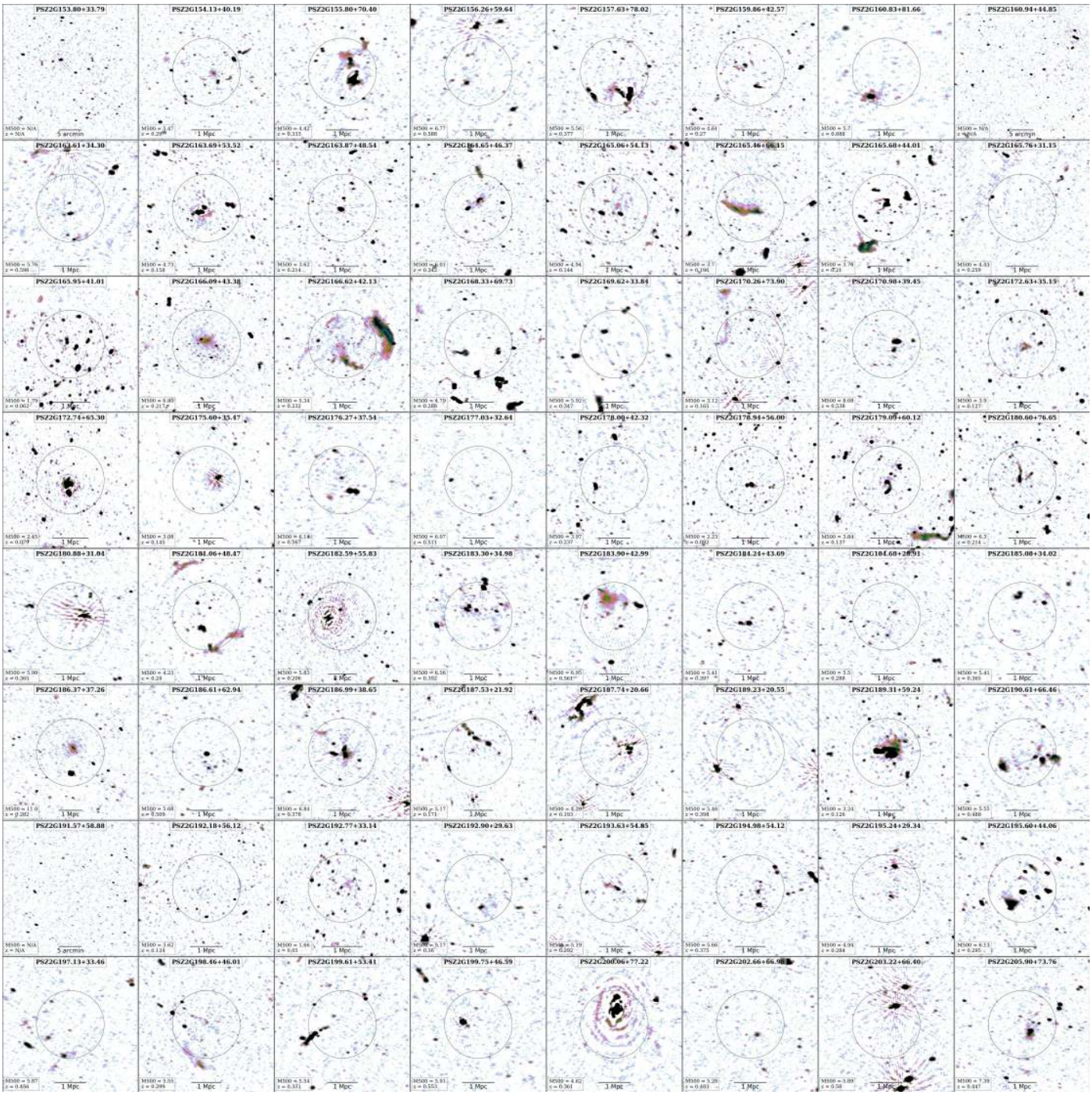

Fig. B.1. continued.

Appendix C: Comparison between flux density measurements for radio halos

Here we compare the flux density for the radio halos obtained by fitting their surface brightness profile with Halo-FDCA ($S_{\rm fit}$) and by manual integration of a circular/elliptical region encompassing the 2σ level contour ($S_{2\sigma}$). In both cases, regions affected by residual calibration errors and/or contaminating extended sources were masked out and the flux density beneath them was extrapolated assuming the best-fit model (in the case of Halo-FDCA) or the average surface brightness of the halo in the non-masked region (in the case of the manual measurement). The left panel of Fig. C.1 shows that there is a general agreement between the two measurements, although a few outliers are present.

We inspected the radio images and results of the fitting for all clusters and found that the outliers may indicate cases in which Halo-FDCA provides a unreliable fit because of the low significance of the radio halo. To verify this, we produce the plot shown in the right panel of Fig. C.1, which shows the ratio between the best-fit value of the central surface brightness I_0 and the 3σ noise of the map as a function of the $S_{\rm fit}/S_{2\sigma}$ ratio. We observe a trend between the plotted quantities, noting indeed that the halos where the two flux density measurements are in most disagreement (large $S_{\rm fit}/S_{2\sigma}$ values) are typically those with lowest $I_0/3\sigma$. Our interpretation is that when the radio halo is observed with low significance, Halo-FDCA does not converge on the diffuse emission but it provides a nonphysical best fit with a low I_0 and a large r_1, basically fitting the image noise. Importantly, these nonphysical best-fit models have still good S/N and $\chi^2_{\rm red}$ values and corner plots as the fit is still converged; thus, they cannot be simply rejected by using these tools. We therefore used the right panel of Fig. C.1 as diagnostic plot, adopting the arbitrary thresholds

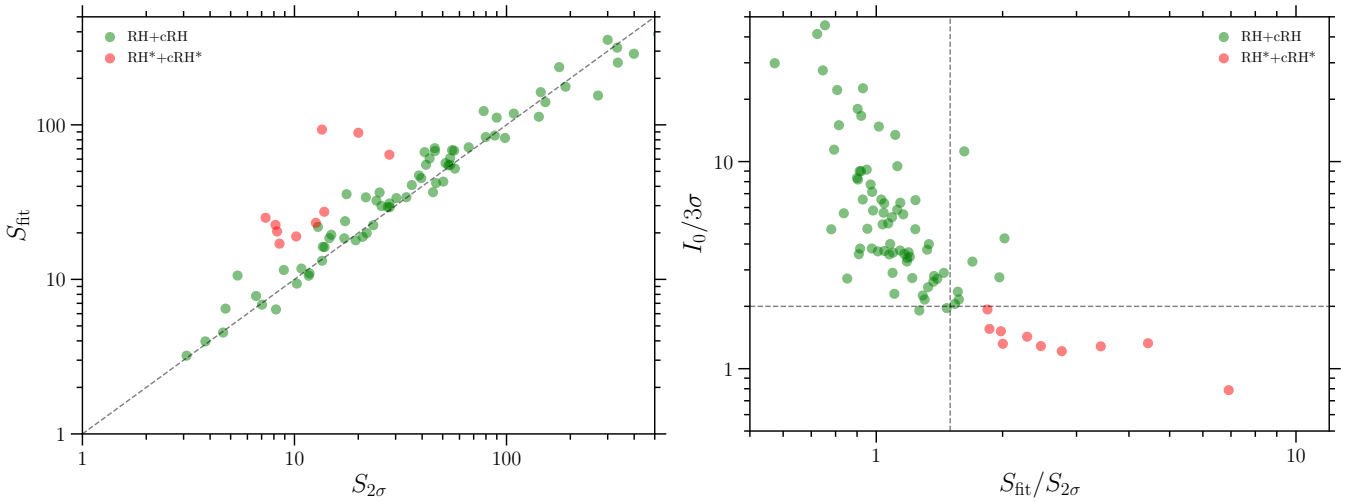

Fig. C.1. Flux density measurements for radio halos. *Left*: Comparison between the flux density derived with Halo-FDCA ($S_{\rm fit}$) and that obtained manually within the 2σ contour ($S_{2\sigma}$). The dashed line indicates the linear correlation as a reference. *Right*: Diagnostic plot used to determine when Halo-FDCA does not provide a reliable flux density measurement due to the low significance of the radio halo. The dashed lines indicate the thresholds of $S_{\rm fit}/S_{2\sigma} > 1.5$ and $I_0/3\sigma < 2$ that were used to identify the sources that were classified as radio halos or candidate radio halos with the decision tree of Fig. 4, but whose flux density was not considered reliable. These sources are reported in red and in the manuscript are referred to as RH* and cRH*.

Table C.1. Sample of radio halos and candidate radio halos that were classified with an asterisk (the RH* and cRH* in Table A.1) because of their low significance. The integrated flux density of these sources cannot be determined accurately with current data.

Name	S_{150} (2σ) [mJy]	$S_{150\rm err}$ (2σ) [mJy]	S_{150} (fit) [mJy]	$S_{150\rm err}$ (fit) [mJy]	P_{150} [W Hz^{-1}]	$P_{150\rm err}$ [W Hz^{-1}]	I_0 [μJy arcsec^{-2}]	$I_{0\rm err}$ [μJy arcsec^{-2}]	r_1 [kpc]	$r_{1\rm err}$ [kpc]	Model	S/N	rms [mJy beam^{-1}]	$\chi^2_{\rm red}$
PSZ2 G071.39+59.54	20.01	2.30	88.87	11.90	2.60e+25	3.48e+24	1.27	0.08	529.2	36.0	circle	11.25	0.319	1.15
PSZ2 G076.55+60.29	8.14	1.67	22.52	5.72	6.33e+24	1.61e+24	0.43	0.07	453.8	82.3	circle	4.40	0.118	0.76
PSZ2 G077.90-26.63	28.02	4.04	64.10	10.75	3.89e+24	6.52e+23	1.88	0.24	218.1	26.5	circle	7.53	0.439	1.03
PSZ2 G095.29+44.13	13.82	2.08	27.38	4.36	1.08e+25	1.72e+24	1.21	0.13	328.7	32.8	circle	8.48	0.266	0.89
PSZ2 G099.55+34.23	13.48	5.97	93.17	19.09	3.14e+25	6.44e+24	0.56	0.07	851.0	112.6	circle	5.95	0.237	0.84
PSZ2 G116.50-44.47	12.62	6.73	23.23	8.29	1.42e+25	5.05e+24	3.94	0.78	187.8	36.0	circle	5.11	0.680	1.08
PSZ2 G118.34+68.79	7.31	2.48	25.05	4.47	5.33e+24	9.52e+23	0.80	0.09	321.5	32.4	circle	8.58	0.208	1.34
PSZ2 G123.00-35.52	8.28	1.86	20.43	4.27	1.13e+25	2.35e+24	2.23	0.35	228.4	34.4	circle	5.93	0.578	1.08
PSZ2 G133.59+50.68	10.19	1.45	18.96	3.35	2.37e+25	4.18e+24	1.20	0.15	362.8	43.6	circle	7.07	0.257	0.92
PSZ2 G163.61+34.30	8.50	2.19	17.02	3.71	2.87e+25	6.25e+24	1.50	0.24	324.7	44.9	circle	6.21	0.379	0.79

Notes. Col. 1: PSZ2 name; Cols. 2 and 3: flux density integrated within the 2σ region and its error; Cols. 4 and 5: flux density obtained from the surface brightness profile fitting and its error; Cols. 6 and 7: radio power and its error; Cols. 8 and 9: best-fit central brightness and its error; Cols. 10 and 11: best-fit e-folding radius and its error; Col. 12: model adopted for the fitting; Col. 13: S/N of the radio halo; Col. 14: rms noise of the image used to fit the surface brightness profile; Col. 15: $\chi^2_{\rm red}$ of the fit.

of $S_{\rm fit}/S_{2\sigma} > 1.5$ and $I_0/3\sigma < 2$ to identify the bad cases. These radio halos and candidate radio halos are marked with an asterisk in Table A.1 (i.e., RH*/cRH*) and represent 10 out of the 83 fitted halos. They are collected in Table C.1. Deeper LOFAR observations are required to reliably determine the integrated flux density of the halo emission in these clusters.

Appendix D: Notes on individual clusters

In the following, we make specific remarks for some clusters of our sample.

PSZ2 G023.17+86.71 The radio halo is elongated in the E-W direction and it is claimed in this paper for the first time.

PSZ2 G031.93+78.71 (A1775) It hosts a prominent head-tail radio galaxy that has been studied in the past (Owen & Ledlow 1997; Giovannini & Feretti 2000; Giacintucci et al. 2007; Terni de Gregory et al. 2017). The presence in the cluster center of a radio halo bounded by a cold front was recently claimed by Botteon et al. (2021b) using LoTSS data, who referred to this emission as a "slingshot" radio halo. Toward the SE, a diffuse source elongated along the N-S direction and with uncertain nature is also observed.

PSZ2 G033.81+77.18 (A1795) Past observations with the VLA and GMRT found the presence of diffuse emission in the cluster center, which may be related to a mini-halo or AGN activity (Giacintucci et al. 2014; Kokotanekov et al. 2018). Due to the bad data quality, we cannot perform the analysis of this system. Bîrzan et al. (2020) used LOFAR data to search for an association between the central radio source and the X-ray cavity in the NW, but found none. A paper presenting the analysis of this system using the LOFAR international baselines is currently in preparation (Timmerman et al., in preparation).

PSZ2 G040.58+77.12 (A1800) The radio halo is claimed here for the first time. A roundish region of emission without clear optical counterpart is observed in the S.

PSZ2 G045.87+57.70 The presence of diffuse emission in this cluster was originally claimed by Di Gennaro et al. (2021a) using LoTSS data. We confirm the central emission and following our decision tree we classified it as radio halo.

PSZ2 G046.88+56.48 (A2069) This is a bimodal cluster in which the first detection of megaparsec-scale radio emission was claimed by Farnsworth et al. (2013). Drabent et al. (2015) found extended emission in both components. This is confirmed by our images, in which the radio emission seems to embed the whole system (including the region in-between the two subclusters). The detailed analysis of the LOFAR observations of this target will be presented by Drabent et al. (in preparation).

PSZ2 G048.10+57.16 (A2061) It hosts a radio halo and a relic in the SW direction, which have already been claimed (Rudnick & Lemmerman 2009; van Weeren et al. 2011; Farnsworth et al. 2013). In our images, the radio halo remarkably follows the X-ray emission, which is stretched along the SW-NE direction, and is connected with the radio relic with a trail of emission. The detailed analysis of the LOFAR observations of this target will be presented by Drabent et al. (in preparation).

PSZ2 G049.32+44.37 (A2175) The radio halo is claimed here for the first time.

PSZ2 G053.53+59.52 (A2034) Diffuse radio emission in the center of this cluster was noticed by different authors (Kempner & Sarazin 2001; Rudnick & Lemmerman 2009; Giovannini et al. 2009; van Weeren et al. 2011). Shimwell et al. (2016) provided the clearest view of the diffuse radio sources in this system to date using LOFAR observations. They claimed the presence of a radio halo with filamentary structures and a number of sources in the cluster outskirts with unclear origin. Our new LoTSS images confirm the structures observed by Shimwell et al. (2016). This cluster is displayed in Fig. 5.

PSZ2 G055.59+31.85 (A2261) Hints of diffuse emission in this system were first noticed with VLA 1.4 GHz observations by Venturi et al. (2008), but not confirmed with GMRT 235 and 610 MHz data by Kale et al. (2013). Sommer et al. (2017) reanalyzed these radio observations and claimed to detect the presence of megaparsec-scale emission in the cluster, which was classified as a radio halo. The radio halo was confirmed by LOFAR observations (Savini et al. 2019). Our images agree with these findings.

PSZ2 G056.77+36.32 (A2244) The radio halo is claimed here for the first time.

PSZ2 G057.61+34.93 (A2249) The presence of a radio relic in the E was recently reported with LOFAR and uGMRT data by Locatelli et al. (2020). The relic is confirmed in our image while we classified as uncertain the emission in the cluster center due to the presence of artifacts from the bright central AGN.

PSZ2 G057.80+88.00 (Coma cluster) It hosts the prototypical radio halo and relic, which have been studied in the past with numerous instruments (e.g., Kim et al. 1989; Giovannini et al. 1991, 1993; Thierbach et al. 2003; Feretti & Neumann 2006; Bonafede et al. 2010; Brown & Rudnick 2011). Due to its large angular size, the analysis of LOFAR data for this cluster requires a special treatment. For this reason, this cluster was excluded from our analysis. Results on this system using LOFAR observations have been recently reported by Bonafede et al. (2021); Bonafede et al. (2022).

PSZ2 G058.29+18.55 It is a double galaxy cluster, comprising RXC J1825.3+3026 (dubbed subcluster E in Table A.2) and CIZA J1824.1+3029 (dubbed subcluster W in Table A.2). It also known as Lyra complex, in which the presence of a radio halo in RXC J1825.3+3026 was claimed with a targeted LOFAR observation by Botteon et al. (2019a). Due to the bad quality of LoTSS data, we could not perform the analysis of this system.

PSZ2 G063.38+53.44 The candidate radio halo is claimed here for the first time.

PSZ2 G066.34+26.14 The candidate radio halo is claimed here for the first time.

PSZ2 G066.41+27.03 The radio halo is claimed here for the first time.

PSZ2 G067.17+67.46 (A1914) The intricate emission from this system was noticed by early observations with the VLA by Bacchi et al. (2003). Past LOFAR observations found the presence of very steep spectrum emission in the cluster due to very bright revived fossil plasma, a radio halo, and a head-tail radio galaxy (Mandal et al. 2019). Due to the complex emission of this system, we classified it as uncertain. We refer the reader to Mandal et al. (2019) for more details.

PSZ2 G068.36+81.81 We interpreted the diffuse emission from this cluster as the radio lobes of the central AGN. Therefore, we classified this cluster as NDE.

PSZ2 G069.39+68.05 A faint candidate radio halo is noticed in the lowest-resolution images. An elongated region of emission in the S is classified as candidate radio relic. These two sources are claimed here for the first time.

PSZ2 G071.21+28.86 (MACS J1752.0+4440) It is a textbook example of a double radio relic that has been reported in the past using GMRT and WSRT observations (van Weeren et al. 2012; Bonafede et al. 2012). A faint radio halo was claimed by van Weeren et al. (2012) and it is confirmed by our images. This cluster is displayed in Fig. 5.

PSZ2 G071.39+59.54 Central diffuse emission in form of a radio halo is observed here for the first time. Since the fitting of the radio halo surface brightness profile does not provide reliable results, we classified this emission as RH*.

PSZ2 G072.62+41.46 (A2219) It hosts a radio halo detected in the NVSS (Giovannini et al. 1999) and confirmed in deeper VLA observation at 1.4 GHz (Bacchi et al. 2003) and 325 MHz (Orrù et al. 2007). Our LOFAR images of this cluster are affected by bad quality due to the presence of the strong AGN located in the cluster center. Therefore, we could not perform the analysis of this system.

PSZ2 G073.97-27.82 (A2390) Originally, this cluster was classified as a mini-halo by Bacchi et al. (2003) using VLA data at 1.4 GHz. Later, Sommer et al. (2017) analyzed deeper and wide-band VLA data at 1−2 GHz and reclassified the emission as radio halo. Past LOFAR observations revealed that the central radio galaxy may account for most or even all the radio flux that was attributed to the radio halo (Savini et al. 2019). In this paper, we interpret all the radio emission observed in this system as lobes of the central AGN. Another LOFAR work highlighted how these radio lobes are filling the X-ray cavities in the ICM (Bîrzan et al. 2020).

PSZ2 G076.55+60.29 The X-ray emission of the cluster is offset with respect to the position provided by the PSZ2 catalog. Faint emission in the form of a radio halo is noticed here for the first time. Since the fitting of the radio halo surface brightness profile does not provide reliable results, we classified this emission as RH*.

PSZ2 G077.90-26.63 (A2409) Central diffuse emission in form of a radio halo is observed here for the first time. Since the fitting of the radio halo surface brightness profile does not provide reliable results, we classified this emission as RH*.

PSZ2 G080.16+57.65 (A2018) A radio relic in the E direction was discovered together with a candidate radio halo by van Weeren et al. (2021) in the analysis of the LoTSS-DR1 cluster sample. More recently, Paul et al. (2021) confirmed the presence of the two sources using uGMRT data at 300−500 MHz. In this paper, we confirm only the presence of the radio relic.

PSZ2 G080.41-33.24 (A2443) This cluster is known to host complex radio emission with an ultra-steep spectrum in the form of revived fossil plasma (Cohen & Clarke 2011; Clarke et al. 2013), which is well recovered in our LOFAR images.

PSZ2 G080.70+48.31 (A2136) The candidate radio halo is claimed here for the first time.

PSZ2 G081.02+50.57 The radio halo is claimed here for the first time.

PSZ2 G081.72+70.15 (A1838) This system hosts two elongated sources with uncertain origin that are located outside the bulk of the X-ray emission. We did not classified these sources as radio relics as they do not show a sharp surface brightness edge in the LOFAR images.

PSZ2 G083.29-31.03 The radio halo is claimed here for the first time.

PSZ2 G084.10+58.72 The presence of diffuse emission at the center of this cluster was originally noted by previous LOFAR studies (Di Gennaro et al. 2021b,a; van Weeren et al. 2021), belonging to the LoTSS-DR1 area. Here, we confirm the emission and claim the presence of a radio halo.

PSZ2 G084.13-35.41 (A2472) The radio halo is claimed here for the first time. An uncertain source with a wedge-shape is also observed to the S of the radio halo.

PSZ2 G085.23+39.42 The candidate radio halo is claimed here for the first time. The diffuse emission is embedded into two bright structures likely associated with cluster radio galaxies.

PSZ2 G086.58+73.11 The galaxy overdensity seems located toward the SE with respect to the cluster coordinates reported in the PSZ2 catalog. To the S of the optical overdensity, we observed an elongated emission that we classify as candidate radio relic. This relic is claimed here for the first time. The presence of diffuse emission in the central region of the cluster is uncertain due to the artifacts introduced by the source subtraction.

PSZ2 G086.93+53.18 The presence of a radio halo in this cluster has been recently studied with LOFAR by Di Gennaro et al. (2021b,a). This systems belongs to the LoTSS-DR1 area and was also reported by van Weeren et al. (2021). Here, we confirm the emission.

PSZ2 G088.53+41.18 (A2208) This cluster hosts a peculiar emission that is likely associated with radio galaxies. This cluster is displayed in Fig. 5.

PSZ2 G089.39+69.36 The presence of a radio halo in this cluster was recently claimed and studied with LOFAR and uGMRT data (Di Gennaro et al. 2021b,a). Here, we confirm the emission.

PSZ2 G089.52+62.34 (A1904) Two radio relics located on the same side of the cluster (NE) have been firstly claimed by van Weeren et al. (2021) during the analysis of the LoTSS-DR1 cluster sample. We confirm the two detections. Recently, the innermost relic was detected also with the uGMRT at 300−500 MHz (Paul et al. 2021).

PSZ2 G091.79-27.00 The radio relic is claimed here for the first time.

PSZ2 G093.94-38.82 (A2572) This is a system with multiple cluster components in the X-rays, with the main component that we dubbed PSZ2 G093.94-38.82 W and two smaller sub-clumps that we dubbed PSZ2 G093.94-38.82 EN and PSZ2 G093.94-38.82 ES in Table A.2. We discover an extended diffuse source in the S of PSZ2 G093.94-38.82 W that has an uncertain origin.

PSZ2 G094.61-41.24 (A2589) Diffuse emission at the center of this cluster is noticed only in the image tapered at 100 kpc resolution. Due to the possible blend of partially subtracted sources at low resolution, we classified the emission as uncertain.

PSZ2 G095.22+67.41 Patches of emission with low significance and uncertain origin are observed in the cluster center and cluster outskirts. The peripheral emission on the E was classified as a candidate radio relic during the analysis of the LoTSS-DR1 sample (van Weeren et al. 2021).

PSZ2 G095.29+44.13 Central diffuse emission in form of a candidate radio halo is observed here for the first time. Since the fitting of the radio halo surface brightness profile does not provide reliable results, we classified this emission as cRH*.

PSZ2 G096.43-20.89 The candidate radio relic is claimed here for the first time.

PSZ2 G096.83+52.49 (A1995) Extended emission at the center of this cluster was firstly reported by Giovannini et al. (2009) with VLA 1.4 GHz observations. Our images confirm the presence of a radio halo in this system.

PSZ2 G097.72+38.12 (A2218) Diffuse radio emission in the form of a radio halo in this system was originally reported by Moffet & Birkinshaw (1989) and later confirmed by other authors (Giovannini & Feretti 2000; Kempner & Sarazin 2001). In our image, the halo is slightly elongated in the E-W direction and it has an extension toward N. This cluster is displayed in Fig. 5.

PSZ2 G098.30-41.15 The candidate radio halo is claimed here for the first time.

PSZ2 G099.24+42.54 Radio emission with uncertain origin (due to the possible contribution of partially subtracted discrete sources) is noticed in the cluster center. Another emission in the SW with unclear origin is observed.

PSZ2 G099.48+37.72 (A2216) Extended emission is noticed only in the lowest-resolution radio emission. Due to the possible contribution of partially subtracted discrete sources, we classified it as uncertain.

PSZ2 G099.48+55.60 (A1925) This is a double radio relic system and it is claimed here for the first time.

PSZ2 G099.55+34.23 Central diffuse emission in form of a candidate radio halo is observed here for the first time. Since the fitting of the radio halo surface brightness profile does not provide reliable results, we classified this emission as cRH*. Another source elongated in the N-S direction with uncertain origin is located W to the cluster center.

PSZ2 G099.86+58.45 The radio halo in this cluster was claimed by previous LOFAR observations (Cassano et al. 2019; Di Gennaro et al. 2021b,a; van Weeren et al. 2021) and is confirmed in our images.

PSZ2 G100.14+41.67 (A2146) This cluster hosts a double radio relic system that has been observed with the VLA and LOFAR (Hlavacek-Larrondo et al. 2018; Hoang et al. 2019). Due to the bad data quality, we could not perform the analysis of this system.

PSZ2 G100.45-38.42 (A2626) Peculiar emission in form of four arcs was observed in this system (Gitti et al. 2004; Gitti 2013; Kale & Gitti 2017; Ignesti et al. 2017), which led to the nickname of Kite cluster. Recent LOFAR observations suggest that the emission originate from the central radio galaxy whose fossil radio plasma has been compressed and revived as a consequence of motions of the ICM (Ignesti et al. 2020).

PSZ2 G100.96-24.07 The candidate radio halo is claimed here for the first time.

PSZ2 G105.55+77.21 (A1691) Extended emission is noticed only in the lowest-resolution radio image. Due to the possible contribution of partially subtracted discrete sources, we classified it as uncertain.

PSZ2 G106.41+50.82 (A1918) Possible diffuse radio emission is observed at the center of the cluster. However, due to an artifact introduced by the discrete source subtraction, we classified the diffuse emission as uncertain.

PSZ2 G106.61+66.71 Central diffuse emission in form of a radio halo was discovered by van Weeren et al. (2021) in the analysis of the LoTSS-DR1 cluster sample and was later confirmed by Paul et al. (2021). Our images agree with previous results.

PSZ2 G107.10+65.32 (A1758) This is a double galaxy cluster (dubbed PSZ2 G107.10+65.32 N and PSZ2 G107.10+65.32 S in Table A.2) that has been intensively studied in the past with different instruments (Kempner & Sarazin 2001; Giovannini et al. 2009; Venturi et al. 2013; Botteon et al. 2018, 2020b; Schellenberger et al. 2019; van Weeren et al. 2021). It hosts a double radio halo system (Botteon et al. 2018), and the two cluster components are connected with a bridge of radio emission (Botteon et al. 2020b). The northern cluster hosts revived fossil plasma emission and the southern system hosts a radio relic. Our images agree with previous results.

PSZ2 G108.27+48.66 The candidate radio halo is claimed here for the first time.

PSZ2 G109.22-44.01 The candidate radio relic is claimed here for the first time.

PSZ2 G109.97+52.84 The radio halo is claimed here for the first time.

PSZ2 G111.75+70.37 (A1697) The relic and halo in this system were firstly reported by Paul et al. (2020). This cluster belongs to the LoTSS-DR1 sample presented by van Weeren et al. (2021). Our images confirm the presence of an elongated radio halo and a relic in the NE with a long trail of emission.

PSZ2 G112.48+56.99 (A1767) The radio halo is claimed here for the first time.

PSZ2 G113.29-29.69 Diffuse emission is observed at the center of the cluster. Due to the artifacts introduced by the subtraction of discrete sources, we classified it as uncertain.

PSZ2 G113.91-37.01 The radio halo and relics are claimed here for the first time. This is a double radio relic system. This cluster is displayed in Fig. 5.

PSZ2 G114.31+64.89 (A1703) Hints of diffuse radio emission in this cluster were noticed with the VLA by Owen et al. (1999) and with LOFAR by Savini et al. (2018b). Recently, van Weeren et al. (2021) confirmed the presence of a radio halo during the analysis of the LoTSS-DR1 sample. Our images agree with previous findings.

PSZ2 G114.99+70.36 (A1682) This systems hosts complex diffuse emission associated with the ICM and radio galaxies that has been studied in the past with GMRT and LOFAR (Venturi et al. 2008, 2011, 2013; Macario et al. 2013; Clarke et al. 2019; van Weeren et al. 2021). Due to the difficulty of disentangling the diffuse emission, we classified it as uncertain. This cluster is displayed in Fig. 5.

PSZ2 G116.32-36.33 There are two separate X-ray components for this cluster, RX J0027.8+2616 and WHL J002727.0+260707. They are dubbed PSZ2 G116.32-36.33 N and PSZ2 G116.32-36.33 S in Table A.2 respectively. RX J0027.8+2616 is the target of the *Chandra* observation and it is within the FoV of the *XMM-Newton* observation targeted at WHL J002727.0+260707.

PSZ2 G116.50-44.47 Central diffuse emission in form of a radio halo is observed here for the first time. Since the fitting of the radio halo surface brightness profile does not provide reliable results, we classified this emission as RH*. We also report for the first time a radio relic located in the N.

PSZ2 G118.34+68.79 The presence of a candidate radio halo was claimed during the analysis of the LoTSS-DR1 sample (van Weeren et al. 2021). Our images confirm the presence of central diffuse emission in form of a candidate radio halo. Since the fitting of the radio halo surface brightness profile does not provide reliable results, we classified this emission as cRH*.

PSZ2 G121.03+57.02 The radio relic in the S of the cluster is located where there is an apparent jump of the X-ray surface brightness and it is claimed here for the first time. The emission in the center has uncertain origin due to the possible residual of discrete source subtraction.

PSZ2 G123.00-35.52 Central diffuse emission in form of a radio halo is observed here for the first time. Since the fitting of the radio halo surface brightness profile does not provide reliable results, we classified this emission as RH*.

PSZ2 G124.20-36.48 (A115) A prominent and bright radio relic in the N periphery of the system was originally claimed with VLA 1.4 GHz observations by Govoni et al. (2001). Follow-up studies focused on the connection between relic and shock (Botteon et al. 2016), also exploiting GMRT observations at 610 MHz (Hallman et al. 2018). Due to the bad quality of the LoTSS data, we could not study the radio properties of this system. The PSZ2 source comprises two subclusters, which are dubbed PSZ2 G124.20-36.48 N and PSZ2 G124.20-36.48 S in Table A.2.

PSZ2G126.28+65.62 A radio halo in this system was claimed by Di Gennaro et al. (2021a) with LOFAR data at 144 MHz. Follow-up uGMRT observations at 550−900 MHz did not show the presence of diffuse radio emission in the cluster possibly due to its steep spectrum (Di Gennaro et al. 2021b). Owing to the difficulty of separating the contribution of discrete sources from the diffuse emission, we classified this cluster as uncertain.

PSZ2 G133.59+50.68 Central diffuse emission in form of a radio halo is observed here for the first time. Since the fitting of the radio halo surface brightness profile does not provide reliable results, we classified this emission as RH*.

PSZ2 G133.60+69.04 (A1550) The radio halo in this cluster was originally claimed by Govoni et al. (2012) and recently confirmed during the analysis of the LoTSS-DR1 sample (van Weeren et al. 2021). We confirm the presence of a radio halo elongated in the E-W direction and the presence of possible revived fossil plasma. This system will be analyzed in detail in a forthcoming publication (Pasini et al., in preparation).

PSZ2 G135.17+65.43 This cluster was recently studied by van Weeren et al. (2021) as part of the LoTSS-DR1 cluster sample. They found the presence of a halo and relic (source G in van Weeren et al. 2021). We confirm the previous classification.

PSZ2 G138.32-39.82 The radio halo in this cluster was originally claimed by Kale et al. (2013) in the context of the Extended GMRT Radio Halo Survey. Our images confirm the detection.

PSZ2 G139.00+50.92 (A1351) The existence of a halo source in this cluster was firstly reported by Owen et al. (1999) and later studied by different authors (Giacintucci et al. 2009; Giovannini et al. 2009). Our images confirm the presence of radio halo emission that is contaminated by two bright cluster AGN.

PSZ2 G141.05-32.61 The candidate radio halo is claimed here for the first time.

PSZ2 G143.26+65.24 (A1430) The presence of a radio halo in this cluster was claimed by van Weeren et al. (2021) during the analysis of the LoTSS-DR1 sample, and later confirmed by Paul et al. (2021). A dedicated work on this system, composed of two cluster components, using LOFAR data has been recently published by Hoeft et al. (2021).

PSZ2 G143.44+53.66 A number of diffuse radio sources are noted in the cluster center. These sources are claimed here for the first time, and their nature is still uncertain. This cluster is displayed in Fig. 5.

PSZ2 G144.23-18.19 The candidate radio halo is claimed here for the first time. This is the only target in our sample in which the indication of diffuse emission in the cluster center is noticed in a cluster without redshift/mass.

PSZ2 G144.99-24.64 The candidate radio relic is claimed here for the first time. Another diffuse emission with uncertain origin is observed at the center of our images.

PSZ2 G145.65+59.30 A candidate radio halo was claimed in this system during the analysis of the LoTSS-DR1 sample (van Weeren et al. 2021). We classified this emission as uncertain as its location is offset with respect to the bulk of the X-ray emission.

PSZ2 G147.88+53.24 The presence of central diffuse emission in the form of a radio halo was recently claimed by Di Gennaro et al. (2021a) and studied with deeper observations in the context of the LoTSS Deep Fields (Osinga et al. 2021) and with uGMRT data (Di Gennaro et al. 2021b). Our images confirm the emission (which is classified as candidate radio halo due to the lack of X-ray data).

PSZ2 G148.36+75.23 The radio halo is claimed here for the first time. The diffuse emission surrounds the central cluster AGN. This cluster is displayed in Fig. 5.

PSZ2 G149.22+54.18 (A1132) The radio halo in this system was claimed with LOFAR observations by Wilber et al. (2018) and later studied with deeper observations in the context of the LoTSS Deep Fields (Osinga et al. 2021). Our images agree with previous results.

PSZ2 G149.75+34.68 (A665) The presence of diffuse emission coincident with the cluster center was detected in early observations (Moffet & Birkinshaw 1989; Giovannini & Feretti 2000; Kempner & Sarazin 2001), and it was further studied by other authors (Feretti et al. 2004; Vacca et al. 2010; George et al. 2021). Our images show that the emission entirely fills the central volume of the cluster and has a sharp surface brightness edges toward N. This cluster is displayed in Fig. 3.

PSZ2 G150.56+46.67 The candidate radio halo is claimed here for the first time.

PSZ2 G150.56+58.32 The presence of a radio halo elongated in the NW-SE direction was recently claimed by van Weeren et al. (2021) during the analysis of the LoTSS-DR1 sample. Our images agree with previous results.

PSZ2 G151.19+48.27 (A959) Diffuse radio emission in this system was reported in Owen et al. (1999). More recently, this system was studied in detail with LOFAR and GMRT observations by Bîrzan et al. (2019) who confirmed the radio halo and identified a radio relic in the SE. Our images agree with these results.

PSZ2 G154.13+40.19 The candidate radio halo is claimed here for the first time. The diffuse emission surrounds the central cluster AGN.

PSZ2 G156.26+59.64 The presence of a candidate radio halo in this cluster was reported by van Weeren et al. (2021) during the analysis of the LoTSS-DR1 sample. Here we confirm the previous classification.

PSZ2 G160.83+81.66 The presence of a radio halo in this system was recently claimed by Di Gennaro et al. (2021a) and followed-up with the uGMRT (Di Gennaro et al. 2021b). Our images confirm the emission. This is the highest-z radio halo cluster observed to date.

PSZ2 G163.61+34.30 Central diffuse emission in form of a candidate radio halo is observed here for the first time. Since the fitting of the radio halo surface brightness profile does not provide reliable results, we classified this emission as cRH*.

PSZ2 G164.65+46.37 The radio halo is claimed here for the first time. The emission is elongated along the NW-SE direction.

PSZ2 G165.06+54.13 (A990) The radio halo in this cluster was recently claimed by Hoang et al. (2021a) using LOFAR observations. Our images agree with previous results.

PSZ2 G165.46+66.15 (A1240) This cluster hosts a double radio relic system. The two relics are located to the N and S, and were firstly hinted by Kempner & Sarazin (2001), and later firmly claimed by Bonafede et al. (2009). This cluster has been the subject of a dedicated study by Hoang et al. (2018), who employed LOFAR, GMRT, and VLA observations. Our images agree with previous findings.

PSZ2 G166.09+43.38 (A773) The existence of diffuse emission in the central region of the cluster was suggested by NVSS and WEsterbork Northern Sky Survey (WENSS) observations (Giovannini et al. 1999; Kempner & Sarazin 2001). The cluster was then targeted with the VLA, and the presence of a radio halo was firmly claimed (Govoni et al. 2001; Cuciti et al. 2021). In our images, the halo appears more extended than previously observed.

PSZ2 G166.62+42.13 (A746) The prominent radio relic in the W of this system was firstly claimed by van Weeren et al. (2011). In addition, our images highlight the presence of other two fainter and smaller relics in the E and NE directions. An elongated structure with high surface brightness surrounded by extended diffuse emission is observed toward the cluster center. We classify the extended emission a radio halo, but did not provide a flux density due to the difficulty of disentangling the emission from the bright elongated structure, which possibly traces a radio relic projected on the center of the cluster. A detailed study of this system will be presented in a forthcoming paper. This cluster is displayed in Fig. 5.

PSZ2 G172.63+35.15 (A655) The radio halo is claimed here for the first time and will be the focus of a forthcoming work (Groeneveld et al., in preparation).

PSZ2 G176.27+37.54 The candidate radio halo is claimed here for the first time. The diffuse emission surrounds the central cluster AGN.

PSZ2 G179.09+60.12 (A1068) The radio halo is claimed here for the first time, although hints of diffuse emission in the cluster center were noticed in the past by Govoni et al. (2009) using VLA observations at 1.4 GHz. The detailed analysis of this system will be presented in a forthcoming paper (Biava et al., in preparation).

PSZ2 G181.06+48.47 This is a double radio relic system and it is claimed here for the first time.

PSZ2 G183.30+34.98 The candidate radio halo is claimed here for the first time. A diffuse emission elongated in the N-S direction with uncertain origin is also observed to the E of the cluster center.

PSZ2 G184.68+28.91 (A611) The candidate radio halo is claimed here for the first time. The diffuse emission surrounds the central cluster AGN.

PSZ2 G186.37+37.26 (A697) Hints of diffuse emission located in the cluster center and were firstly claimed by Kempner & Sarazin (2001) using WENSS observations. The radio halo was later confirmed and studied in detail with the VLA, GMRT and WSRT (Venturi et al. 2008; van Weeren et al. 2011; Macario et al. 2010, 2013). Our images agree with previous results.

PSZ2 G186.61+62.94 The candidate radio halo is claimed here for the first time.

PSZ2 G186.99+38.65 The radio halo and radio relic are claimed here for the first time. The radio halo is slightly elongated in the N-S direction while the relic lays in the NE outskirts of the cluster. Curiously, this relic has a mildly convex morphology; to the best of our knowledge, such an unusual curvature has been reported only for the relics in SPT-CL J2023-5535 (HyeongHan et al. 2020), the Ant Cluster (Botteon et al. 2021a), and Abell 3266 (Riseley et al., in preparation).

PSZ2 G189.31+59.24 (A1033) This cluster hosts revived fossil plasma (de Gasperin et al. 2015) and the prototype of Gently Re-Energized Tail (GReET; de Gasperin et al. 2017). In our images, diffuse radio emission in form of a radio halo is observed to the N of the GReET. This radio halo is claimed here for the first time. A dedicated paper on this target is currently in preparation (Edler et al., in preparation).

PSZ2 G190.61+66.46 The radio halo and radio relic are claimed here for the first time. The radio halo is elongated in the E-W direction while the relic is located to the W of the halo emission.

PSZ2 G192.18+56.12 (A961) The radio halo is claimed here for the first time.

PSZ2 G192.77+33.14 (A671) The candidate radio halo is claimed here for the first time. If confirmed, this would be the radio halo in the lowest-mass cluster observed to date.

PSZ2 G192.90+29.63 The candidate radio halo is claimed here for the first time.

PSZ2 G195.60+44.06 (A781) This is a complex system with multiple galaxy cluster components (e.g., Sehgal et al. 2008) with two components at redshift $z \sim 0.3$ (dubbed PSZ2 G195.60+44.06 E2 and PSZ2 G195.60+44.06 W1 in Table A.2) and the other two (dubbed PSZ2 G195.60+44.06 E1 and PSZ2 G195.60+44.06 W1 in Table A.2) at redshift $z \sim 0.43$. The presence of a radio halo in the main component of A781 (PSZ2 G195.60+44.06 E2) was disputed in the literature, being observed with the VLA at 1.4 GHz (Govoni et al. 2011) but not with the GMRT at lower frequency (Venturi et al. 2008, 2011, 2013). Deeper observations performed with LOFAR did not confirm the presence of a radio halo in this system (Botteon et al. 2019b). Our images agree with the latter results. The peripheral diffuse emission in the SE was originally believed to trace a radio relic (Venturi et al. 2008; Govoni et al. 2011), while recently it has been proposed that it results from the interaction between a weak shock and a radio galaxy (Botteon et al. 2019b).

PSZ2 G198.46+46.01 The candidate radio relic is claimed here for the first time. It is located in the S and it is elongated in the NE-SW direction. Another diffuse, elongated, emission with uncertain origin is observed toward the cluster center.

PSZ2 G205.90+73.76 The radio halo and double radio relic system are claimed here for the first time. The radio halo is elongated in the N-S direction. The two relics are located in symmetric directions (N-S) with respect to the radio halo emission.